

Non-equilibrium migration mechanisms for microfluidic bioanalysis

DISSERTATION

submitted in partial fulfillment
of the requirements for the degree of
Doktor der Naturwissenschaften
(Dr. rer. nat.)

Jan Regtmeier

Faculty of Physics
Bielefeld University

December 2007

©Copyright by Jan Regtmeier 2007
All Rights Reserved

To my wife, Anna, and our son Niklas

Erklärung

Hiermit erkläre ich, dass ich die vorliegende Arbeit selbständig verfasst und dabei keine weiteren als die angegebenen Hilfsmittel verwendet habe.

Mit einer Auslegung in der Universitätsbibliothek bin ich einverstanden.

Bielefeld, den 27. November 2007

(Jan Regtmeier)

Gutachter

PD Dr. Alexandra Ros

Prof. Dr. Peter Reimann

Datum des Einreichens der Arbeit: 27. November 2007

Preface

This thesis describes different approaches to exploit thermal noise in a microfluidic device for transport and separation of colloids and DNA. A very close collaboration of theoretical and experimental physicists led to four different projects, *Absolute Negative Mobility*, *Electrodeless Dielectrophoretic Ratchet*, *Dielectrophoretic Manipulation of DNA*, and *Giant DNA Diffusion*. The successful realization is a result of the flow of work starting with an idea followed by the continuous interaction of theoretical predictions, experiments and thereon improved predictions. The main results are already published or will be published soon.

1. A. Ros, R. Eichhorn, J. Regtmeier, T.T. Duong, P. Reimann, and D. Anselmetti. Brownian Motion: Absolute Negative Particle Mobility, *Nature*, 436:928, 2005.
2. W. Hellmich, J. Regtmeier, T.T. Duong, R. Ros, D. Anselmetti, A. Ros. Poly(ethyleneoxide) Based Surface Coatings for Poly(dimethylsiloxane) Microchannels, *Langmuir*, 21:7551-7557, 2005.
3. A. Ros, W. Hellmich, J. Regtmeier, T. T. Duong and D. Anselmetti. Bioanalysis in Structured Microfluidic Systems, *Electrophoresis*, 27:2651-2658, 2006.
4. R. Eichhorn, A. Ros, J. Regtmeier, T.T. Duong, P. Reimann, and D. Anselmetti. Paradoxical Brownian Motion in a Microfluidic Device: Absolute Negative Mobility, *European Physical Journal Special Topics*, 143:159-167, 2007.
5. J. Regtmeier, R. Eichhorn, T.T. Duong, P. Reimann, D. Anselmetti, and A. Ros. Pulsed-field Separation of Particles in a Microfluidic Device, *European Physical Journal E*, 22:335-340, 2007.
6. J. Regtmeier, S. Grauwin, R. Eichhorn, P. Reimann, D. Anselmetti, and A. Ros. Acceleration of Absolute Negative Mobility, *Journal of Separation Science*, 30:1461-1467, 2007.

-
7. J. Regtmeier, T.T. Duong, R. Eichhorn, D. Anselmetti, and A. Ros. Dielectrophoretic Manipulation of DNA: Separation and Polarizability, *Analytical Chemistry*, 79:3925-3932, 2007.
 8. J. Regtmeier, R. Eichhorn, P. Reimann, A. Ros, D. Anselmetti. Giant DNA diffusion, in preparation

In the first chapter, the physical idea of this thesis is defined and the addressed projects are outlined. The system, in which the projects are realized is presented and the relevance for bioanalytical applications is illustrated. In the first part of the second chapter (Sec. 2.1 to 2.3), an introduction is given to the structure and properties of DNA in aqueous solution and to the physics of microfluidics and electrokinetic transport. In Sec. 2.4 to 2.7, a more detailed insight into the description, modeling and characterization of Brownian migration phenomena is given. In the third chapter, the methods used in this thesis are described in detail. The fourth chapter, 'Results and Discussion', is organized according to the four different projects. Every project is introduced and the setup is explained. The results are presented together with the theory necessary to analyze and interpret the experimental data. Every result is discussed and a short summary is given. Chapter five summarizes the work and gives an outlook.

All experiments have been conducted by the author, except the ANM acceleration in the 'wrong' direction (Sec. 4.1.3), which was performed by Sebastian Grauwin under my practical supervision, and the measurements of the DNA polarizability concerning the salt and dye dependencies (Sec. 4.3.6 and 4.3.7), which were conducted by Lukas Bogunovic in the time of his Bachelor thesis under my practical supervision. The simulation, which provided much insight, was developed, programmed and continuously enhanced by Dr. Ralf Eichhorn.

Contents

Preface	i
1 Introduction	1
2 Background and Theory	6
2.1 DNA	6
2.1.1 Statistical DNA Model	10
2.1.2 Fluorescent DNA Labeling	11
2.2 Electrohydrodynamics	13
2.2.1 Hydrodynamics on the μm -Scale	14
2.2.2 The Electrical Double Layer	14
2.2.3 Electroosmosis and Electrophoresis	16
2.2.4 Dielectrophoresis	17
2.2.5 Coulomb Interaction between Colloids	21
2.3 Brownian Motion and Diffusion	21
2.4 Paradoxical Brownian Migration Phenomena	22
2.5 Theoretical Modeling	24
2.6 Thermal Diffusion in a Tilted Periodic Potential	25
2.6.1 Kramers Rate	25
2.6.2 Diffusion and the First Passage Time	27
2.7 Pitfalls in Particle Tracking	28
3 Materials and Methods	30
3.1 Chemicals and Reagents	30
3.2 Production of SU-8 Masterwafer	30
3.3 Production of Microfluidic Chip	32
3.4 Surface and Sample Preparation	34
3.5 Experimental Setup	36
3.6 Experimental Procedures	37

3.6.1	Polystyrene Particle Procedures	37
3.6.2	DNA Procedures	38
3.7	Automated Evaluation of Trapping Times	39
4	Results and Discussion	41
4.1	Absolute Negative Mobility (ANM)	41
4.1.1	Proof of Principle	42
4.1.2	Particle Separation by ANM	44
4.1.3	ANM Acceleration	47
4.1.4	Summary	51
4.2	Electrodeless Dielectrophoretic Ratchet	52
4.3	Dielectrophoretic Manipulation of DNA	57
4.3.1	DNA Trapping	58
4.3.2	Dielectrophoretic DNA Separation	61
4.3.3	Quantitative Description of DNA Migration	65
4.3.4	Polarizability of Linear and Supercoiled DNA	66
	Discussion of the Polarizability of Linear DNA	69
	Discussion of the Polarizability of Supercoiled DNA	72
	Summary of the Polarizability of Linear and Supercoiled DNA	75
4.3.5	Frequency Dependence of DNA Polarizability	75
4.3.6	Salt Dependence of DNA Polarizability	77
4.3.7	YOYO-1 Dependence of DNA Polarizability	78
4.3.8	Summary	80
4.4	Giant DNA Diffusion	80
5	Summary and Outlook	86
	Appendix	89
	Theoretical derivation of the automated determination of average migration time	89
	Tracking with camera noise	91
	Contact unit for exposure during lithography process	92
	List of Publications	93
	List of Conference Proceedings	93
	Contributions to Conferences	94
	Bibliography	96

1 Introduction

Our macroscopic world resides on a 'jittering sea of fluctuations' [1]. And even our individuality is due to this omnipresent thermal noise during fertilization. On the microscopic scale, these fluctuations can be observed as *Brownian motion*.

The leitmotif of this work is to exploit Brownian motion for *bioanalysis* in the context of migration and separation in microfluidic systems operating *far from thermal equilibrium*. The increasing importance of bioanalysis is based on the fast growing fields of biotechnology and pharmaceuticals. They have a great demand of fast, cheap and robust bioanalytical systems. On the one hand, these systems have to provide pure samples and on the other hand, have to assure the quality of the product.

In order to contribute to these demands, fundamental physical phenomena are studied, such as Absolute Negative Mobility, ratchets and diffusion control and their relevance to bioanalytical applications is illustrated. Two possible approaches are pursued: either the phenomena are directly studied with biological samples or with microparticles as models for cells in order to provide a proof of principle.

The second law of thermodynamics sets strict restrictions on the possible behavior of equilibrium systems to external perturbations. For example, when a static force is applied to a particle, which is in equilibrium with its environment, the particle has to move in the direction of the force. Any other behavior is ruled out because it could be used to extract work from a single heat bath. Thus, in order to develop new, sometimes counter-intuitive, *migration mechanisms* for transport and separation these limitations should be circumvented. And this can be achieved by operating far from thermal equilibrium, where the second law of thermodynamics does not apply.

In this work, two different possibilities are pursued to create conditions far from equilibrium, either periodic driving or a biased perturbation in its most simple form, namely a static force. Four physically different transport phenomena are addressed in spatially periodic systems with direct relevance to bioanalysis.

1. *Absolute Negative Mobility*: particle motion against a (not too large) static force. The effect is demonstrated for non-interacting Brownian particles as a response to a

static perturbation, here realized by a static force, in a spatial periodic system with intact spatial inversion symmetry. The conditions far from thermal equilibrium are created by periodic driving. The counterintuitive migration can be exploited for particle fractionation (see Sec. 4.1).

2. *Electrodeless Dielectrophoretic Ratchet*: directed average transport of microparticles although no systematic force is applied. The effect is demonstrated in a potential with a broken spatial inversion symmetry. The conditions far from thermal equilibrium are created by periodic driving. The effect allows to tune the transport direction by a single parameter, opening new perspectives for separation (see Sec. 4.2).
3. *Dielectrophoretic Manipulation of DNA*: separation of differently sized and shaped DNA fragments by thermally induced escape from potential minima. The effect is demonstrated in a tilted periodic potential, with conditions far from thermal equilibrium induced by the tilting. A new access to the polarizability of DNA is presented, allowing its quantitative study (see Sec. 4.3).
4. *Giant DNA diffusion*: diffusion enhancement and control. The effect is demonstrated in a tilted periodic potential at the *critical tilt*, i.e. any further tilting of the potential leads to a deterministic migration of the DNA 'downhill'. This control of diffusion enables new concepts for mixing and purification (see Sec. 4.4).

Interestingly, all these different effects are observed with a single experimental 'tool box', consisting of structured microfluidic channels with electrokinetic forces, i.e. electrophoresis, electroosmosis and dielectrophoresis. The basic setup is the same for all four projects (see Fig. 1.1). The central unit is a periodically microstructured linear channel, with channel dimensions of some 100 μm in width, a few millimeters in length and less than 10 μm in height. If necessary, a cross injector is included allowing the injection of samples of defined volume. The production of the chips is based on the rapid prototyping idea of *Soft Lithography* [2]. The objects inside the channel are electrokinetically manipulated by immersing electrodes into the reservoirs at the end of the channel and applying electric ac and dc voltages.

The microfluidic environment almost ideally equips us with what we need for the experimental realization of the four projects:

- Inertia forces are usually small compared to all other forces.
- The Brownian motion of particles is significant.

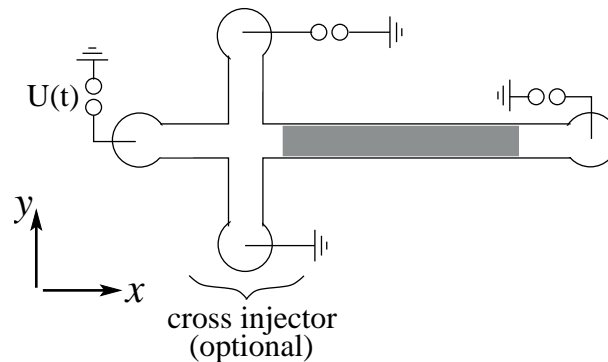


Figure 1.1: Schematic diagram of the microfluidic chip and the applied voltages. The gray shaded area symbolizes the microstructured area.

- Colloidal particles (e.g. made from polystyrene or biomolecules) settle out so slowly under gravity that they can be considered as suspended.
- Electrokinetic effects can be used to exert forces on particles because they normally acquire a charge in aqueous solution.
- Colloidal particles suspended in low concentration do not interact.

These points are discussed in more detail in Secs. 2.2 and 2.3.

Turning from purely physical aspects to applications, microfluidics might in the future allow new techniques for analysis, diagnosis and quality control in scientific fields as biology, chemistry and medicine. This is discussed, for example, by P. Yager et al. in 'Microfluidic diagnostic technologies for global public health care' [3]. The idea is to build robust sophisticated diagnostic tools, which work under most climatic conditions, in every home and can be used without expert knowledge. Through miniaturization, analysis should be possible with low sample consumption, high speed and the possibility to build complex systems on a chip. Such kind of devices are called *micro Total Analysis Systems* (μ TAS) or *Labs-on-a-Chip* [4, 5].

In a first approach, the miniaturization of already established and successful biological and chemical techniques can be pursued. For example, polymerase chain reaction [6] of DNA was demonstrated as well as protein crystallization [7]. Another example of the successful scale down of a standard technique is the capillary gel electrophoresis (CGE), with typical capillary diameters in the range of 50 to 100 μ m.

The separation of DNA fragments is of high relevance, as for example demonstrated by the 'Human genome project' [8] or the DNA vaccination [9], leading to high demands concerning the quality control. The problem is that all DNA fragments, regardless of

their length (> 100 base pairs) or conformation, show the same electrophoretic mobility [10]. The standard technique for the separation of DNA fragments according to length is the slab gel electrophoresis, inducing different mobilities by a 'reptating' motion through the gel. However, both techniques require a gel in order to invoke different electrophoretic migration velocities of differently sized DNA fragments. Because of the high viscosity of the gel, these techniques are time-consuming in the range from 30 minutes to several days, depending on the size of the DNA fragments.

Besides the simple scale down of existing techniques and with the advances in micro- and nanotechnology, the realization of new techniques has become possible by exploiting effects of the miniaturization. An example are artificial gels for DNA sieving fabricated by microstructured obstacle courses realized in microfluidic environments. This way, the accelerated separation of DNA could be demonstrated, even for long fragments, which are hard to handle with the standard techniques: the separation of DNA fragments > 40 kbp could be demonstrated in micro- [11–13] and nanopillar [14] arrays as well as in magnetic bead [15] or nanosphere matrices [16]. Size dependent DNA migration and separation have also been performed in periodically structured microfluidic channels [17, 18] and by using entropic traps [19–21].

Besides the length of a DNA fragment, its topology or conformation is of great importance for biotechnological applications, such as DNA vaccination. Only a highly purified supercoiled DNA conformation is suitable for vaccination [9]. Hence, there is an increasing interest to develop fast, miniaturized separation devices for quality control or, if highly parallelized, for sample purification. However, the only example (known to the author) of a miniaturized approach to study circular DNA is the separation of DNA with different configurations on a flat silicon surface by Li et al. [22].

Another new technique, only possible because of the miniaturization is single cell analysis. The technique already includes cell positioning, lysis and protein finger printing [23]. However, before a cell of interest can be analyzed it has to be separated from other cells. Possible separation criteria are size or charge. Besides those, the polarizability has proven to be a reliable separation criterion. Combined with dielectrophoresis, separation has been demonstrated for particles [24–26], bioparticles [27–29] or live and dead bacteria [30]. Furthermore, the fractionation of rare cells as stem or cancer cells is a very active field of research [31].

A third approach exploiting the effects of miniaturization are *ratchet devices*. The idea is to extract work out of thermal fluctuations by utilizing a potential with a broken spatial inversion symmetry although all forces average out to zero. Several devices with different realizations of the potential landscape have been presented. Asymmetric chan-

nel geometries were demonstrated [32–35] as well as potential landscapes created with microelectrodes [36]. The latter demonstrated the transport of DNA and anticipated bioanalytical applications including the detection of single-nucleotide polymorphisms.

The references [5, 37–39] provide a comprehensive introduction to microfluidics and therein realized applications.

The four projects presented here are proof-of-principles for new concepts and address different aspects and different possible applications in the general context of bioanalysis:

The project Dielectrophoretic Manipulation of DNA (Sec. 4.3) demonstrates the fast separation of DNA fragments according to length and conformation. As a quantitative characterization is indispensable for a reliable application, a new method is presented to determine the polarizability of DNA molecules quantitatively. This method is used to study the dependence of the polarizability on salt and dye concentration, and on the frequency of the applied electric field.

The project Giant DNA Diffusion shows that the diffusion of different DNA fragments can specifically be controlled in a microfluidic environment. Thus, new approaches to mixing and purification are possible (see Sec. 4.4).

The projects ANM and Electrodeless Dielectrophoretic Ratchet demonstrate the ability to separate spherical colloids (see Secs. 4.1 and 4.2). These concepts might be transferred to cells. However, the most important advantage of these two projects is the 'tunability' of the separation criterion. Typically, the separation criterion fixes the structure of the microfluidic device and thus is 'built-in' during construction. It would be of great practical use to change this criterion during the separation or between different separation experiments by changing a single parameter.

2 Background and Theory

2.1 DNA

Deoxyribonucleic acid (DNA) is a long polymer present in every cell of every living organism. It carries the genetic information in a form that can be passed from one generation to the next [40] and consequently serves as a long time information memory. A DNA molecule consists of a large number of linked nucleotides [41]. A nucleotide is composed of a sugar (deoxyribose), a phosphate and a base. The sugars are linked by phosphates forming the backbone. There are only four bases, two purines, adenine (A) and guanine (G), and two pyrimidines, cytosine (C) and thymine (T). The genetic information is stored in the sequence in which these four bases are arranged. Each type of base can form a bond only with just one other type of base (A-T and G-C) stabilized by two (A-T) or three hydrogen bonds (G-C). This complementary pairing results in the formation of a double helix with two anti-parallel complementary strands wound around a common axis (see Fig. 2.1). The double helix is additionally stabilized by hydrophobic interactions between the bases. Under physiological conditions the DNA can mostly be found in the so called B conformation (B-DNA), a right handed double helix with adjacent bases separated by 0.34 nm and nearly perpendicular oriented to the helix axis. In this conformation, ten bases make a full turn of the helix, so that the helical structure repeats every 3.4 nm. The diameter of the helix is 2.4 nm.

In aqueous solution of physiological pH, the phosphate groups on the backbone carry two negative charges per base pair. Thus, the DNA can be regarded as a polyelectrolyte and is usually surrounded by positive counterions, which stem from the surrounding solution.

In complex living organisms, the DNA molecule is much too long to be stored as a random coil. As for example the human double helix is much longer (≈ 2 m) than the largest diameter of any cell, the DNA is closely packed under the assistance of histones into 46 chromosomes [43].

Alternatively, the linear DNA can be closed to a ring. When a linear DNA polymer with its intrinsic number of helical turns is covalently closed to a ring, this form is called

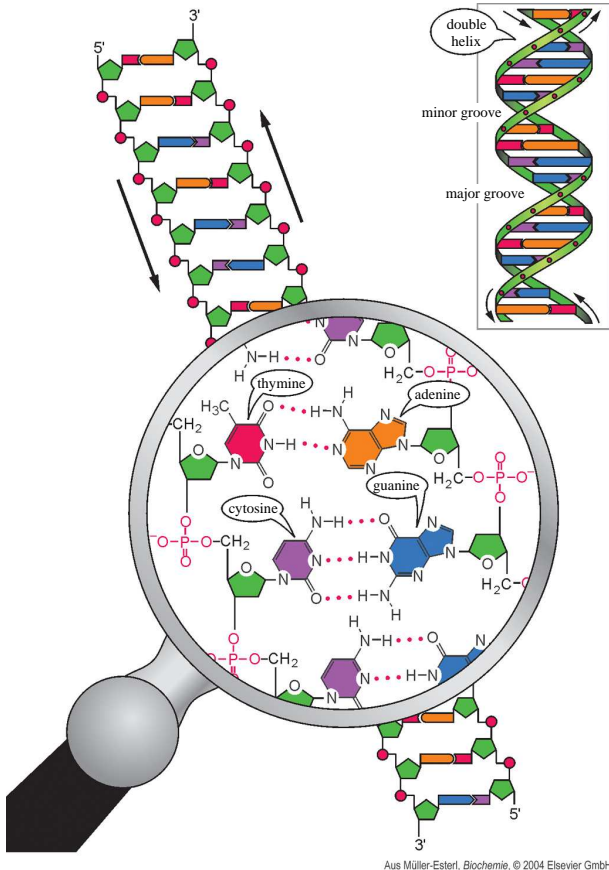


Figure 2.1: Chemical and secondary structure of B-DNA [42]. Adenine can only form a bond with thymine (A-T) and cytosine only with guanine (G-C). (A-T) is stabilized by two and (G-C) by three hydrogen bonds. Under physiological conditions the DNA takes the B-conformation, a right handed double helix with a major and minor groove.

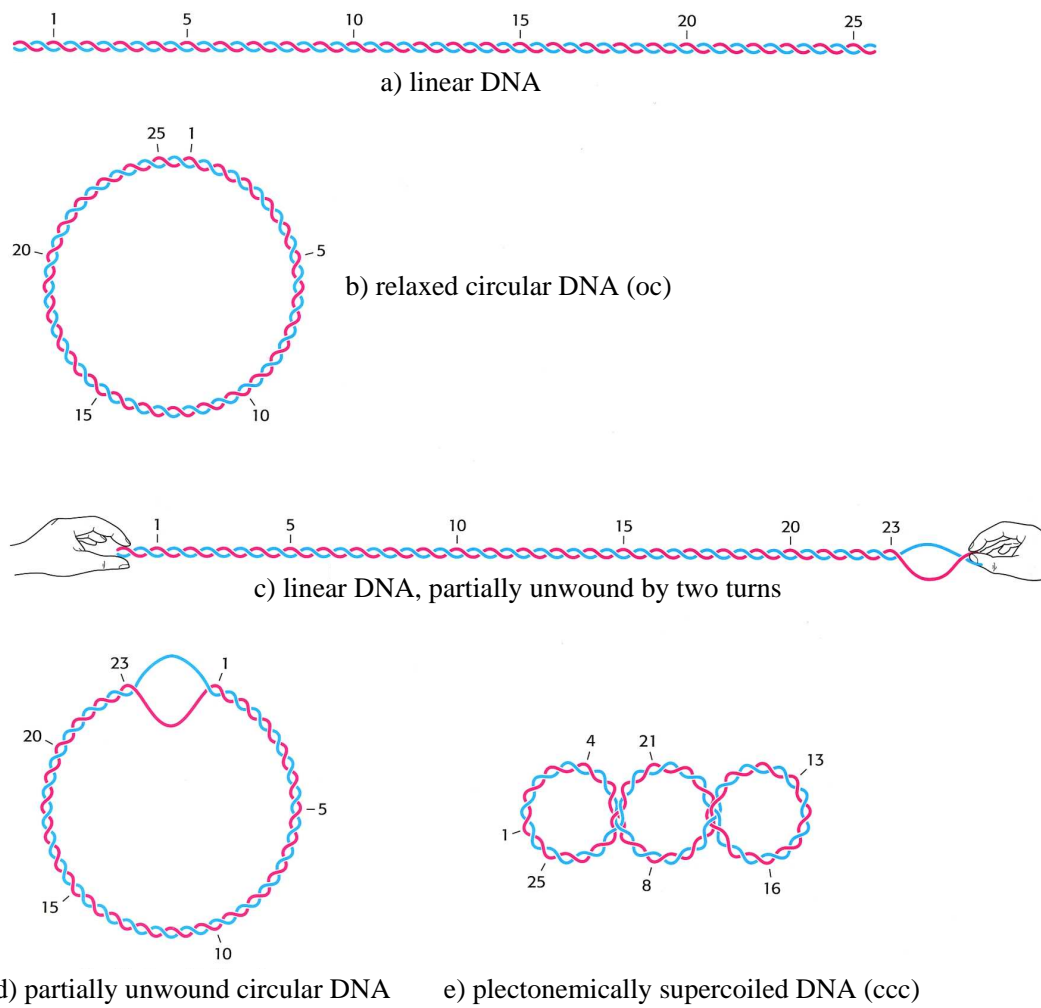


Figure 2.2: (a) Schematic drawing of linear DNA with 25 turns and 260 base pairs (bp). (b) Covalently closing the linear DNA to a ring leads to relaxed circular DNA (oc). (c) Partial unwinding of the DNA by two turns and covalent closure to a ring (d) results in partially unwound circular DNA, which is topologically equivalent, but energetically not favored compared to the supercoiled DNA (ccc) (e) [40].

a *relaxed* or *open circle* (oc) form. Twisting or untwisting, i.e. changing the intrinsic number of helical turns, and subsequent covalent closure of the DNA double strand into a ring results in a superhelix, which is called the *covalently closed circular* (ccc) form (see Fig. 2.2). This form is much more compact (see Fig. 2.3, Tab. 4.7 and Fig. 4.21). A transfer of the ccc form into the oc form is possible by introducing one or more single strand breaks. In this case, the twisting energy is dissipated because the remaining single strand joint is flexible and can rotate freely. The supercoiling can result in a *plectonemic* structure, i.e. two sections of a double helix are twisted around each other and make up a superhelix (see Fig. 2.3).

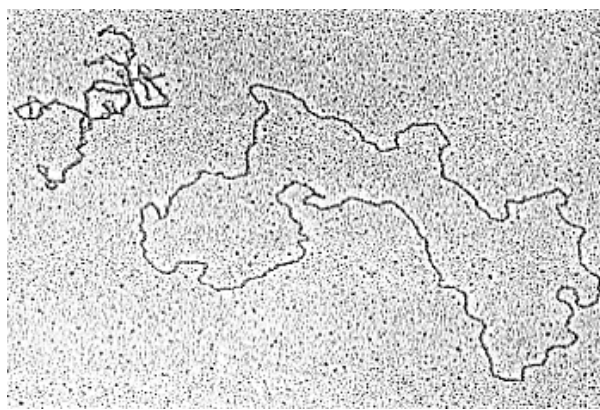


Figure 2.3: Scanning electron micrograph of a plectonemically supercoiled (ccc) DNA molecule (left) and a relaxed (oc) molecule (right) [40].

Supercoiling is biologically and biotechnologically relevant. On the one hand, the biological relevance is given because the superhelix is spatially more compact. Moreover, supercoiling may hinder or favor the ability of the double helix to unwind and thereby affects the interactions between DNA and other molecules, for example with the DNA polymerase controlling the DNA transcription [41]. Supercoiled DNA can in vivo be found in viruses or bacteria, usually with a negative supercoiling, i.e. before closure the DNA was unwound. Extrachromosomal circular DNA molecules, which can often be found in viruses or bacteria, are called *plasmids*. Although extrachromosomal, they are replicated and passed on to the daughter cells during cell division and can have biological functions, e.g. carry resistance genes against antibiotics [41]. On the other hand, supercoiling is biotechnologically relevant because these plasmids are used for cloning DNA fragments. The fragment of interest is inserted into the plasmid ring and then brought into a cell. The cell grows and divides, i.e. with each cell division the DNA is doubled. Then, the cells are lysed and the supercoiled DNA can be extracted. Usually, cloning is used to insert a specific function encoded by a DNA fragment into a

cell, such that the cell produces the desired product, e.g. vitamins, proteins, or amino acids. Furthermore, plasmids can be used for vaccination. Highly purified supercoiled DNA is injected into a living organism and taken up by the cells to some extent. Once the genetic code has been inserted into the DNA of a cell, it can produce proteins and antigens according to the new genetic code. In this way, the immunization of animals and humans can be achieved [44].

2.1.1 Statistical DNA Model

In aqueous solution, linear DNA takes the conformation of a random coil [45]. Nevertheless, it is possible to describe this coil quantitatively and there are several established models [46]. The *freely-jointed-chain* (FJC) model describes DNA as an ideal chain with stiff segments that are freely jointed, i.e. there is no restriction to any degree of freedom. In the *freely-rotating-chain* (FRC) the description is analogous to the FJC, but the angle of rotation of the segments is restricted. In contrast, the *worm-like-chain* (WLC) model describes the polymer as a single continuous flexible cylinder without joints. This model is especially suited for stiff polymers, which can be characterized by a *persistence length*. The persistence length is a measure of the stiffness of the polymer, i.e. the stiffer the polymer, the longer the persistence length.

From the models introduced above, the WLC model gives the most realistic description of DNA [46]. Let us consider a DNA double strand of *contour length* L and persistence length l_p . The conformation of the long polymer ($L \gg l_k$) is a random walk of step l_k , where $l_k = 2l_p$ is the *Kuhn length*, with an average end-to-end distance $R_{\text{end-to-end}}$ and a *radius of gyration* R_g related by [45]

$$R_{\text{end-to-end}} = \sqrt{6}R_g = (l_k L)^{1/2}. \quad (2.1)$$

The radius of gyration is defined as the distance between the axis of a rotating body and its center of gyration, and is again related to the *hydrodynamic radius* R_H via $R_g = 1.51 \cdot R_H$ [46].

The radius of gyration scales with the number of base pairs N as

$$R_g \propto N^\nu \quad (2.2)$$

with ν being the so called *Flory exponent*. The value of ν depends on the dimensionality, the model and especially on the *excluded volume effect*. For long chains, excluded volume interactions introduce an extra repulsive force, which expands the random coil. These interactions take into account that two monomers cannot simultaneously occupy the same

position. In the 3D WLC model, the Flory exponent is given by $\nu = 0.5$ without excluded, and by $\nu = 0.588$ with appreciable excluded volume effects [46] (see Sec. 4.3.4).

The crossover from one regime to the other strongly depends on the details of the molecular structure and the solvent. Different critical lengths can be found in the literature at which excluded volume effects have to be taken into account. They range from 10 kbp [45] to 100 kbp, whereas only a marginal influence of the effect is expected [47]. The large variance is probably due to the inaccuracy of the effective diameter of the DNA strand. It is often assumed that the effective diameter of DNA corresponds to the solvent dependent thickness of the screening ion cloud rather than the natural helix diameter [48]. This screening length is characterized by the *Debye length* (see Sec. 2.2.2) and values ranging from 3 to 24 nm are reported with 10 mM NaCl [48]. This screening length determines the electrostatic repulsion between different segments. Consequently, a larger effective diameter leads to a more pronounced excluded volume effect. Moreover, a weak screening makes the polymer stiffer and thus increases the persistence length, and vice versa. A value of the persistence length of 50 nm is assumed under physiological conditions [49, 50]. The flexibility of DNA is discussed in detail in [51] and a more detailed description of the ion cloud is given in Sec. 2.2.2.

2.1.2 Fluorescent DNA Labeling

Fluorescent labeling is a standard technique for the optical detection of single DNA molecules [52], i.e. a dye molecule is specifically or unspecifically bound to the target molecule. The fluorescent emission of photons allows the optical detection even of molecules that are much smaller than the achievable optical resolution.

A dye molecule absorbs a photon and is excited into a higher energy state (see Fig. 2.4). After about 10^{-8} s, the excited system can emit a photon and fall back into the ground state. The energy of the emitted photon is reduced compared to the energy of the exciting photon (*Stokes* or *red shift*) due to energy losses during the excitation. Besides the relaxation through fluorescence, there are several other relaxation processes. *Intersystem crossing* (ISC) is possible due to intermolecular interactions, i.e. there is a crossing from the excited singlet state into the triplet state. From the triplet state, the relaxation through photon emission is also possible and called *phosphorescence* (P). However, this process is quantum mechanically forbidden and thus unlikely, resulting in a long life time of the excited triplet state. Another process is a *photo induced chemical reaction* (Chem).

There are further relaxation processes without radiation, e.g. rotational relaxation or

collisions with other molecules close by (*internal conversion* (IC)). All of these effects can lead to *quenching* (Q), i.e. a reduction of the fluorescence intensity.

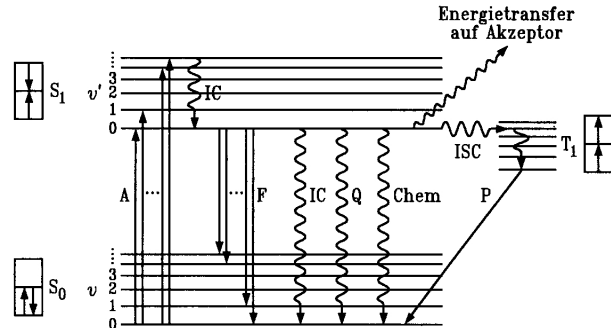


Figure 2.4: Jablonski diagram of electronic states of a molecule and the transitions between them. The system is excited from the ground state v to the first excited state v' through absorption of a photon, and several possibilities for relaxation are depicted (see main text) [53].

Intercalating fluorescent dyes are frequently used for DNA detection. The dye molecules intercalate between two base pairs of the DNA molecule and thereby increase the quantum yield up to a factor 3000 compared to the free state [54, 55]. The reason can be found in the spatial fixation, thus limiting the degrees of freedom of rotation and the probability of collisions with solvent molecules. Examples of intercalating dyes are ethidium bromide or the cyanine dimers YOYO-1 and TOTO-1 [56].

YOYO-1 is particularly suitable for DNA labeling. Because of its planar aromatic rings and its high charging of four positive charges per YOYO-1 molecule, it can easily intercalate into the negatively charged DNA. This fact is supported by the high binding constant of $K = 6 \cdot 10^8 \text{ Mol}^{-1}$ (in phosphate buffer with pH 7 and 100 mM NaCl) [54].

The intercalation accordingly changes the DNA charging, which might change the electrokinetic properties of DNA. Nevertheless, Carlsson et al. [57] observed only minor changes.

However, the intercalation needs some time to equilibrate. A double band in an agarose gel is found, when a sample of a single DNA species is stained with YOYO-1 and a gel is run of the sample within a few hours after staining [58]. This indicates subpopulations with different YOYO-1 content. Furthermore, each intercalated YOYO-1 molecule stretches the DNA molecule by about 0.34 nm resulting in a changed charge density and an increase in persistence length [50, 59]. For λ -DNA with 48.5 kbp and a contour length of 16 μm , the intercalation of YOYO-1 with a concentration of 1 dye molecule per 5 base pairs stretches the molecule to a total length of 20 μm . Moreover, the persistence length is increased from about 50 μm to 64 μm at 10 mM NaCl [50].

2.2 Electrohydrodynamics

The miniaturization of fluidic systems promises similar advances as already achieved in microelectronics. Microfluidic devices, fluid filled channels with a width of typically a few 100 μm or less, offer the possibility of performing numerous experiments rapidly and in parallel, while consuming little reagent [5, 60]. However, the fundamental fluid physics changes rapidly as the length scale is reduced, much before quantum effects have to be taken into account [60]. For example, mass transport in a microfluidic system is dominated by viscous dissipation and inertia effects are in general negligible. This implies that mixing is difficult in a microfluidic system, as inertia is responsible for nonlinearity and thus for turbulences. However, the small dimensions bring other physical phenomena to prominence, which are less familiar on the macroscale. Here, a few examples are given.

Diffusion is usually a small effect, as nobody waits for the sugar in the tea cup to distribute itself by diffusion (it would take hours to days). In a microfluidic device, however, an object can easily travel a typical channel width within only a few seconds, e.g. Hemoglobin diffuses with $69 \mu\text{m}^2/\text{s}$ [61]. And even latex spheres of $1.9 \mu\text{m}$ diameter diffuse with $0.1 \mu\text{m}^2/\text{s}$.

Most objects in our every day life are not buoyant and thus sediment quickly. However, if the particles are very small and have a density close to water, just as DNA molecules, proteins, or microspheres, diffusion dominates over sedimentation [62]. More precisely, if the density of the object is not too large, it can be regarded as suspended in a microchannel, with an average height that can be calculated [63].

Scaling down a capillary of radius R_c , the cross sectional area scales as $\sim R_c^2$ and the surface only as $\sim R_c$. Thus, the surface to volume ratio increases and interfacial surface effects become more important. To name just a few, the adsorption of objects onto the channel surface has to be controlled and if permeable materials are used to construct a microfluidic channel, the permeation has to be considered [64].

Finally, electrokinetic effects are important because particles normally acquire a charge in aqueous solution. Moreover, the channel walls also acquire charges as they are often composed of glass or a polymer. Ions from the buffer screen these charges. Thus, applying an electric field moves a charged object in solution, but at the same time the ions at the channel surface.

2.2.1 Hydrodynamics on the μm -Scale

The flow, for example in a capillary, can be characterized by the *Reynolds number*

$$Re = \frac{\rho v R_c}{\eta}, \quad (2.3)$$

where R_c , ρ , η and v are the capillary diameter, the density, the viscosity of the fluid and the fluid velocity. This dimensionless number gives the ratio between inertia forces and viscous forces. For $Re < 2300$ the viscous forces dominate and the flow is *laminar*. For larger values it becomes *turbulent* [65]. In a typical microfluidic system, the Reynolds number is much smaller than one ($Re \ll 1$), i.e. inertia effects are irrelevant [60] and the dynamics is *overdamped*. This can be illustrated by the following example. A particle of diameter $1 \mu\text{m}$ is pushed and moves with a velocity of $30 \mu\text{m/s}$. If suddenly no force is applied anymore, the particle stops within 0.01 nm and $0.6 \mu\text{s}$ [66]. A further consequence is that the flow is laminar. Thus, mixing is not possible by steering, but dominated by diffusion (see Sec. 4.4) [60].

Due to the spatial dimensions of a typical microfluidic channel, even small water droplets in the reservoir of a micro channel can induce high fluid velocities. The pressure P in a water drop of radius r_d is given by

$$P = \frac{2\gamma}{r_d}, \quad (2.4)$$

where γ is the surface tension. For example, with $r_d = 2 \text{ mm}$ and the surface tension of water, the pressure results in $P \approx 70 \text{ Pa}$. The velocity of a fluid in a channel due to pressure can be estimated by [67]

$$v \approx \frac{h_c^2}{3\eta} \left(\frac{P}{L_c} \right), \quad (2.5)$$

with L_c being the channel length and h_c the channel height. A 2 mm water droplet induces a velocity of about $180 \mu\text{m/s}$ in a 11 mm long and $9 \mu\text{m}$ high channel.

2.2.2 The Electrical Double Layer

Most substances acquire an electric surface charge, if they are brought into contact with an aqueous (polar) medium [62]. The mechanisms include ionization, ion adsorption, and ion dissolution. Any charged surface in an electrolyte solution will influence the distribution of nearby ions in the solution. Ions of opposite charge (*counterions*) are attracted toward the surface while ions of like charge (*coions*) are repelled. This attraction and repulsion can be described with two layers of ions at the charged surface. The

first layer is the *Stern layer*, in which the ions in the immediate vicinity of the surface adsorb or *condense* permanently and the *diffuse* or *Gouy-Chapman-layer*, in which the attracted ions remain mobile due to the already weakened attraction and the Brownian motion (see Fig. 2.5). Both layers together are called the *electric double layer* [62].

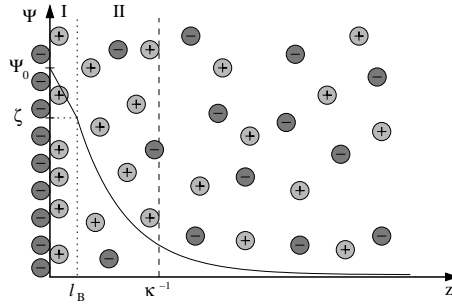


Figure 2.5: Electric double layer, where the *Stern layer* is found in region I and the *diffuse layer* in region II. The potential decays linearly in I and exponentially in II.

The thickness of the Stern layer is roughly given by the *Bjerrum length*

$$l_B = e^2 / (4\pi\epsilon_b\epsilon_0 k_B T), \quad (2.6)$$

where ϵ_b is the dielectric constant of the fluid, ϵ_0 the permittivity of vacuum, e the elementary charge and $k_B T$ the thermal energy. The typical Bjerrum length is about the diameter of the condensed counterions.

Generally, the distribution of mobile ions can be described using the *Poisson-Boltzmann* equation [62]

$$\epsilon_b\epsilon_0 \nabla^2 \Psi = -e \sum_k z_k C_k \exp(-e z_k \Psi / k_B T), \quad (2.7)$$

where z_k is the valence of ion k , C_k the bulk concentration of ions of the species k and Ψ the electric potential. Under the assumption of $z_k e \Psi \ll k_B T$, Eq. 2.7 can be linearized and gives the *Debye-Hückel theory*, which is applicable to the diffuse layer. According to this model, the electric potential in the diffuse layer decays exponentially from its value at the boundary

$$\Psi(z) = \Psi(l_B) \exp(-\kappa z), \quad (2.8)$$

with $\Psi(l_B)$ being the potential value at the boundary of the condensed and the diffuse layer, called ζ -potential, and $\kappa^{-1} = \lambda_d$ the screening length. This length is called *Debye length* and is given by [62]

$$\lambda_d = \left(\frac{\epsilon_b \epsilon_0 k_B T}{2e^2 I} \right)^{1/2}, \quad (2.9)$$

where $I = (1/2) \sum_k z_k^2 C_k$ is the *ionic strength*. The typical Debye length for a glass capillary and physiological buffer conditions is in the order of $\lambda_d = 3$ nm.

2.2.3 Electroosmosis and Electrophoresis

Electrokinetic phenomena arise when the mobile portion of the diffuse double layer and an external electric field interact in the viscous shear layer near the charged surface. If an electric field is applied tangentially along a charged surface, it will exert a force on the counterions in the diffuse layer resulting in a migration. Due to viscous drag, the surrounding solvent is drawn by the counterions and therefore starts to flow. The movement of the liquid relative to a stationary charged surface with surface potential ζ by an applied electric field is called *electroosmosis*. Assuming a thin double layer compared with the characteristic length scale of the microdevice, e.g. the diameter of a capillary, the electroosmotic mobility $\mu_{eo} = \frac{\bar{v}}{E}$ is given by [62]

$$\mu_{eo} = -\frac{\epsilon_0 \epsilon_b \zeta}{\eta}. \quad (2.10)$$

This formula is known as the *Helmholtz-Smoluchowski* equation. Thus, outside the double layer, the flow profile is plug like. Only within the thin diffuse layer itself, the velocity is not constant as the no slip boundary condition at the surface must be retained.

A second electrokinetic phenomenon is *electrophoresis* and it describes the movement of a charged surface with surface potential $\bar{\zeta}$ relative to a stationary liquid by an applied electric field. Thus, the electrophoretic mobility of a charged object is obtained from the electroosmotic mobility by just changing the frame of reference [62]

$$\mu_{ep} = +\frac{\epsilon_0 \epsilon_b \bar{\zeta}}{\eta}. \quad (2.11)$$

As a consequence, assuming a thin double layer compared to the particle size, the electrophoretic velocity is independent of the particle size and shape for constant surface potential. This especially applies to DNA, which always shows the same electrophoretic velocity independent of its length (>100 bp). Only the assumption $z_k e \zeta \ll k_B T$ might be questionable for DNA or other highly charged objects [68], but the length independent migration of DNA is experimentally well confirmed [10, 45] (see Sec. 4.3.4).

Under many conditions of practical interest, the resulting electroosmotic fluid velocity is proportional to the local electric field with the constant of proportionality everywhere the same [69]. Consequently, electroosmosis and electrophoresis can be modeled as a single effective force. The conditions for this *similitude* are a steady electric field, a thin double layer compared to the particle and device dimensions and fluid velocities on all inlet and outlet boundaries that satisfy the Helmholtz-Smoluchowski relation. These

conditions are fulfilled under the given experimental conditions because the double layer (≈ 3 nm) is much thinner than any characteristic length scale of the microfluidic device ($> 2\mu\text{m}$), including in- and outlet boundaries or the particles in the device (for the smallest DNA molecules used $R_g > 100$ nm). Moreover, the electric field is steady in the device as electric fields are applied at the ends of the channel and the channel consisting of an insulating polymer and filled with a conducting buffer.

Thus, the net particle velocity is given by the superposition of electrophoresis and electroosmosis [70]

$$\vec{v} = \frac{\epsilon_0 \epsilon_B (\bar{\zeta} - \zeta)}{\eta} \vec{E}. \quad (2.12)$$

This description is sufficient to model the mobilities observed in the experiments. However, there are more effects due to the finite thickness of the double layer. One consequence is the *electrophoretic retardation*. The effect results from the fact that the ions in the double layer move opposite to the particle. Because of the viscosity, a drag is exerted on the particle by the electroosmotic flow at its surface. Another effect changing the velocity is the *relaxation*. The motion of the ions because of the local electroosmotic flow distorts the double layer from sphericity [62]. A review of ac electrokinetic effects including scaling laws is given by [71]. In the following Sec., the main focus will be on dielectrophoresis solely.

2.2.4 Dielectrophoresis

Dielectrophoresis (DEP) is the translation of neutral matter caused by polarization effects in a nonuniform electric field [72]. Thus, DEP can be used to manipulate every polarizable object [25], such as latex spheres [73–76], cells [77], viruses [27], proteins [78, 79] or carbon nanotubes [80].

The generation of a nonuniform electric field is possible with two different approaches (see Fig. 2.6). The first one is based on microelectrodes, the other one on creating gradients with nonconducting obstacles (*electrodeless dielectrophoresis* [81], see also Fig. 2.7, Secs. 4.3.1 and 4.2). The latter has the advantage of allowing a monolithic fabrication, and more importantly, provides field gradients over the entire depth of the microchannel.

The dielectrophoretic force is given by [72]

$$\vec{F}_{DEP} = (\vec{p} \cdot \nabla) \vec{E}, \quad (2.13)$$

where \vec{E} is the electric field and \vec{p} the induced dipole. The latter can be calculated according to

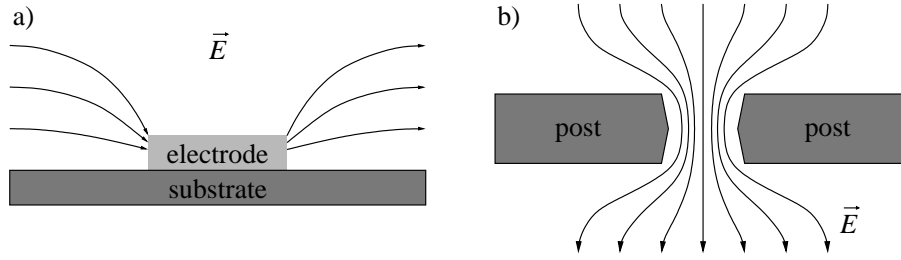


Figure 2.6: a) Side view of an inhomogeneous electric field created by microelectrodes. The maximum electric gradient is found at the corners of the microelectrode and thus does not extend over the full height of the channel. b) Top view of an inhomogeneous electric field created by two non-conducting posts. The strongest electric gradient is found at the corners of the posts and the gradient is created over the full post height.

$$\vec{p} = \alpha(\omega)\vec{E}, \quad (2.14)$$

where $\alpha(\omega)$ is the frequency dependent polarizability.

The direction of the force does not depend on the polarity of the electric field and is observed with ac as well as dc voltages. However, the direction depends on the difference of the dielectric permittivity of the particle and the solvent. Objects are attracted to regions of stronger electric fields when their permittivity ϵ_p exceeds that of the medium (*positive dielectrophoresis*) and vice versa (*negative dielectrophoresis*) [82]. The latter is of great importance, because the polarizability depends on the medium. More precisely, the net polarizability is given by the material of the particle itself, its ion cloud and the surrounding solvent.

For a spherical particle the DEP force can be calculated with several assumptions. The particle is a homogeneous dielectric particle with ohmic conductance but no dielectric loss. This particle is suspended in a dielectric solvent, which also only shows ohmic loss. Additionally, the electric field must be applied much longer than the time constant associated with the accumulation of free charge at the surface of the sphere.

Then, the dipole moment of a sphere is given by [83]

$$\vec{p} = 4\pi\epsilon_m Re[K(\omega)]R^3\vec{E}, \quad (2.15)$$

where $Re[K(\omega)]$ is the real part of the so called *Clausius-Mossotti* factor $K(\omega) = \frac{\epsilon_p - \epsilon_m}{\epsilon_p + 2\epsilon_m}$ and $\epsilon_{p/m}$ are the frequency dependent dielectric constants of the particle and the medium respectively [71, 84]. Thus, the DEP force for a spherical particle, with the assumptions listed above and neglecting the polarization of the surrounding ion cloud, is given by [72, 82]

$$\vec{F}_{DEP} = 2\pi\epsilon_0\epsilon_m R^3 Re[K]\nabla\vec{E}^2 \quad (2.16)$$

and scales with the volume of the particle. For the experimental conditions used here, the assumptions are valid, as the particles demonstrate negative dielectrophoresis, i.e. the polarization of the particle itself dominates the total polarizability and not its surrounding ion cloud (see Sec. 4.2).

In contrast, DNA is not a homogeneous dielectric sphere and the assumptions made above do not apply, i.e. the scaling of \vec{F}_{DEP} with the volume fails for DNA molecules (see Sec. 4.3.4). However, a more general description is possible. The underlying potential to the dielectrophoretic force in Eq. 2.13 is given by $W = -\vec{p}\vec{E}$. Hence, the application of an electric field $\vec{E}(t) = \vec{E} \sin \omega t$ creates a dielectrophoretic potential landscape given by (see Fig. 2.7)

$$W = -(1/2)\alpha\vec{E}^2, \quad (2.17)$$

thereby using Eq. 2.14. In this description, adsorption effects are neglected so that the polarizability α is real-valued. Moreover, a quasi-static response of the object to the time dependent electric field is assumed, i.e. the object does not follow the time dependent electric field and the factor $(1/2)$ stems from the average of $\sin^2 \omega t$ (see Sec. 4.3.1).

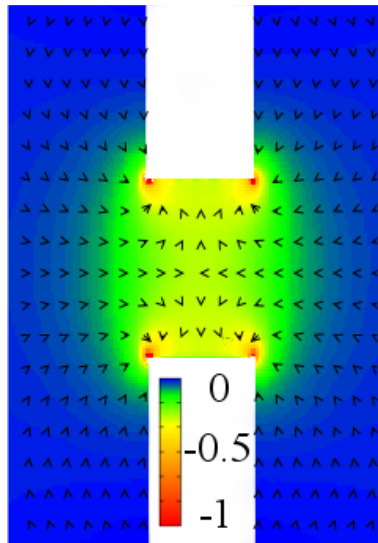


Figure 2.7: Dielectrophoretic potential $W = -(1/2)\alpha\vec{E}^2$ in a gap between two posts (white rectangles) in the case of positive dielectrophoresis ($\alpha > 0$). The electric field is numerically calculated as described in Sec. 2.5. The color code indicates the magnitude of the potential energy in arbitrary units. The arrows indicate the direction of the resulting dielectrophoretic force field. Potential minima occur near the edges of the posts.

There are two possible contributions to the polarizability of DNA, induced or permanent dipoles. It is widely assumed that DNA possess no permanent dipole [85, 86].

However, DNA molecules with a length of 400-850 bp were reported to show a small permanent dipole moment [85, 87]. This observation might depend on the base pair sequence, which induces a permanent bending of the DNA strand, and on the buffer conditions [88].

The major part of the DNA polarizability stems from the induced dipole [81, 85, 89, 90]. The charged DNA strand accumulates an ion cloud in aqueous solution. The counterions can be displaced by an electric field inducing a dipole. The magnitude of the latter depends on the polarizability $\alpha(\omega)$ of the molecule, which depends on the frequency of the applied field. Although the exact mechanism is still not well understood [85], Chou et al. [81] demonstrated that the polarizability decreases with increasing viscosity of the surrounding buffer. Hence, it seems plausible that the induced dipole stems from the mobile counterions (see Fig. 2.8). Depending on the thickness of the Debye layer, a displacement of the ions along the DNA strand can be imagined in case of a thin double layer and the DNA can be modeled as a random coiled charged cylinder. If the Debye length is large, the DNA can be considered as a large spherical ion cloud. Hence, the ions could be freely displaced in the vicinity of the DNA strand, as depicted in Fig. 2.8. Moreover, the ion displacement might be hindered by juxtaposition or kinks of the DNA strand [81, 91].

The time available to displace an ion along the DNA strand is determined by the frequency of the ac electric field (see Sec. 4.3.5). The frequency dependence of the polarizability is well documented and covers a wide frequency range from 10^{-1} to 10^7 Hz [90, 92, 93]. The ion displacement discussed so far is only possible in the low frequency range below 200 kHz as otherwise the time is too short for the required charge transport. In the higher frequency bands around 2 and 12 MHz, the mechanism is attributed to concentration dependent interactions of DNA molecules and fluctuations in the double layer [86, 94]. The polarization at 12 MHz is also attributed to a so called *Maxwell-Wagner* interface polarization [91, 95, 96].

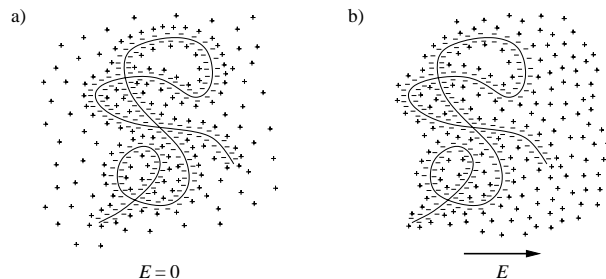


Figure 2.8: Cartoon of the DNA ion cloud polarization in an electric field for large λ_d .

However, the manipulation of DNA via DEP is not possible over the full frequency

range. There are only a few narrow frequency bands, in which the polarization is strong enough to be exploited for dielectrophoresis (see Sec. 4.3.5). For example, manipulation has been reported in the range below 1 kHz [81] (see also Sec. 4.3.1) as well as in the low MHz range [27, 78, 90, 97]. Especially in the low frequency range, there are several more effects that contribute and complicate the analysis. There are hydrodynamic effects, electroosmosis along the DNA strand and the electrophoretic motion of the DNA molecule (see Sec. 4.3.1). Moreover, the capability of manipulating DNA depends on the salt concentration. The polarizability decreases with increasing salt concentration and especially divalent ions let the polarizability vanish already at very low concentrations (see Sec. 4.3.6) [85, 89, 90, 95, 98].

2.2.5 Coulomb Interaction between Colloids

The charges of particles and molecules in aqueous solution are *screened* through the counterions of the buffer. Nevertheless, there still is a Coulomb interaction, which is only reduced by the counterions. Accordingly, the resulting interaction between charged colloids or molecules is short ranged, i.e. it decays exponentially with $\exp(-\kappa r)/r$. The interaction can be described in detail with the theory of Derjaguin, Landau, Verweij and Overbeek (DLVO) [99]

$$V_{\text{DLVO}}(r) = \left(\frac{q \exp(\kappa R)}{1 + \kappa R} \right)^2 \frac{\exp(-\kappa r)}{\epsilon_b \epsilon_0 r}, \quad (2.18)$$

with r being the distance between two particles with charge q (without effects of the solvent) and R the radius of the particles, also without solvent. The potential decays on the length scale of the Debye length $\lambda_d = \kappa^{-1}$. Because of the Debye length of about 3 nm under the given experimental conditions, one can assume that the particles and molecules in the experiment interact as hard walls (see Sec. 4.1).

2.3 Brownian Motion and Diffusion

The *Brownian motion* is named after the Scottish botanist R. Brown, who first discovered the random thermal motion of pollen under the microscope. The origin of this motion can be found in the omnipresent collisions with molecules of the surrounding medium, which happen on a time scale of 10^{-14} s. The appropriate quantity to describe the intensity of this motion for a particle is the *diffusion coefficient*, which is defined as

$$D := \lim_{t \rightarrow \infty} \frac{\langle \vec{R}^2(t) \rangle - \langle \vec{R}(t) \rangle^2}{2dt} \quad (2.19)$$

with d being the dimensionality, t the time and $\vec{R}(t)$ the position of the particle in d dimensions at time t . $\langle \cdot \rangle$ denotes the ensemble average.

In 1905, A. Einstein was able to explain Brown's observations with the molecular kinetic theory of heat [100] and derived the diffusion coefficient as

$$D = \frac{k_B T}{6\pi\eta R}, \quad (2.20)$$

showing that D only depends on the temperature T , viscosity of the medium η and particle size R . Hence, the radius of an object can be determined from diffusion coefficients, when the temperature and the viscosity of the surrounding solvent are known. In particular, it allows to measure the hydrodynamic radius of DNA molecules (see Sec. 4.3.4), which is related to its radius of gyration (see Sec. 2.1.1).

2.4 Paradoxical Brownian Migration Phenomena

Often, the Brownian motion or thermal noise is considered as a nuisance. However, the unavoidable thermal fluctuations have found applications, for example in the transport and sorting of colloidal particles [35, 101, 102]. Studying migration phenomena, the observable of foremost interest is the average velocity or current

$$v \equiv \langle \dot{x}(t) \rangle \equiv \left\langle \lim_{t \rightarrow \infty} \frac{x(t) - x(0)}{t} \right\rangle, \quad (2.21)$$

where $x(t)$ is the position of the particle at time t . Here, the current is studied only in one dimension because all phenomena are demonstrated in a linear channel, and only the net velocity along the channel axis is of interest for the migration and separation.

Usually, if no force is applied to a system at rest, one expects zero current ($v = 0$) (see Fig. 2.9(a)). And if a force is applied, the velocity should point in the same direction as the applied force. This is totally in accordance with Newton's second law and the second law of thermodynamics.

However, there are several counterintuitive transport phenomena in spatially periodic systems. The prerequisites are an interplay of nonlinear dynamics to reconcile the effect with Newton's second law and conditions far from thermal equilibrium in order not to violate the second law of thermodynamics.

Absolute Negative Mobility (ANM) is such a counterintuitive phenomenon (see Fig. 2.9(b)) and refers to the average motion *against* a (not too large) static force of whatever direction. ANM has been demonstrated experimentally in semiconductor

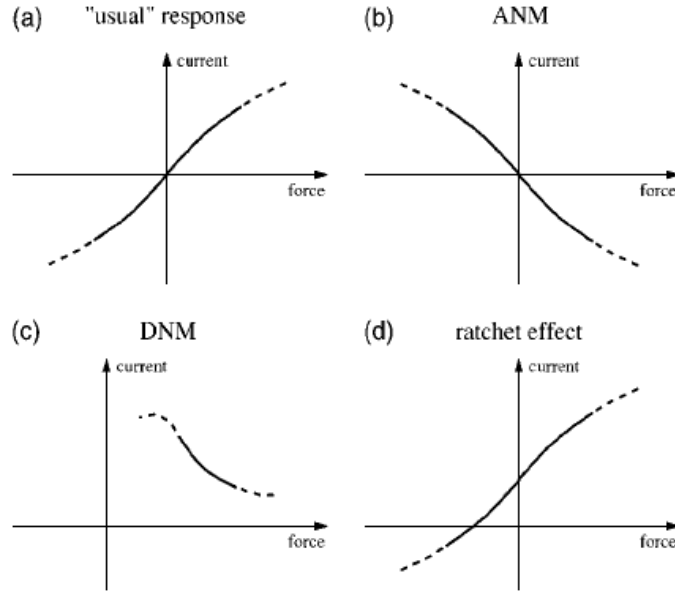


Figure 2.9: Illustration of several fundamentally different current force characteristics. a) 'Usual' response; b) Absolute Negative Mobility (ANM); c) Differential Negative Mobility (DNM); d) ratchet effect [103].

devices [104,105], termed absolute negative resistance or conductance in this context (see [103] for a review and Refs. therein). In these experiments, ANM is based on quantum mechanical effects. ANM can also be demonstrated for interacting Brownian particles [106]. In this case, the mechanism is of classical character, but collective effects are indispensable. The further reduction to a single particle was commonly assumed to be impossible. Only quite recently, theoretical counterexamples were presented, demonstrating the existence of ANM in classical, single particle models [107–110] (see also [103] and Refs. therein). The experimental realization of single particle ANM, ANM based separation and the acceleration of ANM are described and discussed in Sec. 4.1.

In distinction to ANM, the effect of *Differential Negative Mobility* (DNM) (see Fig. 2.9(c)) describes the decrease of the current with increasing force, i.e. in DNM the motion slows down with increasing static perturbation while the direction of motion remains always that of the perturbation [103].

Finally, the *ratchet effect* is a third intriguing migration mechanism (see Fig. 2.9(d)). It is characterized by directed average motion, although on average no force is applied (see Sec. 4.2). The ratchet effect and ANM are different physical effects, as the ratchet needs an asymmetry, while ANM only occurs in symmetric systems.

2.5 Theoretical Modeling

A numerical simulation is based on an appropriate modeling of the system of interest. All acting forces have to be analyzed and, accordingly, the theoretical model should reduce the system to the physically crucial essentials.

Here, the system of interest is a colloidal Brownian particle driven by electric fields through a microfluidic obstacle course. The obstacle course is arranged in a linear channel, with x and y directions defining the horizontal plane and z the vertical direction. The electric field is applied along the channel axis, i.e. the x -axis.

The model is based on the following assumptions: (a) forces in z direction are assumed as isotropic and thus the system reduces to 2D. (b) The walls and particles have hard walls and (c) interact as those (see Sec. 2.2.5). (d) The walls and obstacles are perfect insulators and the buffer is an ideal conductor. (e) The noise is modeled as Gaussian white noise.

The driving forces, namely electrophoresis and electroosmosis, are simulated as a single effective force. This is allowed because under the given experimental conditions the *similitude* of electroosmosis and electrophoresis is assured (see Sec. 2.2.3) [69].

Accordingly, we model the motion of a particle with coordinates $\vec{r} = (x, y)$ by the stochastic Langevin dynamics

$$f\dot{\vec{r}} = \vec{F}(\vec{r}) + q\vec{E}_*(\vec{r}, t)U(t)/U_* - \nabla W(\vec{r}) + \xi(t) \quad (2.22)$$

where $\vec{r} = \vec{r}(t)$. Inertia effects are neglected because of the overdamped dynamics (see Sec. 2.2.1), and f denotes the viscous friction coefficient [111, 112]. The force field $\vec{F}(\vec{r})$ derives from an effective hardwall potential of the microstructure, and includes the finite particle radius (see Fig. 2.10), while $q\vec{E}_*(\vec{r})$ is the electrophoretic force on the bead generated by a constant reference voltage $U_* = 1$ V, and $U(t)$ is the actual applied voltage. The force given by $-\nabla W(\vec{r})$ allows the integration of further potentials, e.g. dielectrophoretic potential landscapes. The thermal fluctuations are modeled by $\xi(t) = (\xi_x(t), \xi_y(t))$, where $i \in \{x, y\}$ are independent, unbiased Gaussian noise sources, satisfying the fluctuation dissipation relation $\langle \xi_i(t)\xi_i(t') \rangle = 2fk_B T \delta(t - t')$.

In order to calculate the electric field $\vec{E}_*(\vec{r})$, the Laplace equation

$$\Delta\phi = 0 \quad (2.23)$$

is solved with periodic boundary conditions along the y axis. Along the x axis, a preset potential difference over several spatial periods was imposed and the resulting 'central

unit cell' periodically continued. Assuming that the buffer solution is a perfect conductor and the microstructure and channel walls perfect insulators, Neumann boundary conditions are adopted at the borders between microstructure and buffer [70].

By this procedure, the relevant force field $q\vec{E}_*(\vec{r})$ can be determined up to an unknown gauge factor between the experimental and theoretical potential differences. In Eq. 2.22, f represents the effective coupling to the thermal environment and q the coupling to the electric field, quantifying the above mentioned gauge factor. Both factors depend in a very complex way on the geometry and the chemical surface properties of microstructure and particles, as well as on the electrohydrodynamic buffer properties. To determine q and f quantitatively, the voltage dependent particle velocity as well as the diffusion coefficient, known from experiments, are reproduced by the model dynamics Eq. 2.22 with fit parameters q and f [70] (see Sec. 4.1).

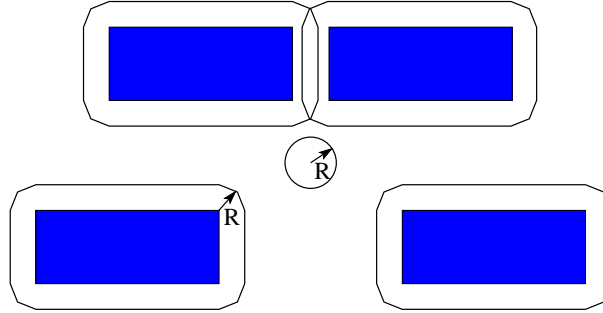


Figure 2.10: Idea of simulating a colloidal object as a point-shaped object by extending the obstacles by the radius of the particle [70].

2.6 Thermal Diffusion in a Tilted Periodic Potential

Thermal diffusion in a tilted periodic potential provides a very general concept in order to describe effects ranging from chemical reactions [113] to Josephson junctions [114] and particle separation by electrophoresis [115, 116].

2.6.1 Kramers Rate

The Kramers rate describes the rate of escape of a point like particle from a meta stable potential well, as depicted in Fig. 2.11. The piecewise harmonic potential $W(x)$ can be described as [117, 118]

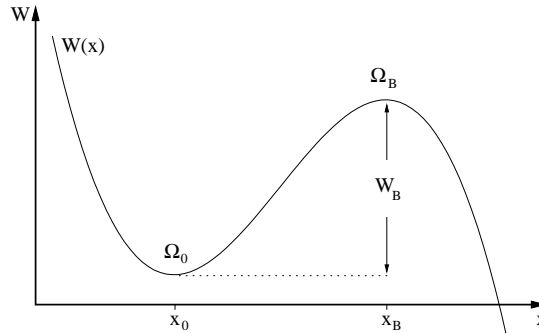


Figure 2.11: Meta stable potential.

$$W(x) - W(x_0) = \begin{cases} \frac{1}{2}\Omega_0^2 (x - x_0)^2 & \text{for } x \approx x_0, \\ W_B - \frac{1}{2}\Omega_B^2 (x - x_B)^2 & \text{for } x \approx x_B, \end{cases} \quad (2.24)$$

with x_0 being the starting position of the particle, Ω_0^2 and Ω_B^2 the curvatures at x_0 and x_B , i.e. the second derivative of the potential $\frac{\partial^2 W(x)}{\partial x^2}$ at x_0 and x_B . The length scale, on which the potential changes, is much larger than the dimensions of the particle. A Langevin equation (cp. Eq. 2.22) can describe the dynamics in such a potential properly in case of an overdamped system (see Sec. 2.2.1) [117, 118].

A Brownian particle in a potential $W(x)$, whose dynamics is given by Eq. 2.22, can escape from such a potential by overcoming the potential barrier at x_B through thermal activation. If the potential barrier W_B is in the order of thermal energies $k_B T$ and the escape thus is a rare process, one can quantify the escape rate by the *Kramers rate*

$$\mathcal{R}_{\mathcal{K}} = \frac{|\Omega_0 \Omega_B|}{2\pi f} \exp\left(-\frac{W_B}{k_B T}\right). \quad (2.25)$$

The inverse of the Kramers rate is equivalent to the *mean first-passage time* [119]. Generally, this time is given by the average time of N independent realizations of an object starting at an arbitrary but fixed position leaving some a priori prescribed domain for the first time [119]. Thus, according to this definition, the first passage time is equivalent to the time an object is trapped in the potential well, when the starting position is given by x_0 and the boundary of the domain by x_B . In the following, the first passage time is also called the *trapping time*.

Thus, taking the inverse of $\mathcal{R}_{\mathcal{K}}$ leads to the average trapping time (see Sec. 4.3.3)

$$\tau \equiv \frac{1}{\mathcal{R}_{\mathcal{K}}} \equiv \frac{2\pi f}{|\Omega_0 \Omega_B|} \exp\left(\frac{W_B}{k_B T}\right). \quad (2.26)$$

2.6.2 Diffusion and the First Passage Time

The diffusion of a single force-free Brownian particle in an overdamped system at thermal equilibrium is always reduced when an additional periodic potential is switched on [120]. Therefore, it might be tempting to conjecture this behavior to systems far from thermal equilibrium. However, the effective diffusion coefficient of a Brownian particle in a periodic potential can become arbitrarily much larger than in the presence of thermal noise alone, if the system is driven away from equilibrium by a static tilting force [121, 122]. An experimental example will be discussed in Sec. 4.4.

The overdamped dynamics of a Brownian particle in a periodic potential $W(x, y)$, tilted along the x -axis, can be described by a Langevin Eq. 2.22 with $W(x, y)$ fulfilling

$$W(x + L, y) = W(x, y), \quad (2.27)$$

where L is the length of the spatial period. The observables of foremost interest are the diffusion coefficient in such a potential and the particle current. For the same reasons, as the current of interest is the current along the channel axis (x axis) (see Sec. 2.4), the diffusion in the tilted periodic potential is also only of interest along the x axis. Hence, the description can be reduced to only one dimension. Moreover, it will be discussed in Secs. 4.3 and 4.4, that the migration of the objects can be described in good approximation along a one dimensional trajectory.

The current and diffusion are typically measured by calculating v and D from averaging particle trajectories as described in Eq. 2.19 and Eq. 2.21. It is also possible, however, to determine both quantities via the mean first passage time. The following expressions are exact, if subsequent escape events are uncorrelated, i.e. if the migration is a *Markov process*. In the experiments, this is indeed the fact, as the DNA molecules have relaxation times much shorter than the migration time from potential minimum to minimum. Moreover, every residence in a potential minimum is a 'reset' to the initial conditions. The details are discussed in Secs. 4.3 and 4.4.

In case of a Markov process, it can be proven that the current and the diffusion are exactly given by [121, 122]

$$\langle \dot{x}(t) \rangle = \frac{L}{\langle t(x_0 \rightarrow x_0 + L) \rangle}, \quad (2.28)$$

$$D = \frac{L^2 \langle t^2(x_0 \rightarrow x_0 + L) \rangle - \langle t(x_0 \rightarrow x_0 + L) \rangle^2}{2 \langle t(x_0 \rightarrow x_0 + L) \rangle^3}, \quad (2.29)$$

where x_0 is an arbitrary reference point, $\langle t^n(x_a \rightarrow x_b) \rangle$ is the n th moment of the first passage time distribution from x_a to $x_b > x_a$ for a stochastic trajectory obeying

Eq. 2.22, and where it is assumed that the static tilt is positive, i.e. the potential declines along the x axis.

2.7 Pitfalls in Particle Tracking

There are several microscopic imaging methods to detect single molecules and particles [123, 124]. Video tracking allows the detailed analysis of their trajectories and thus opens a possibility to quantitatively study migration and diffusion.

There are some obvious pitfalls in particle tracking. The concentration of the objects should be low enough such that always the same molecule is tracked and it is not confused with objects in the vicinity. Moreover, photocleavage of molecules during fluorescence microscopy should be considered as well as the migration out of the focus.

However, there are some more constraints, which might not be so obvious, especially if diffusion coefficients are calculated from trajectories obtained by particle tracking. The position of the particle, determined from an image, e.g. microscopy image detected with a CCD camera, has a statistical error, characterized by an average error σ . This error is due to noise of the CCD chip of the camera and the electronics. In this case, the average quadratic distance is given by (for the derivation see Appendix) [125, 126]

$$\langle R^2(t) \rangle = 2dDt + 2\sigma^2, \quad (2.30)$$

where d is the dimensionality. If the average quadratic distance is used to measure the coefficient of diffusion, the additive factor leads to a correction. Some of the experimental data, relevant to this study, was evaluated with and without the correction, and only marginal differences were found, below the experimental uncertainty. Thus, the correction was not taken into account (see Sec. 4.3.4).

Besides the camera noise, there is the frame rate or exposure time, which should be considered when using video tracking. The exposure time is the time, in which photons are detected and their intensity is summed up. Then the data is read out and the cycle starts again with the exposure. From these images, the position of an object is determined by the location of its center of mass, i.e. the center of averaged light intensity. However, using these images for determining the diffusion coefficient leads to an underestimation of the diffusion, especially for short observation times, as is shown in the following.

Let us consider a freely diffusing Brownian particle. The mean square displacement during one exposure and read out cycle of length t_{cycle} is accordingly $2dDt_{\text{cycle}}$. Because

of the exposure time τ_e , the center of mass position is averaged over a time $\tau_e < t_{\text{cycle}}$. This leads to the fact that the center of mass does not diffuse the mean-square distance $2Dt_{\text{cycle}}$ over one cycle. Instead, the mean square displacement of a particle is given by [126, 127]

$$\langle R^2(Nt_{\text{cycle}}) \rangle = 2dD(Nt_{\text{cycle}} - \tau_e/3), \quad (2.31)$$

where $R(Nt_{\text{cycle}})$ is the location of the averaged center of mass of the N th exposure cycle, $\langle R(Nt_{\text{cycle}}) \rangle = 0$, because of the force-free diffusion, and $N > 2$. Hence, the effect of the exposure time becomes negligible for $Nt_{\text{cycle}} \gg \tau_e$, which is fulfilled in the tracking experiments conducted here (see Sec. 4.3.4).

3 Materials and Methods

3.1 Chemicals and Reagents

The negative photoresist SU-8 (50), SU-8 developer and thinner GBL were obtained from Microresist, Germany. Poly(dimethylsiloxane) (PDMS), commercial name Sylgard 184, consisting of the base polymer and linker, were purchased from Spoerle Electronic, Germany. Glass microscope slides were obtained from Menzel, Germany and 0.4 mm Pt wire from VWR, Germany. Carboxylate modified polystyrene particles (CML) of 1.2 μm , 1.9 μm (fluorescently labeled), 2.0 μm and 2.9 μm diameter were bought from Interfacial Dynamics Corporation, USA. Plasmid DNA (7, 10, 15 and 21 kbp) was a generous gift from PlasmidFactory, Germany. Linear 6 and 12 kbp DNA was obtained from MBBL, Germany, λ -DNA from Promega, USA, and T2-DNA from Fluka, Germany. Disodium hydrogen phosphate dihydrate, sodium chloride, β -mercaptoethanol, N-hydroxysuccinimide (NHS), N-(3-dimethylaminopropyl)-N'-ethyl-carbodiimide hydrochloride (EDC) and L-Histidine were also obtained from Fluka, Germany. Ethylenediaminetetraacetic acid (EDTA) and Tween 20 were purchased from Sigma, Germany. YOYO-1 for DNA staining was obtained from Molecular Probes, USA. The bifunctional poly(ethylene glycol) (PEG) silane SIL-3400 was purchased from Nektar, USA, tridecafluoro-1,1,2,2-tetrahydrooctyltrichlorosilane (TDTS) from ABCR, USA, and performance-optimized polymer 6% (POP-6) from Applied Biosystems, USA. The triblock copolymer Pluronic F-108 was a generous gift from BASF, Germany. For all solutions deionized water from a Milli-Q biocel (Millipore, USA) was used. Acetone was bought from Riedel-de-Haan, Germany, Ethanol from Roth, Germany, sulfuric acid, 2-propanol and hydrogenperoxide from Merck, Germany.

3.2 Production of SU-8 Masterwafer

The microfluidic chip production is realized according to the concept of softlithography [2]. Therefore, a silicon wafer is microstructured via photolithography. A liquid

wafer	U_s [rpm]	τ_s [s]	τ_d [s]
ANM original	1500	16.5	120
ANM acceleration	1400	12	130
DNA dielectrophoresis	2600	21	90

Table 3.1: Parameters of the masterwafer production, where U_s is the spin coating frequency, τ_s the exposure time to UV light, and τ_d the development time.

prepolymer is poured over the wafer having a relief structure on its surface. Then the polymer is cured and peeled off.

A 5 inch silicon wafer, obtained from CrysTec, Germany, was cleaned for 10 minutes in a mixture of 70 % sulfuric acid and 30 % hydrogenperoxid, followed by two times 5 minutes in a water bath. Spincoating at 4000 rpm for 30 seconds in a spin coater (Delta10, Ble-Laboratory Equipment GmbH, Germany) removed the water. Afterwards, the wafer was put onto a hotplate at 200 °C for 20 minutes.

Spin coating After the wafer had ambient temperature, it was placed in a spin coater (spin coater 1001/ST147, Convac, USA) and about 2 ml of photoresist SU-8 (5) were poured onto it. At 500 rpm the resist was spread and subsequently rotated for 30 s at U_s . The parameters are given in Tab. 3.1 for the different wafers produced.

Soft bake and exposure The coated wafer was put onto a hotplate for 3 minutes at 65 °C and 5 minutes 95 °C. For the exposure, it could either be placed in a manual contact unit (designed and home-built by T.T. Duong) or a pneumatic contact unit (designed and home-built by the author, see Sec. 5). The wafer was placed in the unit and the chromium mask (Delta Mask, the Netherlands) on top. The coated wafer and the mask were brought into contact and exposed to the i-line of a Hg-high-pressure lamp (Model 8011, Oriel Corporation, USA) for τ_s .

Post exposure bake Subsequently, the wafer was put onto a hotplate for 3 min at 65 °C and 20 min at 95 °C.

Developing After cooling down, the wafer was placed in a developer bath for τ_d , followed by rinsing with acetone and 2-propanol. Residua were removed with nitrogen.

Hard bake In the end, the wafer was put onto a hotplate for 20 min at 200 °C.

After optical inspection, the wafer was silanized with TDTS. Therefore, the wafer and a few μl of TDTS were placed in an exsikkator, and the pressure was reduced to about 10^{-1} mbar for 30 minutes.

3.3 Production of Microfluidic Chip

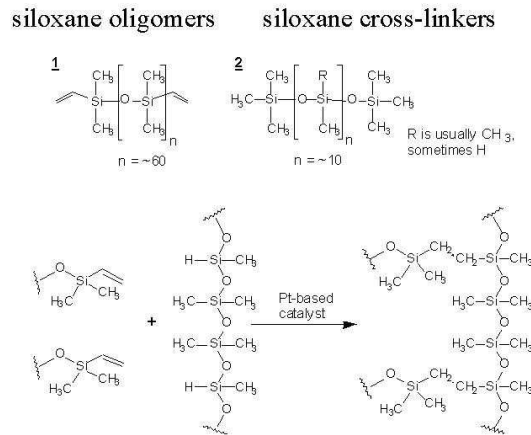


Figure 3.1: Chemical structure of PDMS and the linker. The crosslinking is catalyzed by a Pt-based catalyst [128].

The microfluidic channels were made with poly(dimethylsiloxane) (PDMS). This polymer consists of repeating units of $-\text{OSi}(\text{CH}_3)_2\text{O}-$ (see Fig. 3.1). The base polymer (15 g) was mixed with the linker (1.5 g) at a ratio of 10:1, poured over the masterwafer and baked at $85\text{ }^\circ\text{C}$ for 4h (see Fig. 3.2). The cured PDMS was removed from the wafer and cut to the right dimensions with a scalpel. Reservoir holes were punched with a home-built puncher integrated into a commercial microscope. This way a reproducible, spatial accuracy of about $100\text{ }\mu\text{m}$ could be achieved. The PDMS slabs were then cleaned in a ultrasonic bath in acetone, ethanol and water, and dried with nitrogen. As a substrate, a glass slide was spincoated with about 1 ml PDMS (10:1 ratio polymer:linker) for 30 s at 3000 rpm. Curing was performed on a hot plate at $85\text{ }^\circ\text{C}$ for 30 min. Before chip assembly, the glass slides were also cleaned in an ultrasonic bath in acetone, ethanol and water.

The dimensions of the imprinted microstructures were checked in a scanning electron microscope (JSM-880, Jeol, JP). Therefore, the PDMS was sputtered with $\sim 20\text{ nm}$ layer of Pt (MCS 010, Bal-Tec, Liechtenstein). The pictures were evaluated with the software WinDiss, point electronic GmbH, Germany.

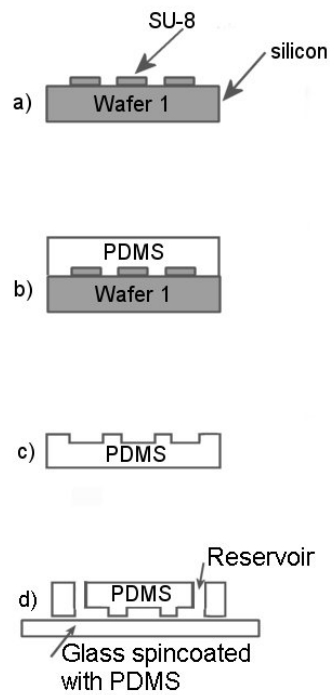


Figure 3.2: Microfluidic chip assembly: (a,b) PDMS was poured over the microstructured Si-wafer and cured at 85 °C for 4 h. (c) The polymer was peeled off and reservoir holes were punched. (d) Oxidation of the PDMS slab and the PDMS coated glass slide and assembly.

3.4 Surface and Sample Preparation

Before chip assembly, the PDMS slab and the PDMS spincoated glass slide were oxidized for 30 s in a home-built plasma chamber, with a pressure of 10^{-1} mbar, at 50 kV with a frequency of 500 kHz and an electrode distance of 6.15 cm. The apparatus is comparable to [129] and was built by W. Hellmich and T.T. Duong.

After oxidation, the PDMS surfaces were assembled and filled with the buffer containing the coating substance after 60 to 120 minutes. For experiments with beads, the chip was filled with F108 (100 μ M for the ANM proof of principle experiment and 500 μ M for all the other experiments) in 100 mM phosphate buffer (pH 8.2). After 2 to 20 h, the coating was replaced by the working buffer. For the proof of principle experiment, pure 100 mM pH 8.2 phosphate buffer was used (see Sec. 4.1). For the ANM separation (see Sec. 4.1.2) and the ratchet experiment (see Sec. 4.2), the working buffer contained 200 μ M Tween 20, 100 μ M L-histidine and 100 mM phosphate buffer at an pH of 8.2. For the ANM acceleration experiments (see Sec. 4.1.3) the working buffer consisted of 200 μ M Tween 20 and 100 mM phosphate buffer pH 8.2. Prior to usage, the beads were washed with water three times and resuspended in fresh buffer solution. Only the 2.9 μ m beads in the ANM separation experiment were chemically modified. They were reacted with butylamine in a concentration of 89 mM for 90 min under continuous shaking with a Vortex in 100 mM phosphate solution (pH 8.3) containing 2.2 mM NHS and 44 mM EDC.

For the DNA experiments, the microchannels were coated with PEG-3400 (3 μ M) for 20 min. The working buffer, replacing the coating, contained 1 mM EDTA, 22 mM NaCl, 0.1 % (v/v) POP-6 and 10 mM phosphate solution (pH 8.3). Additionally, the DNA solutions contained 2 μ l/ml β -mercaptoethanol and 1 YOYO-1 molecule per 10 base pairs.

Only for the salt and YOYO-1 dependence of the polarizability (see Secs. 4.3.6 and 4.3.7), the composition of the buffer was varied from the constitution given above. The low ionic solutions for the dependence of the polarizability on ionic strength were prepared with MilliQ water and the addition of NaCl, the other solutions were prepared with phosphate buffer (10 mM, 20 mM NaCl) and the addition of NaCl (see Tab. 3.2). The ionic strength of the MilliQ was estimated from the conductivity of 0.3 mS/cm with the empiric relation $I = 1.6 \cdot 10^{-5} \times \sigma_c$, where I is the ionic strength and σ_c the specific conductance [130]. The solutions for the YOYO-1 dependence of the polarizability were only varied concerning the YOYO-1 concentration.

Prior to each experiment, the reservoirs were emptied and a Plexiglas (PMMA) holder

	additional NaCl [mM]	I [10^{-2} M]
water	0	0.48
water	5	0.74
water	10	0.99
water	20	1.48
10 mM phosphate buffer	22	2.21
10 mM phosphate buffer	50	3.73
10 mM phosphate buffer	80	4.74

Table 3.2: Buffer and salt concentrations used in the experiments to elucidate the ionic strength dependence of the polarizability.

kbp	ccc monomer [%]	ccc dimer [%]	oc [%]	linear [%]
7,0	88.4	9.8	1.8	n.a.
10,3	85.7	12.8	1.5	n.a.
15,5	94.5	4.9	0.6	n.a.
21,0	92,1	7.4	0.5	n.a.
12,2 (PJP2)	82.8	13.3	n.a.	3.9

Table 3.3: Composition of the supercoiled plasmid DNA samples determined by capillary gel electrophoresis [131].

with adequate reservoirs was placed on top of the chip. The PDMS adhered to the PMMA tightly, but reversibel, thus increasing the reservoir volume and holding the Pt electrodes in place. The PMMA block was $56 \times 80 \times 5 \text{ mm}^3$, with 2 mm access holes and 0.5 mm drillings at each reservoir under an angle of 45° for holding the Pt electrodes, which ended in the reservoir.

The supercoiled DNA samples were composed as shown in Tab. 3.3, quantified by capillary gel electrophoresis. In order to study the spatial configuration, AFM images of the plasmids were taken. Mica was silanized with APTES in an exsikkator. Sample volumes of $2 \mu\text{l}$ were incubated on the surface for 4 minutes at a sample concentration of $1 \mu\text{g}/\text{ml}$. The images were taken in tapping mode with a NanoScope IIIa multimode AFM, Digital Instruments, USA.

The PJP2 12,2 kbp plasmid was prepared by Rafael Szczepanowski (Genetics Department, Bielefeld University). The DNA was isolated with the QIAprep Spin Miniprep Kit, Qiagen, Germany, according to the protocol of the manufacturer, and linearized if required with KpnI. The quality of the plasmid preparation was checked by agarose

gel electrophoresis (1 % agarose, run time 1 h, 120 V, 40 mM Tris, 20 mM acetic acid, 1 mM EDTA) and capillary gel electrophoresis (parameters given in [132], see also Sec. 4.3.2 for an example of the original data).

3.5 Experimental Setup

The experimental setup is schematically shown in Fig. 3.3 and was based on an inverted microscope (Axiovert 200, Zeiss, Germany) with a motorized x/y stage (99S008, Ludl Electronic Products, USA) combined with a CCD camera (Imager 3L, LaVision technically identical with SensiCam, PCO) and a mercury arc lamp (HBO50). A SensiCam PCI interface board (PCO, Germany) was used as a video grabber card together with the Davis 6.2 software from LaVision for image acquisition. For the ANM experiments, a 20 fold objective (Zeiss LD ACHRO PLAN 20x/0,40 Korr) was used, whereas a 40 fold objective (Zeiss LD ACHRO PLAN 40x/0,40 Korr) was used to determine the diffusion coefficient of the beads. For all DNA experiments, a 100 fold oil immersion objective (PLAN Neofluar, NA 1.3, Zeiss) was used. The fluorescent filter set consisted of a BP 450-490, a FT 510 and a BP 515-565 filter, all from Zeiss, Germany. Additionally a gray filter (25 % transmittance) was used for the migration and diffusion experiments with DNA to avoid photocleavage.

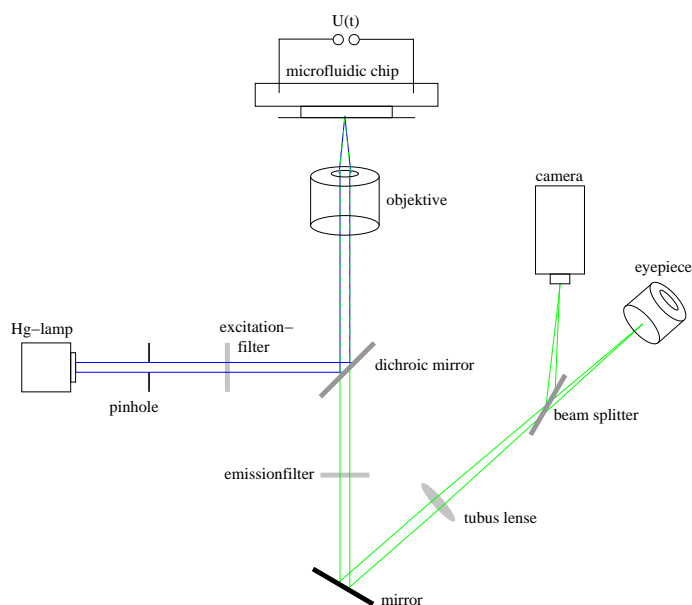


Figure 3.3: Standard optical fluorescence setup with voltage source connected to the microfluidic chip.

A second computer controlled the power supplies via Labview 6i programs. For the

ANM experiments MCN 14-2000 and MCN 140-1250 power supplies from F.u.G., Germany were used. The ac and dc electric fields in the DNA experiments were accomplished with a DAQ card 6036E (National Instruments, USA) combined with a high voltage amplifier (600H, NanoTechTools, Switzerland). Additionally two power supplies F.u.G. HCL 14 -12500 were used for generating dc voltages needed during injection. All sinusoidal and square-wave voltages have to be read as peak-to-peak values.

3.6 Experimental Procedures

3.6.1 Polystyrene Particle Procedures

Diffusion The Brownian motion of about 20 non-interacting beads was recorded in the microfluidic chip over 60 s with the 40 fold objective with 10 frames per second (fps) and a binning of 2 by 2 pixels. The trajectories of the particles were then evaluated with a particle tracking software (ImageJ with the plugin multiple tracker 2 by N. Stuurman [133]). From the plot of the mean square distance traveled versus time, one could calculate the linear regression and thus the free diffusion coefficient (see Sec. 2.3).

Mean free mobility For an applied voltage, the migration of particles between two traps (narrow constrictions) in the microfluidic chip was recorded at 10 fps with a binning of 2 by 2 pixels. With the known travelled distance, the mean free velocity was calculated for an average of 40 particles per voltage value.

Measuring ANM For all ANM experiments a square wave voltage $U(t) = U_{ac}(t) + U_{dc}$ was applied with a period of $2\tau_d$ to the microfluidic chip. Over four time periods, the migration of about 40 particles was recorded with the 20 fold objective at 3 fps and a binning of 2 by 2 pixels. Afterwards, the drift velocity was checked, balanced if needed, and another U_{dc} value applied. Finally, the image sequences were evaluated via particle tracking.

Ratchet effect For the ratchet experiments, three different particles species (diameters 1.2, 1.9 and 2.9 μm) were injected and the drift was balanced, if necessary. Then a voltage $U(t) = U_{ac}^{\text{fast}} \sin \omega_{\text{fast}} t + U_{ac}^{\text{slow}}(t) + U_{dc}$ was applied with an amplitude $U_{ac}^{\text{fast}} = 150$ V of frequency $\omega_{\text{fast}} = 60$ Hz and a square-wave voltage of amplitude $U_{ac}^{\text{slow}} = 12$ V with a frequency of $\omega_{\text{slow}} = 0.25$ Hz. The migration of the beads was recorded with a 20 fold objective at 10 fps and a binning of 2 by 2 pixels. The average traveling velocity was afterwards determined by manual tracking.

3.6.2 DNA Procedures

Diffusion The DNA was injected into the channel via a pinched injection protocol [17]. The cross injector delivered defined sample volumes of ≈ 60 fl. The DNA was highly diluted (≈ 10 pM) assuring single molecule diffusion without interactions with other DNA molecules. The Brownian motion of 30 DNA molecules over 6 s was recorded with the 100 fold objective at 10 fps at a binning of 4 by 4 pixels. The trajectories were evaluated via particle tracking with ImageJ and the plugin multiple tracking 2 by N. Stuurman. The mean square travelled distance was plotted versus time and the diffusion coefficient calculated from the linear regression (see Sec. 2.3).

Mean free velocity For an applied voltage, the migration of DNA molecules between two traps (narrow constrictions) was recorded at 10 fps with a binning of 8 by 8 pixels. With the known travelled distance, the mean free velocity was calculated for an average of 20 DNA molecules per voltage value.

DNA polarizability The field of observation was chosen $140 \mu\text{m}$ from the cross injector. In order to obtain the polarizability of a DNA sample, the DNA solution (≈ 20 pM) was injected with a constant $U_{dc} = 12$ V. Then an image sequence of the migrating DNA molecules was recorded for different U_{ac} . Afterwards, the time needed for 30 DNA molecules from entering one trap to entering the next was determined. Subtracting the time needed for the free migration in between two traps, led to the trapping time, the time a molecule spent localized in a trap. The trapping time plotted logarithmically versus the applied U_{ac}^2 allowed to calculate the polarizability from the slope of the linear fit with logarithmic corrections (see Sec. 4.3.3).

DNA diffusion enhancement The DNA solution (≈ 20 pM) was injected with an $U_{dc} = 6$ V and a constant $U_{ac} = 240$ V. After 70 s for the λ -DNA and after 30 s for the T2-DNA, the U_{dc} was increased to the target value. The region of interest (ROI) was chosen such that the DNA, trapped during the $U_{dc} = 6$ V period, was not in the ROI. The image sequence of the migrating DNA molecules was recorded with 10 fps and a binning of 8 by 8 pixels. Afterwards the first and second moment of the distribution of mean first passage times, approximated by the average time 30 DNA molecules needed from entering a trap to entering the next, was manually determined and the diffusion coefficient calculated (see Sec. 4.4).

DNA separation The DNA sample consisting of two or three different DNA species was injected via pinched injection with a constant $U_{dc} = 12$ V. During the migration of the DNA through the post array, the U_{ac} was stepwise increased from U_{start} every τ_{inc} by U_{inc} up to U_{end} . Then the U_{dc} was switched off and $U_{final} = 420$ V applied, thus

creating a steady trapping state. Then the motorized stage was set into motion with $10 \mu\text{m/s}$ and the separation channel was scanned for fluorescence signals. The video data was recorded with 3 fps and a binning of 8 by 8 pixels and evaluated with a script in Davis own CL language.

Stroboscopic time series The ac field had a frequency of $\omega = 60 \text{ Hz}$. The camera was set to record 59.4 ± 0.05 frames per second. Thus, a beat could be observed because of the slightly shifted frequencies of the electric field and the camera, if the DNA followed the motion of the electric field.

3.7 Automated Evaluation of Trapping Times

As described in Sec. 3.6.2, so far, the trapping times were evaluated manually. Here, an automated evaluation procedure is developed. The DNA is injected via pinched injection and video sequences for a constant U_{dc} but different U_{ac} are recorded, especially one with $U_{ac} = 0 \text{ V}$. The fluorescence intensity of the migrating DNA is measured in a narrow ROI inbetween two rows of traps for every recorded image and results in a temporal intensity distribution $H(t_i)$. As the intensity is directly proportional to the number of DNA molecules, assuming that the DNA sample was homogeneously stained and all DNA molecules had the same length, one can calculate the mean migration time of DNA from a defined starting position to the position of the ROI

$$\langle t \rangle = \frac{\sum_i H(t_i) \cdot t_i}{\sum_i H(t_i)}. \quad (3.1)$$

Here, this value is the average migration time of the DNA molecule ensemble from the injector up to the ROI. It can be shown (see Appendix for its theoretical derivation) that this time is equal to the sum of the free migration time of DNA molecules outside the traps (t_{free}), and the time (τ) they spend in a trap times the number of traps (N) passed,

$$\langle t \rangle = \tau N + t_{free}. \quad (3.2)$$

The time t_{free} can be measured from $t_{free} = \langle t(U_{ac} = 0) \rangle$. Thus, the trapping time can be calculated with

$$\tau = \frac{\langle t \rangle - t_{free}}{N}. \quad (3.3)$$

This procedure was programmed by L. Bogunovic [134] with a master script written in Perl controlling the image operations in ImageJ and the calculations in a C-program. In order to validate the automated analysis, several data sets were analysed manually and

automatically, and the results are in very good agreement within the experimental error bars, as, for example, shown in Fig. 3.4. Hence, in the section 'Results and Discussion', it is not differentiated between manually and automatically determined trapping times.

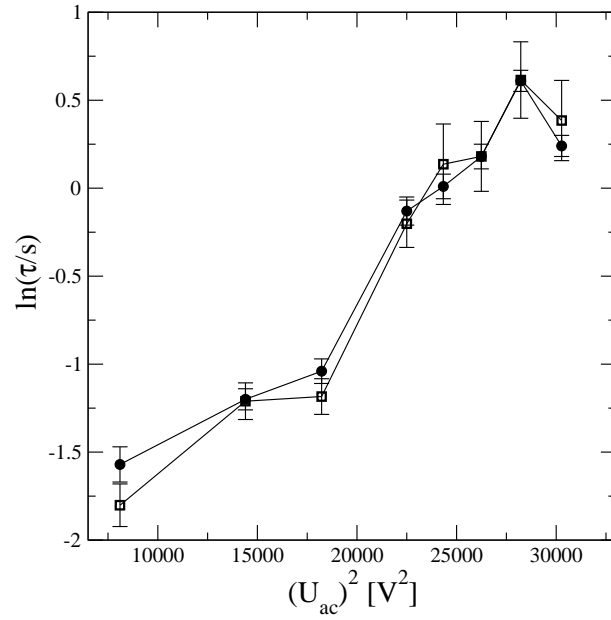


Figure 3.4: Comparison of the trapping times analyzed manually (circles) and automatically (boxes). The results agree very well within the error bars.

4 Results and Discussion

The leitmotif of this work is to exploit thermal noise for bioanalysis in microfluidic systems operating far from thermal equilibrium. In this context, the results of four different projects are presented and discussed. In Sec. 4.1, the fractionation of particles with the paradoxical migration phenomenon *Absolute Negative Mobility* (ANM) and its acceleration is demonstrated. ANM was theoretically predicted by Eichhorn et al. [107, 108] for non-interacting Brownian particles. In Sec. 4.2, an Electrodeless Dielectrophoretic Ratchet is presented and discussed concerning its ability to separate colloidal particles with a 'tunable' separation criterion. In Sec. 4.3 a new method is demonstrated for separating DNA according to its polarizability. The DNA migration is studied in more detail, following the theoretical work of Ajdari and Prost [115], who predicted DNA separation in a tilted periodic potential. Based on this analysis, a new method for the quantitative determination of DNA polarizability is developed. This new technique is applied to study the dependence on various parameters, e.g. salt and dye concentration, frequency, DNA conformation and scaling with length. Finally the giant diffusion of DNA in a tilted periodic potential is demonstrated in Sec. 4.4, which was theoretically predicted by Reimann et al. for point-like particles [121, 135] and possible applications for mixing and purification are discussed.

4.1 Absolute Negative Mobility (ANM)

When applying a static force to a system at rest, a net motion opposite to that force - termed Absolute Negative Mobility (ANM) - seems impossible due to Newton's second law. Yet, such a paradoxical response phenomenon has been observed experimentally in semiconductor devices [104, 105] and has been predicted theoretically in simplified stochastic model systems [107, 136, 137] (see also Sec. 2.4).

Here, the main focus is set on the acceleration and application of ANM for the fractionation of colloids. First results have already been given in [138], but for a conclusive view, all results concerning the ANM of single Brownian particles are presented.

4.1.1 Proof of Principle

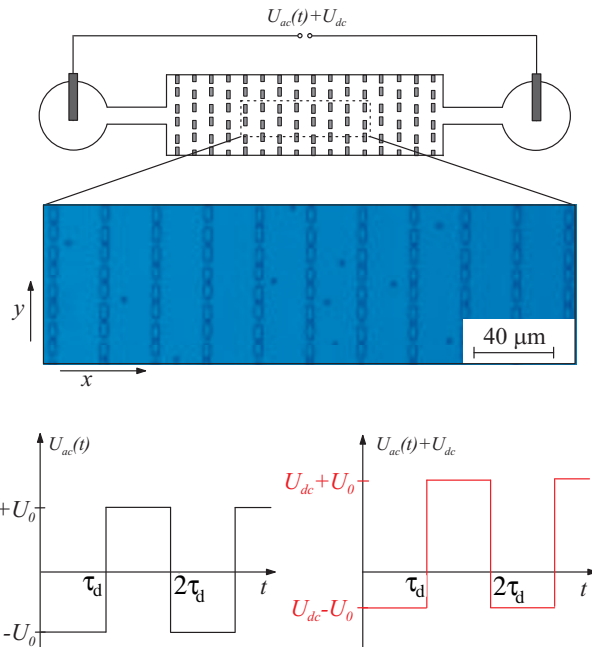


Figure 4.1: Schematic top view of the experimental setup (not to scale). Electrodes are immersed into the two reservoirs of 2 mm diameter. Those are connected by inlet and outlet channels of 2.5 mm length and $24 \times 9 \mu\text{m}^2$ cross section each and a central, microstructured part. It extends over $6000 \times 400 \mu\text{m}^2$ in the $x - y$ -plane and $9 \mu\text{m}$ in height and contains periodically arranged rows of posts. The enlargement shows an optical micrograph of the posts (bright, rectangular) with particles (dark dots) of $2 \mu\text{m}$ diameter. In each row of posts the gaps are alternately smaller and larger than the particle diameter. Along the x -axis, the gaps are in line and again alternately large and small. An alternating voltage $U_{ac}(t)$ switches periodically between $\pm U_0$ with period $2\tau_d$, resulting in an unbiased non-linear particle dynamics far from thermal equilibrium. Superimposing a static dc voltage U_{dc} gives rise to a biased total voltage.

To provide a proof-of-principle for single Brownian particle ANM, a microfluidic device was designed consisting of periodically arranged posts with alternating small and large gaps (see Fig. 4.1, for methods see Sec. 3). Negatively charged particles of $2 \mu\text{m}$ diameter are suspended in the buffer solution in low concentration so that particle-particle interactions are negligible (see Sec. 2.2.5). The particle diameter and the width of the small and large gaps have been chosen such that the particles can pass through the large gaps but not through the small ones. Electric fields are generated by applying a voltage along the x -axis so that a positive voltage induces a positive force on the beads along the x -axis. Applying an alternating voltage $U_{ac}(t)$ that switches periodically between $\pm U_0$, there is no net motion of the particles for symmetry reasons.

This setup represents the unperturbed non-equilibrium system at rest. But what will be the average migration velocity v in the x direction in response to a static perturbation voltage U_{dc} superimposed on $U_{ac}(t)$ (see Eq. 2.21)?

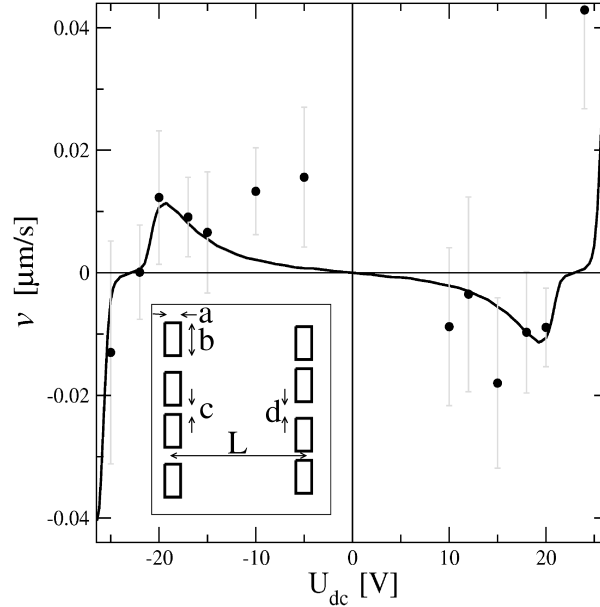


Figure 4.2: Absolute negative mobility of $2 \mu\text{m}$ particles in the microfluidic device specified by the inset ($a = 3.1 \mu\text{m}$, $b = 6.1 \mu\text{m}$, $c = 1.7 \mu\text{m}$, $d = 3.1 \mu\text{m}$, and $L = 22.5 \mu\text{m}$) with $U_0 = 30 \text{ V}$ and switching time $\tau_d = 25 \text{ s}$ of the ac voltage. Dots with error bars: experimentally observed average migration velocity along the x axis. Solid black curve: theoretical response characteristics obtained from numerical simulations (see Sec. 2.5).

In order to answer this question, the average velocity (Eq. 2.21) was approximated by observing about 40 particles over 4 periods of the ac-driving for different values of the static perturbation U_{dc} (see Sec. 3.6.1). This yields the experimental response characteristics in Fig. 4.2. The experimental uncertainty is mostly due to the limited number of recorded particles, but also deviations from strictly spatially periodic conditions and bead-to-bead variations of size and surface charge.

The key feature of the resulting response curve is the negative slope symmetrical around the origin, a distinct and unambiguous signature of ANM (see Sec. 2.4 for distinction from other non-intuitive transport phenomena). For not too large static voltages U_{dc} , the particle is always moving in the direction opposite to the corresponding static force. Increasing U_{dc} to large static forces, the velocity in this 'wrong' direction slows down, passes through zero and finally points in the 'normal' direction.

To explain how ANM occurs, let us consider the small gaps as traps because the electric field lines can pass through but the particles cannot. For $0 < U_{dc} < U_0$, the

alternating total voltages $\pm U_0 + U_{dc}$ yield a back and forth motion of the particles along the x direction. For convenience, the direction of motion in case of $+U_0 + U_{dc}$ is called the 'fast' direction, and in case of $-U_0 + U_{dc}$ it is called the 'slow' direction ($| -U_0 + U_{dc} | < | +U_0 + U_{dc} |$).

Whenever a particle succeeds in passing through a large gap, it is trapped by the adjacent small gap, unless it thermally diffuses sufficiently far in the y direction to proceed through another large gap. The smaller the voltage, the more time it has to diffuse and the farther it can travel before being trapped. As $| +U_0 + U_{dc} | > | -U_0 + U_{dc} |$, the particle becomes trapped after moving forward a short distance when $+U_0 + U_{dc} > 0$, whereas it travels backwards for a longer distance when $-U_0 + U_{dc} < 0$, resulting in ANM (see also Fig. 4.3).

To theoretically model the experiment, it is simulated by numerically solving the stochastic differential equations Eq. 2.22 with $W \equiv 0$ (see Sec. 2.5 for details). However, for a quantitative comparison of the experiment and the simulation, two gauge factors are necessary, q which sets the effective coupling of the particle to the electric field and f the effective coupling to the thermal environment. These can be obtained by reproducing the experimentally determined diffusion coefficient of $D = 0.63 \cdot 10^{-13} \text{ m}^2/\text{s}$ and a voltage dependent velocity in x -direction of $v_0 = U \cdot 2.3 \cdot 10^{-7} \text{ m/Vs}$, where U denotes the voltage applied to the electrodes (see Methods Sec. 3.6.1). The resulting numerical velocities are shown as the solid curve in Fig. 4.2. Within the experimental uncertainty, the agreement of experiment and simulation is very good.

4.1.2 Particle Separation by ANM

Having thus established the reliability of the model, the simulation is used to demonstrate that ANM can coexist with the 'normal' response under identical experimental conditions in the experimental setup discussed in Sec. 4.1.1. Thus, two different particle species can simultaneously be moved into opposite directions, i.e. they can be fractionated. With this insight, the experiment is tackled with driving parameters U_0 and τ_d that demonstrated particle separation in the simulation. The experimental particles are characterized in Tab. 4.1.

Simultaneously, the two particle species are hydrodynamically injected into the microfluidic device and thus are exposed to identical experimental conditions. The average migration velocity for different values of U_{dc} is shown in Fig. 4.4. The remarkable feature is the qualitatively different migration behavior of the two particle species. While the $2.9 \mu\text{m}$ particles follow the direction of the average force, i.e. proceed farther in the

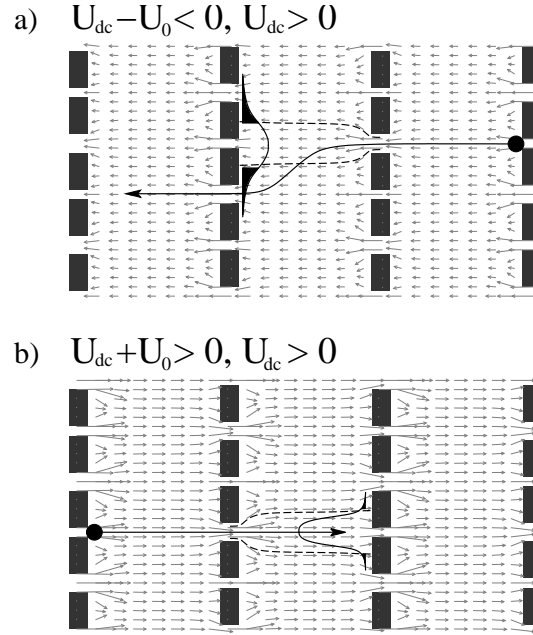


Figure 4.3: Intuitive explanation of ANM for a positive static dc voltage U_{dc} on top of the ac drive. (a) Schematic motion of a particle during any half period of duration τ_d with total voltage $U_{dc} - U_0 < 0$. The grey arrows indicate direction and magnitude of the corresponding force field. Although the field lines can pass through the small gaps, the particle cannot. Hence, these gaps act as deterministic traps. For one trap, the border of the attraction basin, also called separatrix, is indicated by dashed lines. It is obtained from closer inspection of the electric field. Once the particle is trapped, the probability to escape by thermal noise is negligible. In order to avoid such a trap, the particle has to diffuse over the basin-boundary during its traveling time from one row of posts to the next. The probability of doing so is indicated by the tails of the distribution (black colored). (b) Motion of the particle during a subsequent half-period with total voltage $U_{dc} + U_0$. Since $U_{dc} > 0$, the total voltage and hence the forces are larger in modulus than in (a) and of opposite sign. Accordingly, the traveling time from row to row is shorter and the diffusive dispersion in y -direction narrower than in (a). Likewise the probability of avoiding a trap is smaller and hence the average traveling distance. The overall result is a net motion in the negative x direction, i.e. opposite to the positive static voltage U_{dc} .

Diameter [μm]	v_0 [$\mu\text{m}/\text{s}$]	D [$\mu\text{m}^2/\text{s}$]
1.9	0.28 ± 0.03	0.131 ± 0.005
2.9	0.14 ± 0.01	0.082 ± 0.007

Table 4.1: Particle velocity v_0 when applying a constant voltage $U_* = 1$ V and diffusion coefficient D of the particles.

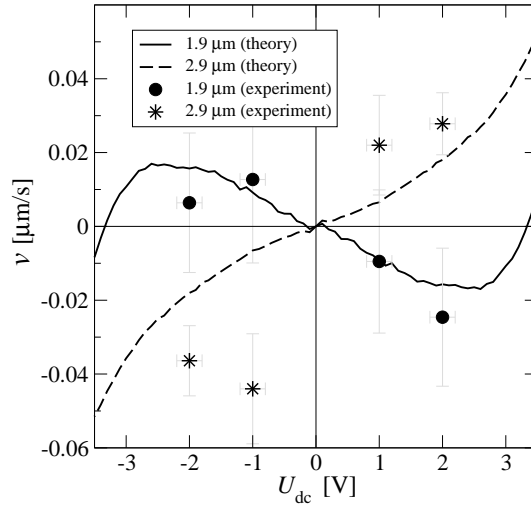


Figure 4.4: Simultaneously observed average particle velocities for the two particle species characterized in Tab. 4.1 with driving parameters $U_{ac} = 5$ V and $2\tau_d = 140$ s. The $1.9 \mu\text{m}$ particles (dots) show ANM, whereas the $2.9 \mu\text{m}$ particles (stars) show 'normal' behavior. The curves result from numerical simulations of the two particle species, the symbols represent experimental measurements.

fast direction when $U_+ \equiv +U_0 + U_{dc}$ with $U_{dc} > 0$ is applied, the $1.9 \mu\text{m}$ particles at the same time run into the direction opposite to that force, i.e. proceed farther in the slow direction when $U_- \equiv -U_0 + U_{dc}$ with $U_{dc} > 0$ is applied.

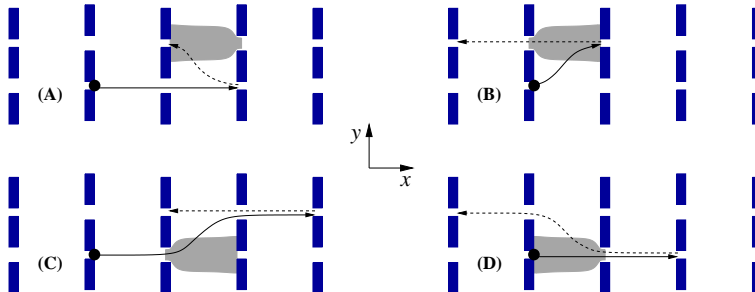


Figure 4.5: Sketches of typical particle trajectories in the microstructure, where particles avoid just one gap during the switching time τ_d ($U_{dc} > 0$). The starting positions are marked by black dots. The solid and dashed arrows correspond to the fast and slow migration direction during the application of $U_{ac}(t)$ (see Fig. 4.1). (A),(B): The particle avoids the first large gap by entering the basin of attraction (gray region) of an adjacent small gap due to lateral diffusion during the slow (A) or the fast (B) phase of the driving. (C),(D): The particle goes through the large gap, but then avoids the small gap by leaving its attraction basin during the fast (C) or the slow (D) phase of driving. The processes (A) and (C) yield a net displacement of one row distance in the positive x direction, whereas in (B) and (D) the particle moves by one row in the negative x direction, corresponding to ANM.

Further inspection identifies four different possible paths that lead to a net displacement of one obstacle row in the positive or negative x direction during a driving period

by avoiding just one gap. They are illustrated in Fig. 4.5. For a specific process to occur, the particle must be able to pass at least the required number of post rows along the x axis during the switching time τ_d . For instance, for process (D) the particle must be able to proceed at least by two post rows in order to reach the second large gap within the time τ_d in the slow direction (see the dashed arrows). This yields the condition $\tau_d \gtrsim (2LU_*)/(v_0 |U_-|)$ or

$$\frac{v_0}{U_*} \gtrsim \frac{2L/\tau_d}{|U_-|}, \quad (4.1)$$

where U_* is the reference voltage at which v_0 has been measured. For the remaining three processes in Fig. 4.5 either the minimal required traveling distance is smaller (processes (A) and (B)) or this distance is travelled during the fast switching period (process (C)). On the one hand, the condition given by Eq. 4.1 thus guarantees the occurrence also of the less frequent processes (A), (B), (C), on the other hand, these three processes still do occur if the condition 4.1 is violated. For the $1.9 \mu\text{m}$ particles condition 4.1 is fulfilled under the experimental conditions specified in Fig. 4.4 for $|U_{dc}| \leq 3 \text{ V}$. Hence, process (D) is the most probable one, explaining the migration opposite to the static force. In contrast, the $2.9 \mu\text{m}$ particles do not fulfill condition 4.1, such that the dominating migration processes are (A) and (C) of Fig. 4.5, leading to a migration in the direction of the static force.

The discussion above of the different migration processes is restricted to paths with just one avoided gap per switching period τ_d . Processes that avoid more traps are possible but unlikely. The probability of avoiding n traps in a row quickly decreases with the probability for avoiding one trap to the power of n [107]. Moreover, for multiple gap avoidances the particle must be able to travel the necessary distance in x direction during the time τ_d , which would require larger τ_d than used here. Thus, the paths with several avoided traps can safely be neglected in the above qualitative discussion.

4.1.3 ANM Acceleration

The so far observed maximum ANM velocities are typically in the range of 10-20 nm/s. The reason for this slow average migration can be found in the small diffusive dispersion leading to very small probabilities of avoiding a trap. Therefore, the first obvious way to accelerate ANM is to use smaller particles. However, this requires a concomitant down-scaling of the post array dimensions, such that the gaps keep their trapping properties for the smaller particles. Moreover, the faster diffusion leads to a larger probability of leaving the attraction basin of the trap also in the fast direction, thus diminishing ANM. Hence, the driving parameters have to be adapted as well; in particular, a higher

amplitude U_0 has to be chosen. This higher amplitude allows using shorter driving periods $2\tau_d$, leading again to enhanced ANM velocities because the frequency of heading toward a trap is increased and thus the probability per time for avoiding a trap. Note, that for the occurrence of ANM, the particle must be able to travel at least the distance between two traps within the time τ_d specifying a lower limit for τ_d (see also previous Sec.). This discussion shows that there are no simple scaling laws for the ANM velocity (see also theoretical analysis in [107, 108, 139]), but that the ANM effect depends on all the details of the setup. On the other hand, this complex interplay between system properties is the basis for its flexibility to guide different particles into opposite direction under identical driving conditions.

Another approach to accelerate ANM is to decrease the lateral size of the attraction basin of the traps by an optimization of the geometry. As discussed before, the probability of avoiding a trap is given by the width of the basin of attraction and the time the particle can diffuse in lateral direction during its motion from one row of posts to the next. Given fixed driving parameters, this probability can be enhanced by, first, a reduction of the diffusion distance necessary to leave the attraction basin and, second, by guaranteeing that once a bead escapes from the attraction basin, the probability of diffusing back is small.

The first point can be achieved by decreasing the width of the posts in y direction. A closer analysis shows, however, that size reduction is limited: if the posts become too small, pathways along the electric field lines arise that lead to deterministic meandering through the post array, completely destroying the basic ANM mechanism. A similar effect was found in a ratchet array by Huang et al. [140] and identified to be responsible for the prevention of ratcheting of small molecules.

The second point is based on the observation that most of the particles diffusively leave the attraction basin of the trap only shortly before they hit one of the posts adjacent to the trap. Therefore, if in this region the motion toward the large gap is favored by a suitable shape of the posts, a diffusion back into the basin is unlikely, and ANM can be enhanced.

Thus, there are two concepts to enhance ANM: reducing the post width and changing the post shape. Tab. 4.2 summarizes the dimensions of the original design (design-1) and the newly developed designs (design-2 to -4) (see insets of Fig. 4.6).

Design-2 consists of square posts, whose width is reduced to 66 % of that of the original design (design-1) with a post width of $6.1 \mu\text{m}$. The square posts thus have a width of $4 \mu\text{m}$, representing the smallest width achievable with the lithography equipment used here. Design-3 displays rhomb-like shaped posts. The width of those posts

Layout	Design-1 (rectangles) (sim and exp)	Design-2 (squares) (sim)	Design-3 (rhomb-like) (sim)	Design-4 (rhomb-like) (sim and exp)
Periodicity (L)	25.6 μm	26 μm	27 μm	27.0 μm
Post size ($b \times a$)	$6.1 \times 3.1 \mu\text{m}^2$	$4 \times 4 \mu\text{m}^2$	$6 \times 6 \mu\text{m}^2$	$4.9 \times 3.8 \mu\text{m}^2$
Small gap (c)	1.7 μm	1 μm	1 μm	2.2 μm
Large gap (d)	3.1 μm	4 μm	3 μm	5.3 μm
Width of attraction basin	7.3 μm	4 μm	5 μm	5.1 μm

Table 4.2: Dimensions of the post designs used in simulations (sim) and experiments (exp). Posts in all experimental designs are 9 μm high. The width of the attraction basin was determined by careful inspection of the deterministic particle migration in the simulation.

(6 μm) is comparable to the width of design-1 (6.1 μm). Design-4 corresponds to the experimentally realized post shape combining both concepts.

In these new designs-2 and -3, simulations are performed with 1.9 μm particles, which were used and characterized in the ANM separation experiment (Sec. 4.1.2), to check if the expected acceleration of ANM can be observed and to compare the velocities with the previously obtained data from design-1. The results of the simulations are shown in Fig. 4.6.

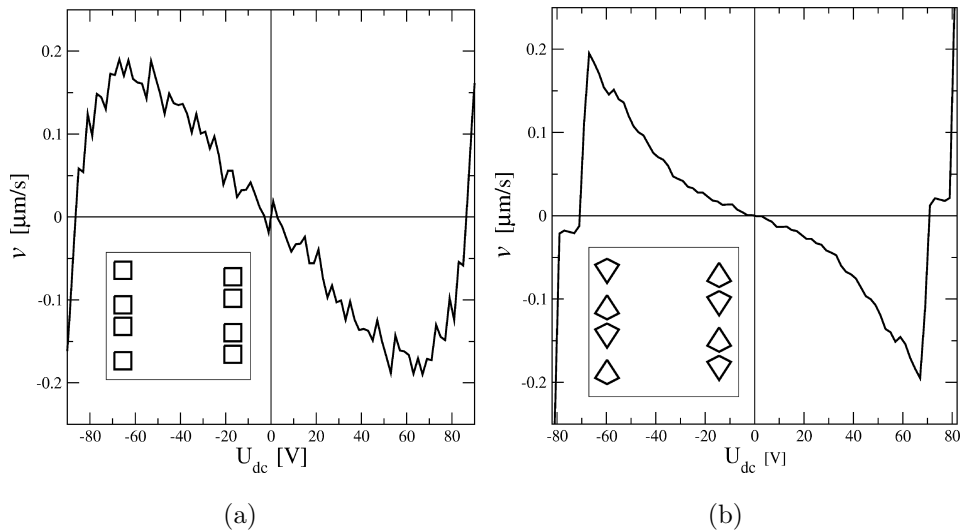


Figure 4.6: (a) Simulation of the new design-2 with squared posts ($U_0 = 120 \text{ V}$, $2\tau_d = 32 \text{ s}$). (b) Simulation of the new design-3 with rhomb-like shaped posts ($U_0 = 90 \text{ V}$, $2\tau_d = 20 \text{ s}$). In (a) and (b), an increase in velocity by one order of magnitude is observed compared with Fig. 4.2 for beads of similar size. For details on the geometry shown in the insets, refer to Tab. 4.2.

Both new geometries demonstrate an increase in velocity of more than one order of magnitude compared to the original design (see Fig. 4.2). For the square posts (design-2), this is attributed to the reduced dimension of the basin of attraction. The width is reduced from $7.3 \mu\text{m}$ in the original design to $4 \mu\text{m}$ in design-2 (see Fig. 4.7 and Tab. 4.2). On the other hand, the same enhancement occurs in design-3, where only the shape of the posts is changed retaining the post width. As can be seen from Fig. 4.7c and Tab. 4.2, the rhomb-like post structure with sharp apexes in design-3 results in a width of the attraction basin of $5 \mu\text{m}$, which is 32 % smaller than in design-1. This means that not only the post width and the resulting ratio of trap-to-gap width determines the width of the attraction basin, but also the shape of the post.

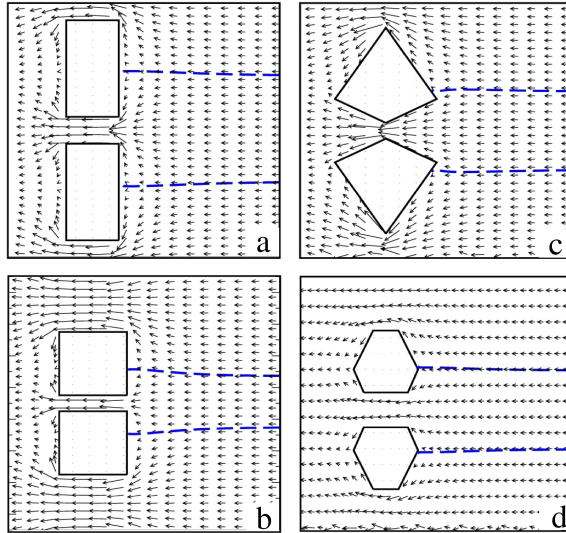


Figure 4.7: Schematic drawings of geometric traps of design-1 to -4 representing 16 by $16 \mu\text{m}^2$. The arrows indicate the strength and direction of the electric field. The dashed lines are the boundaries of the deterministic attraction basin of the small gaps. The width of the attraction basin is determined by careful inspection of the electric field lines.

With this insight, design-4 is experimentally realized, which incorporates both concepts of enhancing ANM. The posts have a rhomb-like shape with truncated apexes and a final width of 75 % compared to design-1. Due to limitations of the lithography process, the trap width results in $2.2 \mu\text{m}$, which is slightly larger than expected. The experiment is thus carried out with $2.9 \mu\text{m}$ particles. Fig. 4.8 shows the ANM response of about 160 driving periods for each data point. All determined velocities up to $U_{dc} \approx 60 \text{ V}$ demonstrate ANM. The experimental error bars are due to the limited number of particles and observation time. Fig. 4.8 also shows a simulation curve, for which the actual dimensions of the experimental posts are approximated by the shape

as shown in Fig. 4.7(d) and characterized in Tab. 4.2. The agreement of experiment and simulation is very good. The comparison of design-1 with design-4 results in an increase in the maximum velocity by a factor of 7. This is remarkable because the diffusion of the $2.9 \mu\text{m}$ particles is lower by 37 % compared with the $1.9 \mu\text{m}$ particles used in measurements of design-1.

It is interesting to note that the width of the attraction basin in design-3 and -4 results in a similar value (5 and $5.1 \mu\text{m}$ respectively), although the post width is reduced in design-4. This demonstrates that the width of the basin of attraction also depends on the ratio of the trap-to-gap width.

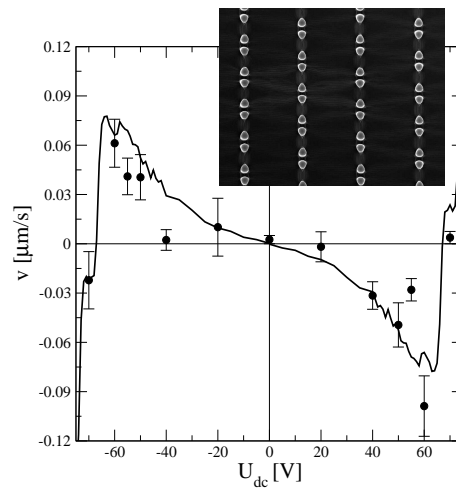


Figure 4.8: Experimental ANM velocity (dots with error bars) for different U_{dc} in design-4 ($U_0 = 80 \text{ V}$, $2\tau_d = 60 \text{ s}$). The velocity is increased by about one order of magnitude compared with Fig. 4.2, although larger particles ($2.9 \mu\text{m}$ compared to $1.9 \mu\text{m}$) are used. The black line shows the results obtained from numerical simulations. The fluctuations are due to the limited simulation time. The inset shows a SEM image of the experimentally used design-4.

Aiming at a separation utilizing ANM, both directions should be accelerated, i.e. the ANM direction as well as the 'normal' direction. This is experimentally validated (see Fig. 4.9) with the same particles ($2.9 \mu\text{m}$) as before, and a velocity enhancement is observed by one order of magnitude in the normal direction. For a detailed analysis of the migration modi, see Fig. 4.5.

4.1.4 Summary

In summary, absolute negative mobility could be demonstrated for non-interacting μm sized particles for the first time. The numerical simulation showed quantitative agreement, and allowed the prediction of parameters suitable for the fractionation of particles.

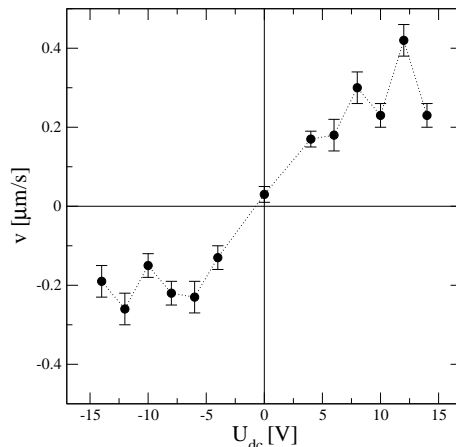


Figure 4.9: Experimental velocity (dots with error bars) for different U_{dc} in design-4 ($U_0 = 20$ V, $2\tau_d = 20$ s). Migration in the normal direction is observed and the velocity is one order of magnitude faster than obtained in Fig. 4.4. The dashed line is a guide to the eye.

Hence, the phenomenon could be used to separate differently sized particles by steering them into opposite directions. Moreover, ANM could be accelerated by one order of magnitude by optimizing post dimensions and shape. However, no simple scaling law for the acceleration of ANM can be given, but this complexity represents the flexibility of ANM to switch sign of the average migration velocity by simple adaptations of the driving parameters (see Figs. 4.8 and 4.9) and to guide different particles into opposite directions (see Sec. 4.1.2).

4.2 Electroless Dielectrophoretic Ratchet

The idea of extracting work out of unbiased random fluctuations, although all acting forces and temperature gradients average out to zero, is tempting. A self-winding wrist-watch is a macroscopical realization of the idea. Microscopically, however the situation is more subtle as the following example shows. In a box of gas at a certain temperature, there is an axle with vanes in it. Onto the other end of the axle, a ratchet and pawl is hooked onto the axle (see Fig. 4.10) [141]. Because of the bombardment of the gas molecules on the vane, the vane jiggles. Prima facie, it seems possible to extract work out of this system, as the pawl only allows the motion in one direction. However, the pawl itself is lifted randomly by Brownian motion, and consequently, the net motion is zero despite the broken symmetry. This is the reason why this device does not work in perpetual motion, and the fundamental law prohibiting this is the second law of thermodynamics ([142] and Ref. therein). However, the law only applies to systems at

thermal equilibrium, and the question arises what happens far from thermal equilibrium.

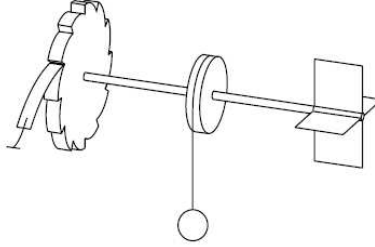


Figure 4.10: Ratchet and pawl [111, 141]. An axel connects the ratchet with the paddle. The system is placed in a box of gas and random collisions of the surrounding gas cause a jiggeling motion of the paddle, which is supposed to be rectified by the ratchet and pawl.

Several devices operating far from thermal equilibrium have demonstrated a net motion of particles although all forces average out to zero [32–36, 73]. Typically, the conditions far from thermal equilibrium are created by periodic driving. However, as already demonstrated in the section before, the highly nonlinear response of a system to a perturbation opens novel perspectives for separation and bioanalysis, as also mentioned in [36]. This nonlinear response is studied here in a highly parallelized dielectrophoretic ratchet. Simultaneously, the response of three differently sized particle species to a static perturbation is observed and discussed in the following.

The experimental setup is shown in Fig. 4.11. A time dependent voltage $U(t)$ is applied to the linear channel. An array of traingular posts is arranged in the channel such that every second row is shifted. Hence, a particle passing through a constriction directly heads towards another post.

In order to construct this dielectrophoretic ratchet with periodic back and forth motion, three components are necessary, all realized by the time-dependent voltage $U(t) = U_{ac}^{\text{fast}} \sin \omega_{\text{fast}} + U_{ac}^{\text{slow}}(\omega_{\text{slow}}) + U_{dc}$. A 'high' frequency ac voltage (sinusoidal) U_{ac}^{fast} of $\omega_{\text{fast}} = 60$ Hz induces a strong inhomogeneous electric field \vec{E} . In Sec. 2.2.4, the dielectrophoretic force of a spherical dielectric particle was given by

$$\vec{F}_{DEP} = 2\pi\epsilon_0\epsilon_m R^3 \text{Re}[K] \nabla \vec{E}^2, \quad (4.2)$$

where R is the radius and K the Clausius-Mossotti factor. The sign of K determines the direction whether a particle is attracted towards regions of large electric fields (positive dielectrophoresis, $K > 0$), or repelled by those regions and attracted towards regions of weak electric fields (negative dielectrophoresis, $K < 0$). The polystyrene particles in the given buffer demonstrate negative dielectrophoresis, i.e. the particles are attracted by regions of weak electric fields, in the following called traps (see Fig. 4.11(c)).

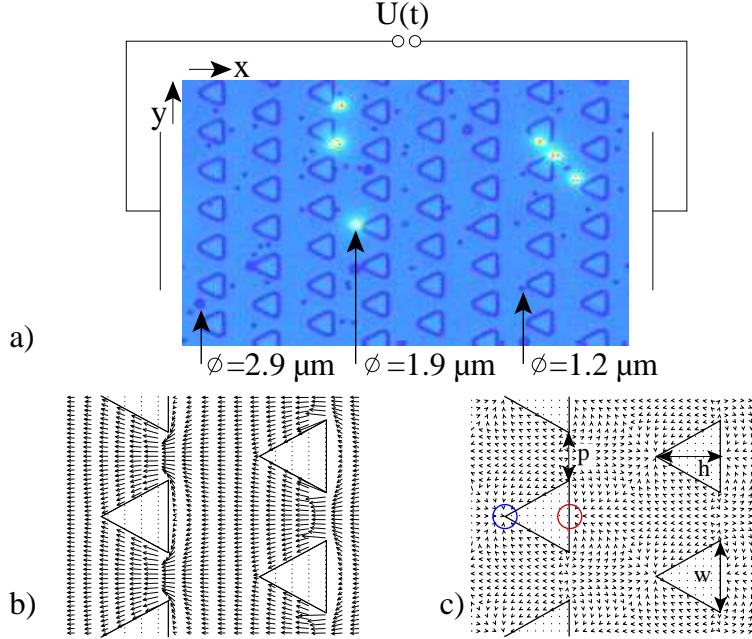


Figure 4.11: a) Schematic setup of the dielectrophoretic ratchet. Simultaneously, three different particle species are suspended in the channel, microstructured with triangular posts. A voltage $U(t)$ is applied along the x axis. The electrophoretic mobilities of the particles without a dielectrophoretic field is given in Tab. 4.3). b) Computed electric field lines in the microstructured post array, for example caused by U_{ac}^{slow} for one direction of the driving period or U_{dc} . The length of the arrows indicate the strength of the field. Post dimensions $h=7.8 \mu\text{m}$, $w=7.9 \mu\text{m}$, $p=5.5 \mu\text{m}$ and a period of $19 \mu\text{m}$ in x direction; overall width and length of the linear channel $100 \mu\text{m}$ and 8mm respectively. c) Calculated dielectrophoretic force field ($\nabla \vec{E}^2$) created by U_{ac}^{fast} . The arrows indicate the direction of the force. The red and blue circles indicate the regions of negative dielectrophoretic trapping.

The frequency of U_{ac}^{fast} is so high that the particles cannot follow the electric field electrophoretically. Hence, the potential created by U_{ac}^{fast} is interpreted as *quasi-static*. A 'slow' ac voltage $U_{ac}^{slow} = 12 \text{V}$ (square wave) with $\omega_{slow} = 0.25 \text{Hz}$ drives the particles periodically back and forth, i.e. creating conditions far from thermal equilibrium (see Fig. 4.11(b)). Finally, a dc voltage U_{dc} induces a static perturbation of the system (see also Fig. 4.11(b)). Thus, the electrical driving is comparable to the ANM experiments, except for the additional U_{ac}^{fast} . Moreover, again the observable of interest is the current of the particles along the x axis (see Eq. 2.21).

The response of three different particle species to different static perturbations is shown in Fig. 4.12.

The following responses are observed. The smallest particles ($1.2 \mu\text{m}$) demonstrate no net velocity in x direction at $U_{dc} = 0 \text{V}$ (see Sec. 2.4 for the definition of the velocity) because they are not dielectrophoretically trapped due to their small volume

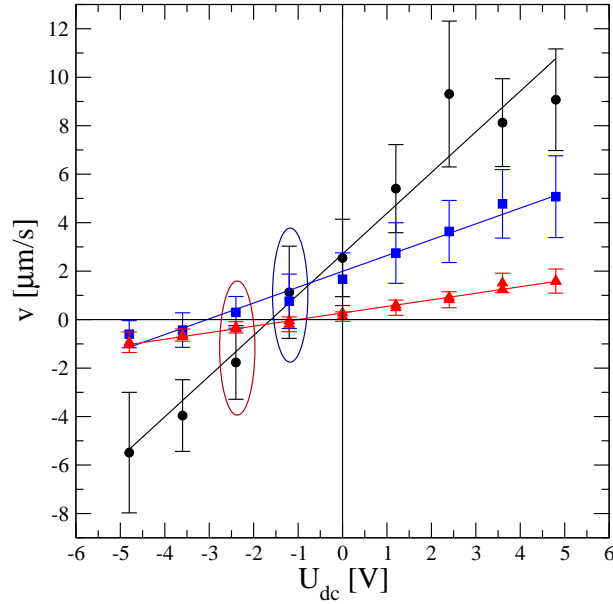


Figure 4.12: Response curve of three different particle species (1.2 μm (red triangles), 1.9 μm black dots), 2.9 μm (blue squares); the linear fits are guides to the eye). The smallest particles show no ratchet response, whereas the larger two particles do. The dielectrophoretic traps are created with a sinusoidal voltage of amplitude $U_{ac}^{\text{fast}} = 150$ V and frequency $\omega_{\text{fast}} = 60$ Hz, the back and forth driving by a square-wave voltage of amplitude $U_{ac}^{\text{slow}} = 12$ V and a frequency of $\omega_{\text{slow}} = 0.25$ Hz. The migration direction of the three particles can be selected by choosing the static perturbation U_{dc} . The blue and red ellipse indicate at which voltages the direction of migration of the particles change (blue ellipse: 1.9 and 2.9 μm particles to the right and 1.2 μm to the left; red ellipse: 1.9 μm particle to the right and 1.2 and 2.9 μm particles to the left).

($F_{DEP} \sim R^3$). Moreover, the particles migrate less than one spatial period due to their small electrophoretic mobility (see Tab. 4.3) before the polarity of the square wave voltage U_{ac}^{slow} changes, making a ratchet effect impossible (see Fig. 4.13(a)).

diameter [μm]	v_0 [$\mu\text{m}/\text{Vs}$]
1.2	0.46 ± 0.09
1.9	1.91 ± 0.18
2.9	1.73 ± 0.16

Table 4.3: Electrophoretic velocity of 1.2, 1.9 and 2.9 μm diameter particles.

The two larger particle species (1.9 μm and 2.9 μm) demonstrate a net current at $U_{dc} = 0$ V, i.e. although on average no force is applied, the particles demonstrate a ratchet effect and perform directed transport. They are large enough to be dielectrophoretically trapped and can travel more than one spatial period in one direction of

the 'slow' ac driving (see Fig. 4.13(b) and (c)).

Phenomenologically, the effect can be understood as follows (see Fig. 4.11). As the posts are nonconducting, the electric field lines avoid the posts and the result are two regions of weak electric fields, i.e. two energetic traps for particles exhibiting negative dielectrophoresis (see Sec. 2.2.4). In Fig. 4.11(c), the blue and red circles indicate the dielectrophoretic traps. The particles are preferably trapped at the flat side of the posts (red circle) because the electric field at the tip (blue circle) is stronger and the particle transport faster compared to the region marked with the red circle. Thus, thermal fluctuations are sufficient to move the particle away from the tip and to allow a subsequent transport by the electric field away from the trap. At the flat side (red circle), the transport by the electric field is much weaker, considerably increasing the trapping probability. Consequently, particles exhibiting negative dielectrophoresis are more easily trapped when migrating in the negative x direction, i.e. the average traveling distance is smaller. Vice versa, the particles can migrate further when the electric field points towards the positive x direction (see trajectories in Fig. 4.13).

The further interpretation of the data is difficult, as the particles possess different electrophoretic mobilities (see Tab. 4.3), such that the obtained response curves in Fig. 4.12 show the superposition of the different mobilities and polarizabilities. But interestingly, there are first indications that the order of migration of the particles can be controlled with a single parameter, the static perturbation U_{dc} . At $U_{dc} = -1.2$ V, the 1.9 and 2.9 μm particles migrate with a positive velocity, whereas the 1.2 μm particles migrate with a negative velocity. At $U_{dc} = -2.4$ V, only the 2.9 μm particles migrate with a positive velocity, whereas the 1.2 and 1.9 μm particles show a negative velocity. As mentioned above, these are first indications, especially concerning the error bars. For higher U_{dc} all particles have a positive velocity, and for lower U_{dc} all have a negative velocity.

In the literature, different realizations of ratchets have been demonstrated. In massively parallel asymmetric silicon pores, Matthias et al. achieved velocities of 1 $\mu\text{m}/\text{s}$ with colloidal particles [33]. Bader et al. demonstrated the ability of transporting DNA with a dielectrophoretic ratchet and demonstrated velocities of 2.5 $\mu\text{m}/\text{s}$ [36]. Gorre-Talini et al. constructed a dielectrophoretic ratchet and achieved particle velocities of 100 $\mu\text{m}/\text{s}$ [143].

The device presented here achieves velocities similar to most other devices. More importantly, however, first evidence could be presented that the order of migration of three differently sized particle species can be controlled by a single experimental parameter, opening new perspectives for particle separation.

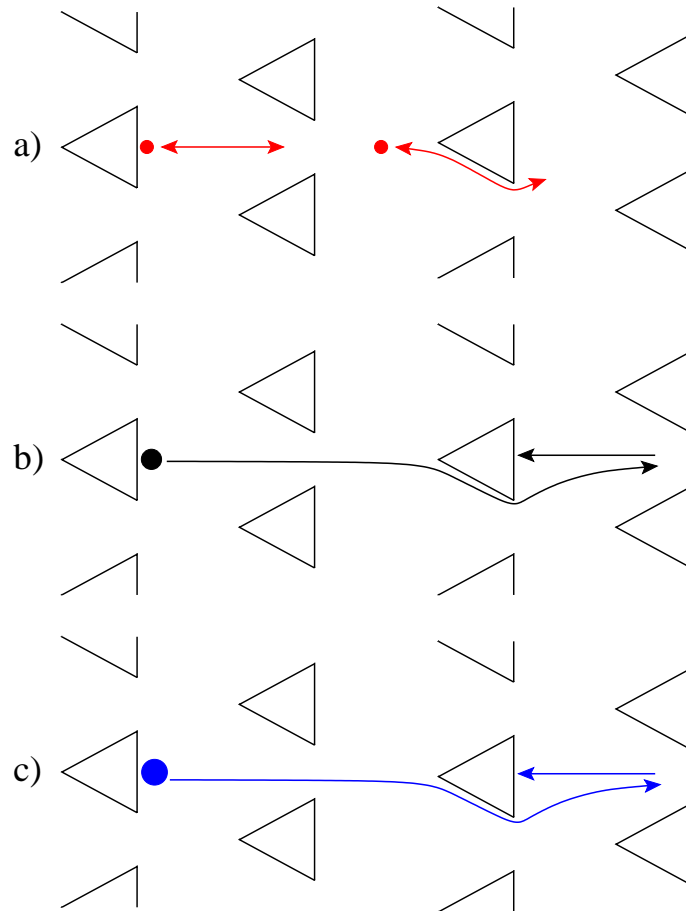


Figure 4.13: a) Two typical trajectories of a $1.2 \mu\text{m}$ particle during the back-and-forth motion. Because of the small electrophoretic mobility, the particles migrate less than one spatial period. And due to the small volume, the particle is not dielectrophoretically trapped. b) & c) Typical trajectories of the $1.9 \mu\text{m}$ and $2.9 \mu\text{m}$ particles are shown. The particles are dielectrophoretically trapped in one direction of the 'slow' driving.

In the future, the ratchet should be tested with differently sized but equally fast particles. Moreover, quantitative simulations should be performed in order to find optimized driving parameters that demonstrate unambiguous response curves validating the evidence presented here.

4.3 Dielectrophoretic Manipulation of DNA

In 1991, the idea was proposed to separate polymers based on the combination of dielectrophoretic trapping and electrophoretic forces [115]. For dielectrophoretic trapping, one needs a polarizable object, in this case DNA, and an inhomogeneous electric field,

which is usually generated by microelectrodes [144]. Alternatively, an inhomogeneous electric field can also be obtained without microelectrodes (i.e. electrodeless) by the use of nonconducting posts in microfluidic channels [76,81], thereby reducing the complexity of the fabrication process and, more importantly, providing field gradients over the entire depth of the microchannel (see Sec. 2.2.4).

The dielectrophoretic manipulation of DNA has been increasingly studied over the last years, including the investigation of DNA in microfluidic devices [78, 81, 90, 145]. Especially Chou et al. [81] paved the way for the present study by thoroughly discussing the electrodeless dielectrophoretic trapping of single and double stranded DNA, demonstrating size-dependent frequency response for DNA fragments from 368 bp to 39.9 kbp below 1 kHz. Similarly, frequency dependent dielectrophoretic trapping using microelectrodes was reported in [90] for a frequency range below 1 kHz. It could be shown that DNA polarizability strongly depends on the frequency range and buffer conditions (e.g. ionic strength) and is quantitatively accessible usually in bulk measurements by birefringence [146–148], conductivity dispersion [149] or time domain reflectometry [91]. However, the mechanism involved in DNA polarization as well as the dependence of the dielectrophoretic response on the DNA length remains unclear [85,91] (see Sec. 2.2.4).

This section is organized as follows: first the setup and the ability to trap DNA is demonstrated (see Sec. 4.3.1). Having proven these prerequisites, the feasibility of separating DNA via electrodeless dielectrophoresis is demonstrated (see Sec. 4.3.2). Based on a theoretical analysis of the size-dependent DNA migration (see Sec. 4.3.3), a new method is developed for the quantitative deduction of the DNA polarizability (see Sec. 4.3.4). The results are discussed in terms of a power law length dependence and possible relations to the radius of gyration. This new method is then used to fathom some basic dependencies of the polarizability, such as salt and dye concentration and frequency (see Secs. 4.3.5, 4.3.6 and 4.3.7).

4.3.1 DNA Trapping

A scheme of the microfluidic setup is shown in Fig. 4.14. The DNA is injected via the cross injector into the microstructured separation channel. First, it is verified that the device is suitable for dielectrophoretic DNA manipulation. In Fig. 4.15(a), the typical experimental situation is shown for T2 DNA (164 kbp) in the microstructure. The DNA is subjected to a time-dependent voltage $U(t) = U_{ac} \sin \omega t$ with frequency $\omega = 60$ Hz and amplitude $U_{ac} = 300$ V. The DNA is permanently trapped within the gaps close to the post walls, i.e. at locations of high electric fields, very similar to the positive

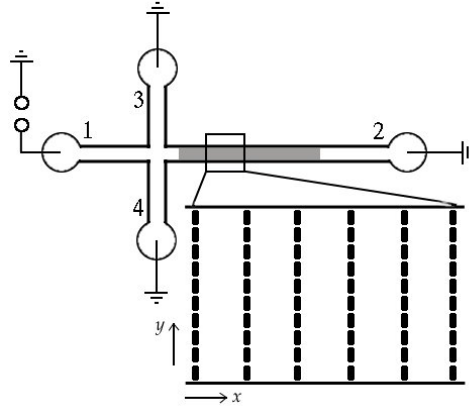


Figure 4.14: Scheme of the microfluidic setup (not to scale). The device consists of a cross injector, formed by the channels 1,3 and 4 (each 2 mm long). Channel 2 (5 mm long) contains the microstructure, indicated by the gray region, in which dielectrophoretic trapping and separation is performed. The depth of all channels is $6 \mu\text{m}$; the channel width is $100 \mu\text{m}$ for channels 1 and 2 and $95 \mu\text{m}$ for channels 3 and 4. The enlargement shows that the microstructure consists of periodically arranged rows of rectangular posts (180 rows) with a period of $L=21.1 \mu\text{m}$ in x direction and a distance between the posts of $2.3 \mu\text{m}$ in y direction. The base area of each post is $2.2 \times 7.4 \mu\text{m}^2$. After the DNA is injected via a pinched injection scheme, the driving voltages $U(t)$ are applied in reservoir 1, whereas all other reservoirs are grounded.

dielectrophoretic trapping of DNA reported by Chou et al. [81]. Note, that this is in contrast to the dielectrophoretic traps in Sec. 4.2, which consist of regions with low electric fields due to the negative dielectrophoretic response of the polystyrene particles.

On the first glance, no DNA motion due to the ac voltage U_{ac} can be observed (see Fig. 4.15(a)). As the frame rate of the camera is not sufficient for a direct observation of DNA motion in a trap, a stroboscopic time series is recorded with 59.4 ± 0.05 fps (see Fig. 4.16). The DNA motion is observed with a repetition after (1.52 ± 0.03) s, which is within the time period of a beat of 1.43 ± 0.08 s caused by the different frequencies of the electric field ($\omega = 60$ Hz) and the frame rate of the camera (59.4 ± 0.05 fps) (see Methods Sec. 3.6.2).

The trapping can be understood as follows. The applied time-dependent voltage $U(t)$ leads to an inhomogeneous electric field $\vec{E} \sin \omega t$ in the structured region, with a field strength \vec{E} proportional to U_{ac} and with the spatial periodicity of the structure. For polarizable molecules with polarizability $\alpha = \alpha(\omega)$, this field creates a dielectrophoretic potential landscape given by (see Sec. 2.2.4)

$$W = -(1/2)\alpha\vec{E}^2, \quad (4.3)$$

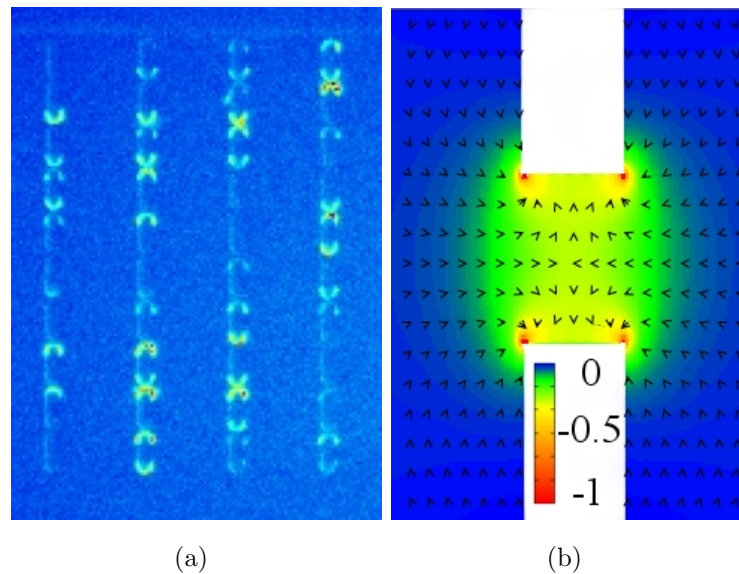


Figure 4.15: (a) Fluorescence micrograph of fluorescently stained T2-DNA that is trapped by dielectrophoresis in the high field regions in the gaps between neighboring posts ($U_{ac} = 300$ V, $\omega = 60$ Hz). (b) Dielectrophoretic potential $W = -(1/2)\alpha E^2$ in a gap between two posts (white rectangles) in the case of positive dielectrophoresis ($\alpha > 0$). The electric field is numerically calculated (see Sec. 2.5). The color code indicates the magnitude of the potential energy in arbitrary units. The arrows indicate the direction of the resulting dielectrophoretic force field. Potential minima occur near the edges of the posts. Thus, the potential reproduces the experimentally observed trapping.

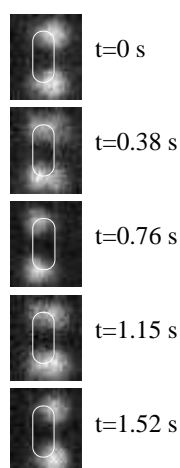


Figure 4.16: Stroboscopic time series of the DNA motion in a trap. The λ -DNA is trapped by an ac voltage $U_{ac} = 240$ V of $\omega = 60$ Hz. The time series is recorded with a frame rate of (59.4 ± 0.05) fps, thus a full period of motion should take (1.43 ± 0.08) s. At $t = 0$, the DNA is at the right side of the post, at $t = 0.76$ s at the left side and after $t = 1.52 \pm 0.03$ s again on the right side. Thus, the DNA follows the ac field in the trap with $\omega = 60$ Hz.

where the factor $(1/2)$ stems from the time average of the $\sin^2(\omega t)$ function. In this description, adsorption effects are neglected so that the polarizability α is real-valued and a quasi-static potential is assumed, i.e. the back and forth motion due to $U(t)$ is neglected. For $\alpha > 0$, the molecule is driven towards the regions of the strongest field amplitudes, which represent the minima of W (positive dielectrophoresis), while for $\alpha < 0$, regions with smallest field amplitudes form the potential minima (negative dielectrophoresis). As illustrated in Fig. 4.15(b), the potential with $\alpha > 0$ has deep minima within the gaps in the regions close to the post walls where the DNA is observed to be trapped (Fig. 4.15(a)), indicating that the trapping is due to positive dielectrophoresis.

The agreement of the experimentally observed trapping and the calculated potential (see Fig. 4.15) indicates that the quasi-static dielectrophoretic potential constitutes an appropriate model for the impact of the ac voltages $U(t)$ on the DNA, although it is neglecting the DNA motion in the trap.

4.3.2 Dielectrophoretic DNA Separation

Ajdari and Prost predicted size separation of DNA with length dependent polarizabilities due to different average migration velocities in a simplified one-dimensional model, when an appropriate static force is applied in addition to the dielectrophoretic traps [115]. Similarly, Chou et al. [81] suggested to selectively trap one sort of DNA while removing another one. These ideas are reasonable because the depth of the potential depends on the polarizability and the polarizability of short (< 5 kbp) DNA fragments is known to increase with their lengths [85].

In order to impose an additional constant force on the DNA in the microstructure, a static voltage component U_{dc} is superimposed onto the oscillating signal $U(t)$. For the separation of two different DNA lengths, an optimal choice of U_{dc} and U_{ac} should permanently trap one DNA species whereas the other one can migrate along the channel. This requires precise knowledge of polarizabilities and electrophoretic mobilities of the DNA molecules under the given experimental conditions. Because a priori such information is usually inaccessible, it is difficult to find the right parameters. The situation becomes even more complicated if more than two species should be separated.

Therefore, the following separation protocol was developed. The DNA is injected with a constant U_{dc} and during migration the different U_{ac} values are probed by increasing U_{ac} from U_{start} to U_{end} in discrete steps of size U_{inc} and duration τ_{inc} . When U_{end} is reached, U_{ac} is set to a value U_{final} and U_{dc} is switched off to create steady-state trapping conditions. Then the channel is scanned for fluorescence signal and an electropherogram

is recorded.

Such separation experiments are performed with three different samples: (a) a mixture of linear λ - and T2-DNA at concentrations 41 and 6.1 pM respectively; (b) a supercoiled ccc plasmid DNA sample, containing a 7 kbp plasmid and its 14 kbp dimer in a concentration ratio 9:1; (c) a sample containing a 12 kbp ccc monomer, its 12 kbp linearized monomer and the 24 kbp ccc dimer with approximate concentrations of 20 pM for both ccc forms together and 17 pM of the linear form. The observed steady-state electropherograms are shown in Fig. 4.17.

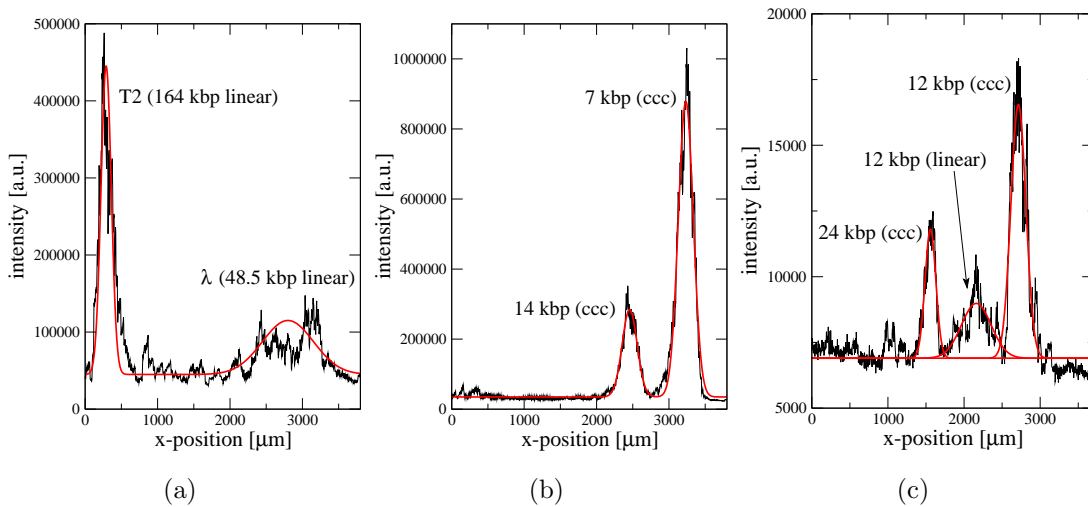


Figure 4.17: Steady-state electropherograms after application of the separation protocol for (a) a λ - and T2-DNA sample; (b) a 7 kbp monomer and its 14 kbp ccc dimer plasmid; (c) (PJP2) 12 kbp ccc monomer, 12 kbp linearized form and 24 kbp ccc dimer. The parameters of the separation protocols are summarized in Tab. 4.4. For all samples, the different DNA species have been trapped at different locations in the separation channel and could thus be separated with base line resolution within less than 240 s. The peaks are fitted by Gaussian curves.

The different DNA fragments in the samples are attributed to the peaks by comparison to control experiments with samples containing only a single DNA species and by spiking experiments. The identification of different fragments due to their fluorescent brightness is complicated by the fact that different conformations can gather different amounts of dye, as formerly noticed for ethidium bromide [150].

The results demonstrate that the technique can be used for various kinds of samples. The separation of long linear fragments is possible (Fig. 4.17(a)), as well as the separation of differently long supercoiled fragments (Fig. 4.17(b)). Most interestingly, even samples of the same length could be separated according to their conformation within less than 240 s (Fig. 4.17(c)).

In order to quantify the efficiency of the dielectrophoretic separation, the resolution Res is calculated as usual for separations according to [151]

$$Res = (x_2 - x_1)/[2(\sigma_1 + \sigma_2)]. \quad (4.4)$$

Here, x_1 and x_2 are the positions of the centers of Gaussian curves fitted to the measured peaks and σ_1 and σ_2 are their width. Every separation experiment resulted in base line resolution, with the calculated resolutions summarized in Tab. 4.4.

sample	U_{dc} [V]	U_{start} [V]	U_{inc} [V]	τ_{inc} [s]	U_{end} [V]	ω [Hz]	t^a [s]	Res^b
λ -T2	12	150	0.6	3	189	60	200	2.95
7-14 kbp ccc	12	198	6	30	240	60	240	1.93
PJP2	12	270	6	13	360	60	210	0.94 ^c ;1.13 ^d

Table 4.4: Tabular overview over the applied voltage ramps during DNA separation and the resulting resolution (see Eq. 4.4). ^a total separation time; ^b resolution (Res); ^c resolution of the ccc monomer (12kbp) separated from the linear monomer (12 kbp); ^d resolution of the ccc monomer (12 kbp) from the ccc dimer (24 kbp).

Shortly after the first presentation of these results, Petersen et al. [152] also presented the migration and separation of linear DNA in a dielectrophoretic microelectrode array with a separation time of up to 100 min. This time is comparable to the time effort needed to analyze DNA with agarose gel electrophoresis or capillary gel electrophoresis (see Fig. 4.18) [132]. The quality control experiments with both techniques, for the samples used in this study, lasted about 60 min each.

Compared to other artificial gel techniques, the method presented here achieves very competitive separation times of less than 240 s. For example, Han et al. needed about 30 min to separate large DNA linear fragments in an array of entropic traps [20]. Doyle et al. demonstrated the separation of linear DNA also within about 30 min an array of magnetic beads [15]. Huang et al. used a *DNA prism* for linear DNA separation and achieved separation times of 15 s [11]. All mentioned artificial gel techniques only demonstrated the separation of DNA fragments of the same conformation.

Only very few studies focus on circular DNA and the separation of different conformations with chip based approaches, although the separation of different DNA configurations with slab and capillary gel electrophoresis are established techniques for this application. The only study, known to the author, was published by Li et al. and they demonstrate the separation of different DNA conformations on a flat and on a nanostructured silicon surface with separation times of about 60 min [22]. Furthermore,

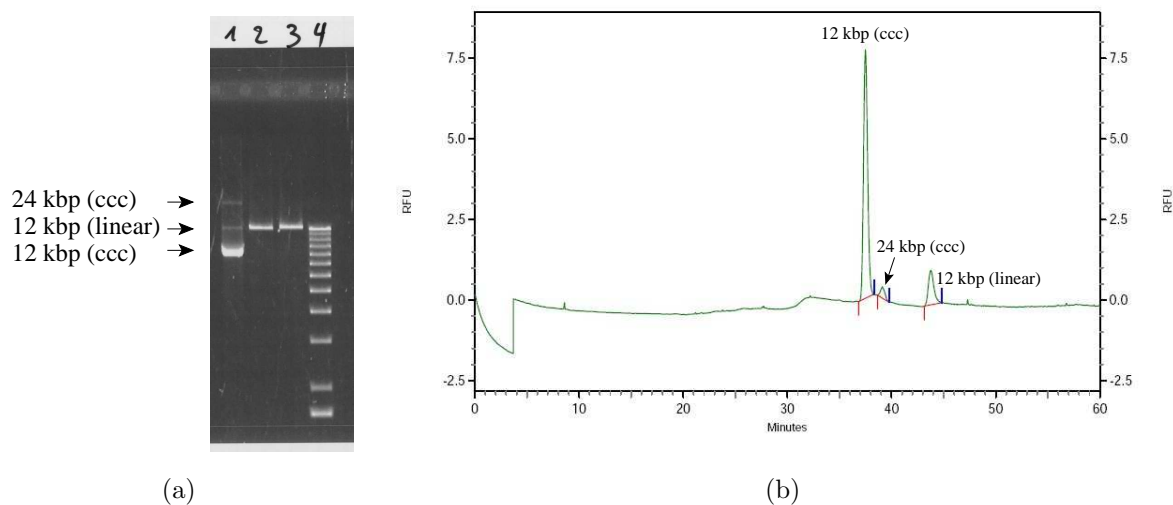


Figure 4.18: (a) Fluorescent image on an agarose gel. (1) Original PJP2 sample (from top to bottom: 24 kbp ccc, 12 kbp linear, 12 kbp ccc), (2) PJP2 linearized with KpnI, (3) PJP2 linearized with EcoI, (4) marker (original data, separation time 1 h, see also Sec. 3.4). (b) Electropherogram of the PJP2 sample (original data) obtained by capillary gel electrophoresis [131], parameters given in [132].

there is no general agreement among DNA separation techniques concerning the order of migration of linear, supercoiled and relaxed circular DNA. This can also be observed in the comparison of the agarose gel with the capillary gel electrophoresis (see Fig. 4.18). The order of migration depends on type and concentration of the intercalating dye, the surface coating, and the operating conditions [22, 153].

Finally, from the follow up of the peaks in Fig. 4.17, one can conclude for the given size range that longer linear DNA fragments are better polarizable than shorter linear fragments. Furthermore longer supercoiled fragments are better polarizable than shorter supercoiled fragments. Besides the length separation, the method presented here is also sensitive to DNA conformation, i.e. the linear monomer is better polarizable than its supercoiled monomer and the supercoiled dimer is better polarizable than the linear monomer. The quantification of the polarizability is discussed in detail in the following section.

In conclusion, the combination of electrodeless dielectrophoresis and electrophoresis allows the separation of DNA according to length and conformation with a special protocol. All samples could be separated with baseline resolution and within less than 240 s.

4.3.3 Quantitative Description of DNA Migration

In order to understand the separation mechanism in more detail, an analysis of the DNA migration is indispensable. Therefore, not a voltage ramp is considered, but just constant amplitudes U_{ac} of the ac voltage $U(t)$. The amplitude creates a dielectrophoretic potential for the DNA molecules with traps in between the constriction made up of two posts. Only by ambient thermal noise, the DNA molecule can escape from such a trap. For large U_{ac} , the potential barrier that has to be surmounted is much larger than the thermal energy $k_B T$, so that an escape process can be considered as a rare event. When the dc voltage U_{dc} is applied in addition to $U(t)$, the potential landscape is tilted due to the induced electrokinetic force. As long as the dielectrophoretic force is larger than the electrokinetic force, the DNA is trapped deterministically and can still only escape by thermal noise. If a molecule escapes from a trap, it is driven along the channel towards the next trap. For appropriate U_{ac} values, the barrier heights of the tilted dielectrophoretic potential are comparable to $k_B T$. Thus, the escape process leads to an average migration velocity in the range of μm per second.

Considering Eq. 4.3, the depth of the dielectrophoretic potential depends on the polarizability of the molecule. Hence, differently polarizable DNA molecules have different migration velocities.

In good approximation, confirmed by observing the DNA molecule trajectories, the migration of the DNA can be described as the motion in an one-dimensional tilted quasi-static periodic potential with deep and narrow potential minima that represent the dielectrophoretic traps (see Sec. 4.3.1). From an estimation of the curvatures Ω^2 (see Eq. 2.25) of the dielectrophoretic potential in x direction, i.e. along the direction of migration, it can be concluded that the *deformation energy* $\Omega^2 l_p^2$ at the length scale of the persistence length $l_p \approx 50$ nm of the DNA is much smaller than the thermal energy ($\Omega^2 l_p^2 \ll k_B T$), except for very small regions at the corners of the posts. Thus, the DNA molecules remain through out the migration process in a globular configuration. In this case, the trapping time of a DNA molecule, i.e. the time a molecule is trapped before thermally induced escape, is given by the inverse Kramers rate [117, 118] (see Sec. 2.6.1)

$$\tau \propto \exp\left(\frac{\Delta W - \Delta W_{dc}}{k_B T}\right), \quad (4.5)$$

where $\Delta W - \Delta W_{dc}$ denotes the dielectrophoretic potential barrier reduced by the energy drop due to the static voltage U_{dc} .

With the above given assumptions, the DNA migration can be described with the one-dimensional model of Ajdari and Prost [115]. According to this model, the average

migration velocity is given by

$$v = L/(\tau + t_0), \quad (4.6)$$

where L is the periodicity of the microstructure in x direction, t_0 the time needed from trap to trap with no dielectrophoretic potential ($U_{ac} = 0$), and τ the mean trapping time according to Eq. 4.5.

In order to quantify the dielectrophoretic potential ΔW , the quantitative knowledge of the potential drop within the microstructure is necessary and can be derived as follows. The fluid is assumed as an ideal conductor, the PDMS as an ideal insulator. Thus, the fluidic chip can be interpreted as an electric circuit [154]. Every segment of the channels with constant cross section is represented by a resistor whose resistance is proportional to the segment length and inversely proportional to the cross sectional area. The unknown electric resistivity is not necessary, as only ratios of resistances are needed. With Kirchhoff's law the potential drop at a single row of posts and in between two rows can be calculated. Recalling the dimensions of the device, a potential drop at a single row of posts is $4.9 \times 10^{-4}U$ with U the applied voltage. By dividing the potential drop by the size of the gaps in field direction ($2.2 \mu\text{m}$), the average electric field is $E_{gap} \approx 220U \text{ m}^{-1}$. For comparison, a simple estimate of the electric field by assuming that the voltage U is applied over the total channel length of channels 1 and 2 would yield a factor 140 instead of 220.

Thus, the potential barrier ΔW can be written, with the now accessible electric fields, as $\Delta W = (1/2)\alpha(E_{gap}^2 - E_{mid}^2) = (1/2)\alpha E_{gap}^2(1 - E_{mid}^2/E_{gap}^2)$. The field strength E_{gap} is an approximation of the average field in a trap. E_{mid} is the electric field in the middle between two rows and can be considered as constant over the channel cross section in good approximation. With the fulfilled condition $\nabla \vec{E} = 0$, the field strengths are related by $E_{mid}/E_{gap} = Y_{gap}/Y_{mid}$ with Y_{gap} and Y_{mid} the widths of the fluid accessible part of channel 2. For the here treated microstructure, one finds $Y_{gap} = 23 \mu\text{m}$ and $Y_{mid} = 100 \mu\text{m}$, so that $E_{mid}/E_{gap} = 0.23$. As stated before, E_{gap} is proportional to U_{ac} with a proportionality factor obtained from the equivalent circuit diagram. Thus, the dielectrophoretic potential barrier can be calculated in good approximation as

$$\Delta W = 22900\alpha U_{ac}^2 \text{ m}^{-2}. \quad (4.7)$$

4.3.4 Polarizability of Linear and Supercoiled DNA

The gained insight into DNA migration in such a dielectrophoretic potential landscape offers the possibility to determine the polarizability quantitatively. If the experimentally

observed escapes are rare events, i.e. trapping times in the order of 100 ms, the rate description Eq. 4.5 is valid. In this case, the mean trapping time τ depends linearly on U_{ac}^2 (see Eqs. 4.5 and 4.7), with logarithmic corrections of the form $\ln U_{ac}^2$ that are due to the prefactors of Eq. 4.5, respectively Eq. 2.25. Evaluating the linear contribution in the U_{ac}^2 dependence, the polarizability α can be calculated according to Eq. 4.7. Thus, just τ has to be observed for different U_{ac} in order to determine the polarizability α .

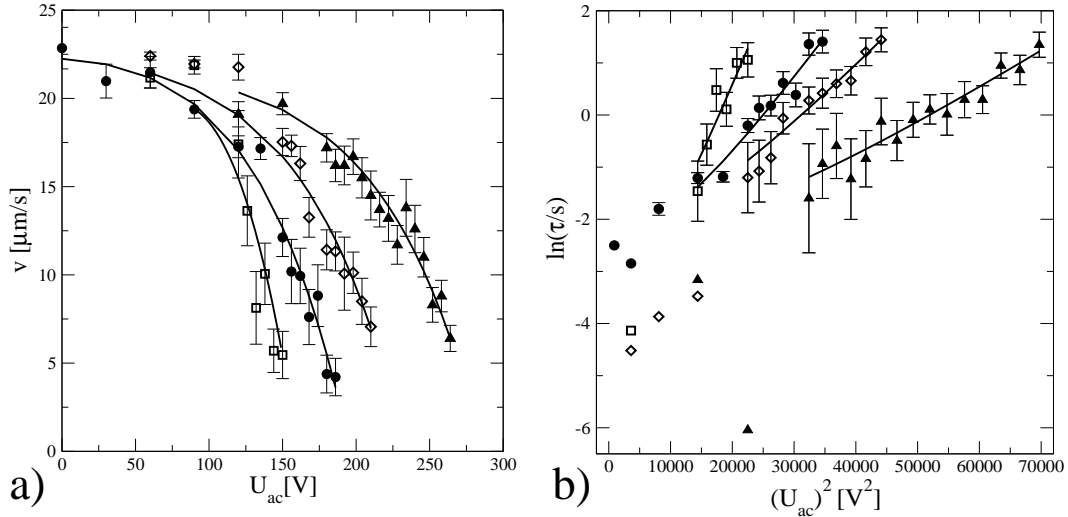


Figure 4.19: (a) Average velocities v versus the applied voltage U_{ac} for 6 kbp (triangle), 12 kbp (diamond), 48.5 kbp (bullet) and 164 kbp (box) linear DNA at $\omega = 60$ Hz and $U_{dc} = 12$ V. About 30 molecules are recorded per U_{ac} value and species and evaluated to determine the average velocity. The longer DNA fragments are retarded for smaller U_{ac} values than the smaller fragments. At the end points of each curve, the velocities become immeasurably small, as the molecules are permanently trapped within the observation time. The lines are guides to the eye. (b) Mean trapping time τ plotted versus the square of the U_{ac} voltage amplitude (symbols as in (a)). The in (a) determined velocities are used to calculate the trapping time τ according to Eq. 4.6 together with the determined free migration time $t_0 = (1.0 \pm 0.1)$ s. The solid lines are linear fits with logarithmic corrections where the rate description is valid.

In Fig. 4.19(a), the average migration velocity for different U_{ac} is shown. For small U_{ac} , all DNA species show very similar velocities, as expected for the length independent free electrophoresis of DNA [45]. For larger U_{ac} , the retarding effect of the dielectrophoretic trapping induces significantly different velocities for the different DNA species. As already expected from the separation experiments, longer fragments are trapped at lower values of U_{ac} than smaller fragments (see Sec. 4.3.1).

The average migration velocity is then used, to calculate the trapping time τ according to Eq. 4.6. Therefore, the free migration time t_0 , i.e. $U_{ac} = 0$, is determined between two successive rows of posts, with $t_0 = (1.0 \pm 0.1)$ s at $U_{dc} = 12$ V

for all DNA species conforming the length independent free migration. The mobility of $\mu_0 = (3.5 \pm 0.4) \times 10^{-8} \text{ m}^2/\text{Vs}$ agrees very well with the values in the literature [10] ranging from 3.0×10^{-8} to $4.5 \times 10^{-8} \text{ m}^2/\text{Vs}$.

Fig. 4.19(b) demonstrates the dependence of the mean trapping time τ on the applied amplitude of U_{ac} . The expected dominating dependence of $\ln \tau$ on U_{ac}^2 (see Eq. 4.7) is confirmed for large enough values of U_{ac} when the rate description becomes valid. The measured data is fitted linearly with the above mentioned logarithmic corrections and clearly different slopes for the different species become obvious. From those the polarizability is calculated according to Eq. 4.7. Additionally, the polarizability of supercoiled DNA fragments of length 7, 10, 15 and 21 kbp are measured and all results are summarized in Tab. 4.5.

linear DNA (kbp)	$\alpha (Fm^2)$	ccc DNA (kbp)	$\alpha (Fm^2)$
6	$(1.5 \pm 0.1) \times 10^{-29}$	7	$(0.5 \pm 0.1) \times 10^{-29}$
		10,3	$(1.7 \pm 0.2) \times 10^{-29}$
12	$(2.5 \pm 0.2) \times 10^{-29}$		
12,2	$(2.8 \pm 0.6) \times 10^{-29}$	12,2	$(2.3 \pm 0.7) \times 10^{-29}$
		15,5	$(2.8 \pm 0.1) \times 10^{-29}$
		21	$(2.9 \pm 0.2) \times 10^{-29}$
48,5	$(3.3 \pm 0.3) \times 10^{-29}$		
164	$(5.8 \pm 0.5) \times 10^{-29}$		

Table 4.5: Experimentally determined polarizabilities for different fragment lengths and conformations. For all fragments of the same conformation, an increase in polarizability with length is observed with exception of the 21 kbp ccc fragment. Additionally, the 12,2 kbp PJP2 plasmid is characterized in the linear conformation as well as in the supercoiled conformation, demonstrating that the polarizability not only depends on length but also on conformation. The order of migration observed in the separation is also confirmed (see Sec. 4.3.2).

Before the obtained polarizabilities are compared to published data, the assumptions and approximations are summarized, which are necessary to extract the polarizability from the mean trapping time. The effect of the time-dependent ac voltage $U(t)$ on the molecule is completely described by the dielectrophoretic potential Eq. 4.3, i.e. the back and forth motion of the DNA due to the ac voltage is neglected. During the migration, the DNA molecules keep their globular configuration, in particular during the escape process from the trap. Calculating the curvatures Ω^2 of the dielectrophoretic potential, the deformation energy $\Omega^2 l_p^2$ at the length of the persistence length is much smaller than

the thermal energy. Thus, any deformation is compensated by thermal fluctuations. Moreover, corrections to the Kramers formula Eq. 4.5 due to DNA deformations in the traps would result in deviations from the observed linear dependence of $\ln \tau$ on U_{ac}^2 . Moreover, it is assumed that the DNA escapes on a single one-dimensional path in the $x-y$ plane. This assumption is strongly supported by observations of the escape events. Especially transitions in the y direction, which would prolong the migration from trap to trap, are not included in the model and are observed experimentally only very rarely. Finally, the amplitude of the electric field is approximated by the average field amplitude in the traps as well as in the sections in between, as calculated in Sec. 4.3.3. The good agreement of the observed mobility, based on the calculated electric field, indicates that this method yields reliable approximations of the electric field amplitudes.

Discussion of the Polarizability of Linear DNA

The following discussion is restricted to linear DNA fragments, whereas the polarizability of the supercoiled fragments is discussed in the next section. The determined polarizabilities are comparable to values reported in the literature (see Tab. 4.6), confirming the validity of the assumptions just summarized. Nevertheless, a quantitative comparison seems questionable because of the different techniques, conditions and frequencies used to determine the polarizability. Moreover, for the method presented here, a fluorescent staining is necessary and its influence on the polarizability is discussed later (see Sec. 4.3.7). Interestingly, Tuukkanen et al. [155] recently published DNA polarizabilities determined from dielectrophoretic DNA trapping with an microelectrode array. They determined the minimum necessary voltage to trap the DNA and calculated from simulations the corresponding field strength. Then, they derived the polarizability by assuming that the minimum trapping energy is equal to the thermal energy $(3/2)k_B T$. They found polarizabilities that are 1 to 2 orders in magnitude smaller than the values determined here. The reasons are the different ways to quantify the potential barrier. Tuukkanen et al. assume the thermal energy as the potential barrier, which has to be overcome. The method presented here quantifies the potential barrier by determining the trapping times.

The quantitative determination of α also allows the calculation of the acting force in the trap, resulting in values from 3 to 12 fN for the different linear DNA fragments at $U_{ac} = 140$ V. Chou et al. [81] found comparable values ranging from 2 to 6 fN and thus confirm the values obtained.

For short DNA fragments, the length dependence of the polarizability is often de-

Ref.	DNA (kbp)	α (Fm^2)	method	buffer system
[146]	4.4	5.5×10^{-31}	TEB ^a	Tris 0.2 mM, pH 8
[147]	5	2.3×10^{-30}	TEB ^a	sodium phosphate 1 mM Na, pH 7.2
[149]	8	3.2×10^{-28}	CD ^{b, e}	1 mM NaCl
	16	3×10^{-27}		
[91]	12 (plasmid)	7.88×10^{-30}	TDR ^{c, d}	dd H_2O
[148]	40 (T7 DNA)	1.3×10^{-28}	TEB ^b	sodium phosphate 0.5 mM Na, pH 6.9
[155]	8	2×10^{-30}	DEP trap	3 mM Hepes, 2mM NaOH, pH 6.9

Table 4.6: DNA Polarizabilities for various DNA lengths and buffer conditions as reported in the literature together with the used techniques. The list does not claim completeness and is restricted to DNA lengths comparable to the ones studied here. ^a transient electric birefringence (TEB); Frequency > 1 kHz. ^b Frequency < 1 kHz. ^c Frequency 137 kHz. ^d time domain reflectometry (TDR). ^e conductivity dispersion (CD).

scribed by a scaling law $\alpha \sim N^\gamma$, although different exponents are discussed in the literature. For example, Stellwagen [146] reported $\gamma = 2$ for DNA lengths below ~ 300 bp. Elias and Eden [147] found $\gamma = 3$ in the range up to ~ 120 bp lengths passing into linear relation ($\gamma = 1$) above ~ 300 bp up to 5 kbp. Furthermore, Porschke et al. [85] showed evidence for a cubic dependence for DNA below ~ 400 bp, whereas they reported a saturation of the polarizability for longer DNA molecules. Although the fragments studied here are much longer, the determined polarizabilities indicate an increase with length. The log-log plot of the polarizability versus the number of base pairs shown in Fig. 4.20(a) demonstrates an exponent of $\gamma = 0.4 \pm 0.1$ for the linear DNA fragments. Thus, there is no saturation observed, but the length dependence is much weaker, than for the short fragments discussed in the literature.

In this context, it is interesting to note that the deduced value of γ is close to the theoretical Flory exponent of $\nu = 0.5$ without excluded volume [45]. The Flory exponent describes the power law scaling of the radius of gyration with length ($R_g \sim N^\nu$) (see Sec. 2.1.1). This might suggest that the polarization is driven by a charge transport along the DNA strand and results in an effective polarization that scales with the end-to-end vector of the DNA molecules, as previously anticipated by Bowers and Prud'homme [156]. Because of the very limited data (four DNA lengths), a more detailed study is necessary, but some interesting findings concerning this scaling will be discussed.

In Fig. 4.20(b), the diffusion coefficients determined for the four DNA species are plotted versus the number of base pairs (for the method see Sec. 3.6.2 and for quanti-

DNA [kbp]	D [$\mu\text{m}^2/\text{s}$]	DNA [kbp]	D [$\mu\text{m}^2/\text{s}$]
linear		supercoiled	
6	1.71 ± 0.11	7	2.80 ± 0.15
12	1.36 ± 0.10	10.3	1.32 ± 0.05
48.5	0.68 ± 0.09	15.5	0.83 ± 0.03
164	0.39 ± 0.05	21	1.05 ± 0.06

Table 4.7: Diffusion coefficients for linear and supercoiled DNA fragments (the corrections due to the particle tracking deduced in Sec. 2.7 give a negligible contribution)

tative data see Tab. 4.7). The slope of the plot results in $\nu = 0.45 \pm 0.05$ indicating a scaling (within the experimental error) according to the scaling predicted for polymers without excluded volume (see Sec. 2.1.1) (the negative sign is omitted, which is due to plotting D instead of R_g as $D \sim 1/R_g$). In the literature, different scaling behaviors for DNA are reported. With light scattering methods, exponents from $\nu = 0.48$ to 0.53 were reported [157, 158], thus a scaling without excluded volume effects (see Sec. 2.1.1). Recently, Robertson et al. reported $\nu = 0.571 \pm 0.014$ determined with video tracking methods [48], and this scaling indicates a contribution of excluded volume effects [46] (see Sec. 2.1.1). The difference might be due to the different buffer and salt concentrations, different viscosities and the different techniques used (see Sec. 2.1.1).

Especially the salt concentration determines the electrostatic self-repulsion of charged DNA molecules. It is often assumed that the effective diameter of DNA is rather given by the Debye length λ_d than the actual helical diameter. Again, the persistence length l_p depends on the electrostatic repulsion [51] and thus on λ_d . Larger λ_d and l_p imply a much stronger excluded volume effect. Under the given experimental conditions, however, $\lambda_d = 3$ nm can be assumed [47, 48, 159], which implies only a marginal excluded volume effect [46].

Considering the polarizability and the diffusion determined for the four linear DNA fragments, Fig. 4.20(c) encourages the scaling of the polarizability with the end-to-end distance as proposed by Bowers et al. [156] because the polarizability scales nearly linearly with the radius, in fact $R_g \sim \alpha^{0.8 \pm 0.2}$.

Assuming that the polarizability scales with the end-to-end radius, i.e. there is a dipole induced with length $2 \times R_g$, it is possible to give an estimate of the number of charges making up this dipole. A classical dipole is defined as

$$\vec{p} = q \cdot \vec{l} \quad (4.8)$$

where \vec{p} is the dipole, q the charge separated by \vec{l} . For an induced dipole, one can write

(see Sec. 2.2.4)

$$\vec{p} = \alpha \vec{E}. \quad (4.9)$$

Combining these two equations, one can estimate the number of charges making up the induced dipole. The length of the dipole is assumed as $|\vec{l}| = 2R_g$, with R_g calculated from the diffusion coefficients (see Sec. 2.1.1). The polarizability and electric field in a trap are known (see Sec. 4.3.3). In consequence, only 10 elementary charges make up the induced dipole at a voltage $U_{ac} = 100$ V. Hogan et al. estimated 11 charges to be displaced along a 230 bp (78 nm) DNA fragment [160]. A similar number of 18 charges was derived by [148], but therein the charge displacement was assumed only along the Kuhn length ($2 \times l_p$). Although the agreement in the number of charges is interesting, the comparison of the values gives no evidence, whether the charges are displaced along the contour length or only the Kuhn length.

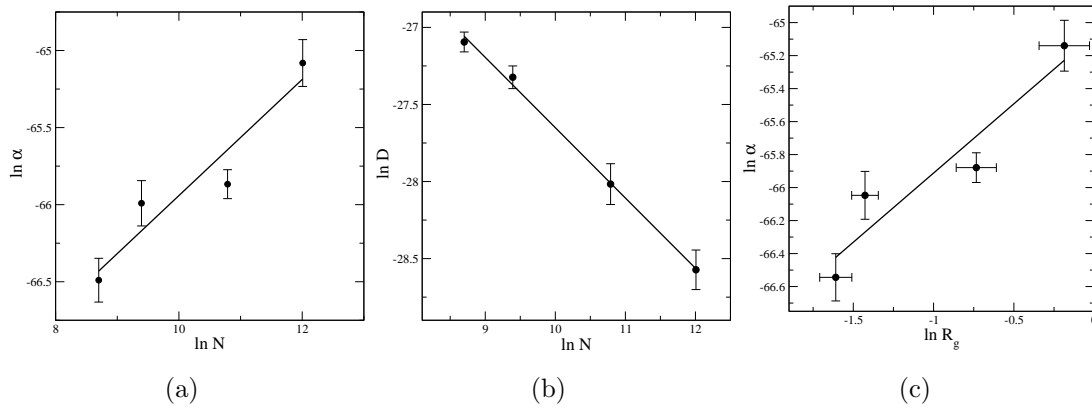


Figure 4.20: (a) Log-log plot of the polarizability of linear DNA versus the number of base pairs with a scaling exponent $\alpha \sim N^\gamma$ with $\gamma = 0.4 \pm 0.1$. (b) Log-log plot of the diffusion coefficient of linear DNA versus the number of base pairs, with an experimentally determined Flory exponent of $\nu = 0.45 \pm 0.05$ (negative sign omitted, which is due to plotting D instead of R_g). (c) Log-log plot of the radius of gyration calculated from the diffusion coefficient versus the polarizability, indicating a linear dependence because of the determined scaling exponent of 0.8 ± 0.2 .

Discussion of the Polarizability of Supercoiled DNA

So far, the polarizability of the supercoiled fragments have not be discussed (see Tab. 4.5). From 7 to 15,5 kbp fragment length, the polarizability increases with the number of base pairs. However, the 15,5 kbp DNA fragment has within the experimental error the same polarizability as the 21 kbp fragment. Thus, there is no clear dependence on length for these two fragments. A similar observation can be made, analyzing the coefficients of

diffusion (Tab. 4.7). Here, the 21 kbp fragment diffuses slightly faster than the 15,5 kbp fragment. This gives first evidence, why the 15,5 kbp and 21 kbp fragments have a similar polarizability, and supports the evidence presented for linear fragments, that the polarizability depends on the radius of gyration.

AFM images of the different supercoiled DNA fragments are taken in order to characterize the specific spatial configuration (for methods see Sec. 3.4). The images show (see Fig. 4.21) that the three smaller fragments (7, 10,5 and 15,3 kbp) have a plectonemic structure (see Sec. 2.1 and Ref. [161] for details), with clearly visible 'arms', whereas the 21 kbp plasmid shows a more 'random coil like' configuration. A transition from a plectonemic to a more random coil like structure is theoretically expected for supercoiled fragments in the range of about 25 kbp [47] and might thus explain the qualitatively different spatial configurations. These results indicate that the polarizability depends on the length of the fragment and the spatial configuration.

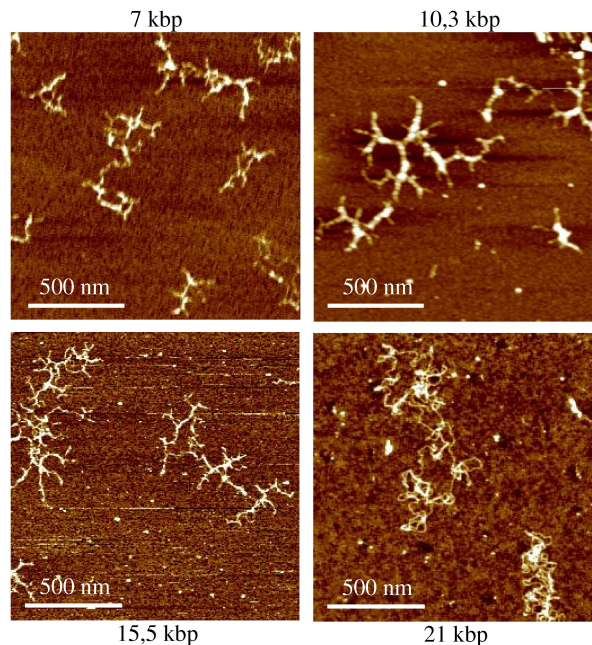


Figure 4.21: AFM images of the four different supercoiled DNA fragments. The first three samples show a clear plectonemic structure, looking more like a 'star'. The fourth sample is also supercoiled, but has a more random coil like structure.

In Fig. 4.22, a log-log plot is shown of the polarizability of the supercoiled fragments versus the radius of gyration. The polarizability of the ccc conformation scales with the radius, but with an exponent of 1.9 ± 0.3 . This indicates a fundamentally different scaling of the polarizability compared to the scaling of the linear fragments (0.8 ± 0.2 , see Sec. 4.3.4). A possible explanation could be a deformation of the plectonemically

conformed plasmids. If a dipole is induced in every plectonemic arm, the energetically favorable conformation is an orientation of the induced dipole parallel to the applied field, resulting in a 'cigare' like geometry.

Robertson et al. also determined diffusion coefficients of linear and supercoiled DNA fragments [48]. For a 11.1 kbp fragment, they found a diffusion coefficient of $1.17 \mu\text{m}^2/\text{s}$ for the linear fragment (corrected for the higher viscosity of 1.2 mPas) and $1.98 \mu\text{m}^2/\text{s}$ for the supercoiled fragment of equal length, with 50-80 % supercoiled DNA molecules in the sample. Furthermore, they reported on a Flory exponent for supercoiled DNA of $\nu = 0.571 \pm 0.057$. The diffusion coefficient for the linear DNA reported by Robertson et al. compares very well with the diffusion coefficient of the 12 kbp linear fragment ($D = 1.36 \pm 0.10 \mu\text{m}^2/\text{s}$) (see also Tab. 4.7). However, the diffusion coefficient of the supercoiled sample of comparable size (10,3 kbp with $D = 1.32 \pm 0.05 \mu\text{m}^2/\text{s}$) shows larger deviations and especially the observed Flory exponent shows very different scaling behavior, as in this study a Flory exponent for the supercoiled samples of $\nu = 0.9 \pm 0.1$ was determined from the values given in Tab. 4.7.

The differences in diffusion and scaling behavior indicate that the diffusion sensitively depends on the actual geometric configuration of the supercoiled DNA molecules. Hence, more experimental data is necessary to clarify the scaling and the actual geometric configuration should be carefully characterized, e.g. by AFM or SEM.

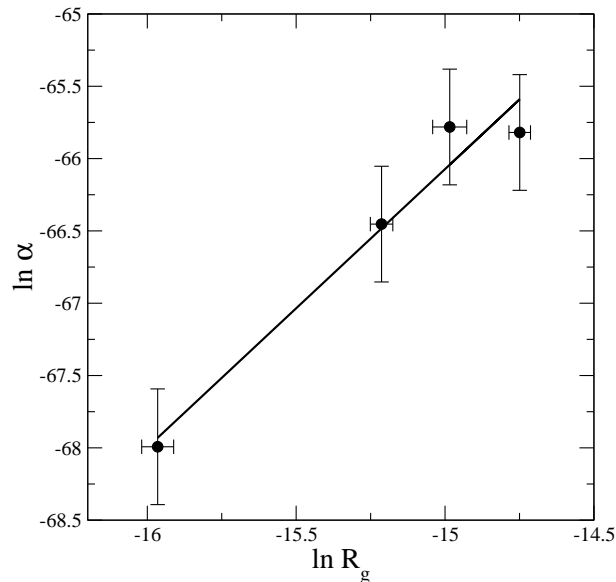


Figure 4.22: Log-log-plot of the radius of gyration versus the polarizability of supercoiled DNA fragments characterized in Fig. 4.21 and Tab. 4.7. The polarizability scales with the radius as $\alpha \sim R_g^{1.9 \pm 0.3}$.

Summary of the Polarizability of Linear and Supercoiled DNA

In summary, the new method to study the polarizability of DNA provides values comparable to the literature. Moreover, the results of the linear DNA fragments clearly demonstrate that the polarizability increases with length. First evidence is presented that the polarizability of long DNA molecules might scale with the radius of gyration. For supercoiled DNA molecules, the situation becomes more complicated. There is no simple scaling of the polarizability. Instead, first indications are given that the specific configuration of a molecule determines the polarizability. For molecules of similar configuration, the polarizability increases with the length of the fragment. Hence, in order to compare the polarizability of supercoiled DNA molecules, the length and the conformation must be known. Comparing equally long but differently conformed DNA fragments, different polarizabilities were observed. All these results confirm the separations of DNA fragments presented in Sec. 4.3.2.

4.3.5 Frequency Dependence of DNA Polarizability

So far, all experiments concerning the dielectrophoretic manipulation are conducted at $\omega = 60$ Hz. Fig. 4.23 shows the dependence of the average migration velocity on the frequency of the ac voltage for three different linear DNA fragments. A minimum in velocity means a maximum in the dielectrophoretic trapping force.

All DNA fragments show a minimum of velocity in a certain frequency range. The frequency, at which the minimum velocity is observed, seems to increase with decreasing DNA length. The problem is that there is no amplitude U_{ac} for which all fragments are still moving, i.e. not trapped, but also retarded by the dielectrophoretic traps, so that different amplitudes had to be chosen for every fragment. Thus, only a qualitative discussion seems appropriate.

Chou et al. [81] also reported on a clear maximum in the trapping force for a 39.8 kbp linear DNA fragment at 400 Hz, and a hint of a maximum for a 4.36 kbp fragment at 800 Hz. Thus, the here observed trend is confirmed that higher frequencies are necessary to efficiently manipulate shorter fragments. The differences in the observed frequencies are attributed to the different buffer conditions. Furthermore, Chou et al. varied the viscosity of the buffer and determined the frequency resulting in the maximum trapping force. They found that an increase in viscosity leads to a decrease of the frequency exerting the maximum force. Hence, they concluded that the DNA polarizability is due to the motion of the ions in the double layer along the DNA strand.

Assuming this model, it is interesting to check how long an Na^+ ion needs to migrate

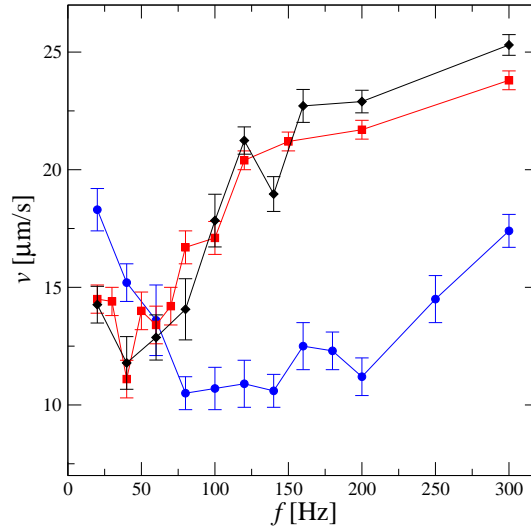


Figure 4.23: Frequency dependence of the migration velocity for 6 kbp measured at $U_{ac} = 234$ V (blue circles), for 48.5 kbp measured at $U_{ac} = 150$ V (red squares) and for 164 kbp measured at $U_{ac} = 138$ V (black diamonds). Thus, a direct comparison seems questionable, but a frequency minimum is observed for every fragment species. Additionally the frequency of the velocity minimum seems to shift towards larger frequencies for decreasing fragment length.

along the full contour length of the DNA strand. With a given mobility of Na^+ of $\mu(\text{Na}^+) = 5 \times 10^{-8} \text{ m}^2/\text{Vs}$ [162], the time needed for a displacement along the contour length of the DNA strand can be estimated with the known field strength in a trap (see Sec. 4.3.3). As the experiments are conducted with intercalated YOYO-1, the contour length is stretched, e.g. λ DNA is elongated from $16.4 \mu\text{m}$ to $\approx 20 \mu\text{m}$ [50]. All DNA lengths are scaled with this factor and the time is calculated, which a Na^+ ion needs to travel along the DNA strand for the U_{ac} used in the frequency measurement (Tab. 4.8) [163]. The calculated times, respectively maximum frequencies allowing an ion transport along the contour length of the DNA molecule, are found in the same order of magnitude as the frequency resulting in the maximum dielectrophoretic force and reflect the same trend. The frequency exerting the maximum force is smaller for longer fragments. The observed deviation at low frequencies is probably due to the dominating electrophoretic back and forth motion of DNA molecules below 40 Hz. Thus, this frequency sets the lower limit under the given experimental conditions.

In summary, the polarizability is frequency dependent. Moreover, there is a frequency for every fragment length that exerts a maximum trapping force. This frequency increases with decreasing fragment length.

N [kbp]	contour length [μm]	E_{trap} [V/m]	t_{ion} [ms]	ω_{max}^{theo} [Hz]	ω_{max}^{exp} [Hz]
6	2.4	49140	0.98	1023	≈ 140
48.5	20	31500	12.7	79	≈ 50
164	68	28980	47	21	≈ 50

Table 4.8: Estimate of the time (t_{ion}) a Na^+ ion needs to migrate along the contour length of a DNA strand, stretched by the intercalation of YOYO-1 with a given ion mobility of 5×10^{-8} m/Vs. From t_{ion} the maximum frequency ω_{max}^{theo} is calculated that allows an ion transport along the contour length and the observed frequency, that demonstrates the maximum trapping force, is given by ω_{max}^{exp} .

4.3.6 Salt Dependence of DNA Polarizability

The influence of the ionic strength on the polarizability of DNA is well documented and has been studied with several different techniques as birefringence and electric dichroism [85,89,98,164], demonstrating that the polarizability decreases with increasing ionic strength. The already known response of the polarizability on salt concentration gives another possibility to validate the quantitative results and the found scaling laws obtained with the new method presented here.

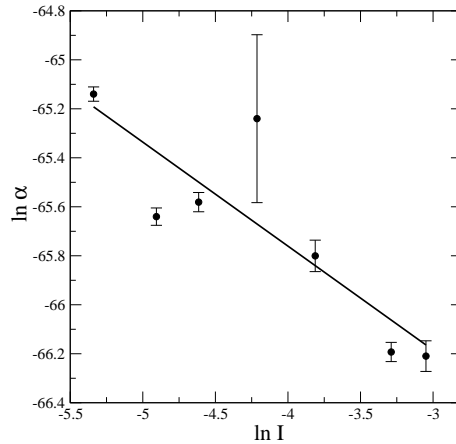


Figure 4.24: Dependence of the polarizability of a 12 kbp linear DNA fragment on the ionic strength. The polarizability decreases with increasing salt concentration. The linear fit results in a slope of 0.46 ± 0.02 , which indicates a scaling similar to the scaling of the Debye length with the ionic strength.

The polarizability is determined as described in Sec. 3.6.2. The composition of all samples studied is given in Sec. 3.4 and only the ionic strength is varied. In Fig. 4.24, the polarizability of a linear 12 kbp DNA fragment is plot versus different ionic strengths (see Tab. 3.2). The linear fit of the log-log-plot results in a slope of -0.46 ± 0.02 . Recalling the scaling of the Debye length with the ionic strength $\lambda_d \sim 1/\sqrt{I} \sim I^{-\frac{1}{2}}$, the same scaling is found within the experimental error, which was also reported by [98,148].

Thus, the new method developed here reproduces and confirms the data obtained by other techniques.

4.3.7 YOYO-1 Dependence of DNA Polarizability

The established techniques, which are used to measure polarizabilities of DNA, e.g. electric dichroism or birefringence, need no fluorescent staining of the DNA. As the method presented here, necessarily needs the staining, the question of the influence of the dye on the polarizability arises. In aqueous solution, YOYO-1 carries four positive charges. Thus, by intercalating, the charge density of the DNA fragment is changed. Moreover, the intercalation process leads to an increase in persistence length. And to my knowledge, there is no study addressing the dependence of the polarizability on fluorescent staining of DNA.

Fig. 4.25 shows the polarizability of a linear 12 kbp DNA fragment for different YOYO-1 concentrations, given in base pairs per dye molecule.

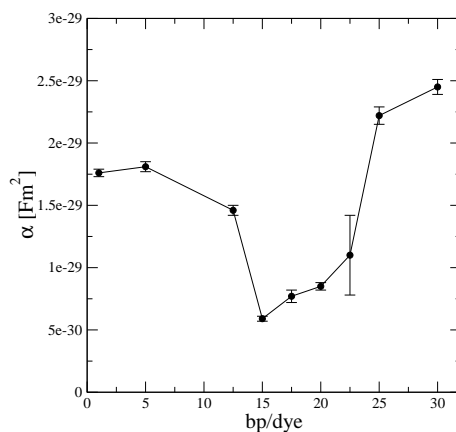


Figure 4.25: Dependence of the polarizability α of a 12 kbp linear DNA fragment versus the dye concentration (in base pairs per dye molecule). The polarizability changes nonmonotonic with the dye concentration.

The response behavior is non monotonic. The polarizability shows a minimum in the range of 15 to 20 base pairs per YOYO-1 molecule. Starting from low dye concentrations, the polarizability decreases with increasing dye concentration. This could be explained intuitively: with more intercalated dye, the total charge of the DNA-dye complex is reduced because the DNA carries two negative charges per base pair and the YOYO-1 four positive charges per molecule. Thus, the number of counterions needed to neutralize the DNA, which can in turn be polarized, is simply reduced. However, the increase towards higher dye concentrations cannot be explained with this simple picture.

A closer inspection of the binding process of YOYO-1 to DNA shows that at concentrations below 1 YOYO-1 per 8 base pairs, intercalation is the dominating binding process. Above this concentration, Larsson et al. reported that groove binding might also be possible. Thus, more YOYO-1 can bind to the DNA than there are intercalation sites [54, 55].

In a first approximation, the intercalated and otherwise bound YOYO-1 might be regarded as tetravalent ions. This point of view allows another possible explanation of the observed minimum in polarizability. Multivalent ions can induce a conformational collapse and subsequent reexpansion of DNA with increasing concentration. For example, Murayama et al. reported on a reduction followed by a reelongation of the radius of the DNA molecule with increasing concentration of trivalent ions [165]. The reduction of the radius can be understood as a better shielding of the charged DNA backbone. Thus, the repulsive interactions are reduced and the molecule takes a more compact conformation. So far, the reexpansion was often associated with the *overcharging* of DNA, i.e. extra ions are attracted despite the fact that the molecule is already neutralized [166]. However, overcharging goes along with a reversal of the electrophoretic direction of migration and this effect was not observed here with increasing YOYO-1 concentration. Only a weak dependence of the electrophoretic mobility without reversal was observed here. This is in accordance with results published by Carlsson et al. [57]. However, Hsiao et al. demonstrated in Monte Carlo simulations that a collapse and subsequent reexpansion can occur *without* overcharging, i.e. also without mobility reversal, for small trivalent ions [167]. As the effect strongly depends on the size and the geometry of the attracted ions [166], it seems possible that YOYO-1 might induce a similar effect. One possibility to check the validity of the proposed idea would be to measure the diffusion coefficient for various dye concentrations. Shimizu et al. made such a study, but the accuracy is not sufficient for a conclusive answer [168].

On the first glance, the observed minimum of polarizability for YOYO-1 and regarding the dye as a multivalent ion might contradict the observed dependence of the polarizability on the concentration of NaCl ($\alpha \sim I^{-\frac{1}{2}}$), as only a monotone dependence was observed. However, NaCl is a monovalent ion and, to my knowledge, no experimental evidence has been presented that monovalent ions induce a reexpansion [167].

In summary, the fluorescent staining has an influence on the polarizability. But the dependence is rather weak. Although the dye concentration was varied by a factor of 30, the polarizability changed from an average over all dye concentrations only by 80 %. Moreover, a possible explanation of the observed minimum of polarizability with increasing dye concentration was presented. It amends the evidenced dependence of

the polarizability on the radius of gyration. The explanation should be confirmed by determining the radius of gyration from the diffusion coefficients for different YOYO-1 concentrations.

4.3.8 Summary

The dielectrophoretic trapping of DNA is demonstrated and the migration of the DNA in the trap visualized. With the developed separation protocol, the separation of linear and supercoiled DNA according to polarizability is presented. Through the quantitative description of the DNA migration, a new method is worked out, which allows the quantitative determination of DNA polarizabilities quickly and with small sample volumes. Although several assumptions are implied, the obtained values compare well with the values found in the literature, considering the range of four orders of magnitude. Moreover, the reported scaling of the polarizability with the ionic strength could be reproduced. The new method allows to compare the polarizability of DNA under varying conditions and conformations. For linear DNA, an increase of the polarizability with length and first evidence for a scaling with the radius of gyration is demonstrated. For supercoiled DNA, the polarizability depends on length and the spatial configuration of the fragments. Furthermore, DNA polarizability depends on the frequency of the applied ac voltage, on the ionic strength and also in a non monotonic manner on the concentration of YOYO-1.

4.4 Giant DNA Diffusion

Usually, diffusion is considered a nuisance, especially in separation science as it leads to peak broadening. However, if there was a way to specifically control diffusion, this might have important implications to microfluidic applications. Because of the very small Reynolds number in microfluidic devices, mixing is difficult as there are no turbulences (see Sec. 2.2.1). Consequently, mixing is mostly based on diffusion and if the diffusion could be enhanced, this would lead to faster mixing. On the other hand, let us consider a sample consisting of two species. The sample is injected as a small plug into a microchannel. If the diffusion enhancement could be 'switched on' only for one species, the first species would spread out very quickly, while the other would only undergo the 'normal' diffusion. This would lead to a purification of the second species. In this section, the specific control of diffusion of DNA is addressed in a microfluidic environment.

The diffusion of a single force-free Brownian particle in an overdamped system at thermal equilibrium is always reduced when an additional periodic potential is switched on [120]. However, as already demonstrated in the sections about ANM and the ratchet (see Secs. 4.1 and 4.2), the response of a system far from thermal equilibrium to a perturbation can be counterintuitive. Thus, the question arises how the diffusion coefficient of a Brownian particle in a periodic potential will respond to a static perturbation, creating conditions far from thermal equilibrium. For a point-like particle, Reimann et al. reported in a theoretical study that the effective diffusion coefficient of a Brownian particle in a periodic potential can be greatly enhanced in case the system is far from thermal equilibrium [121, 122].

The idea of diffusion enhancement is the following. In case of a deterministic and overdamped dynamics, a particle in a periodic potential landscape is confined to a potential minimum. Tilting of this potential landscape leads to a decreasing potential barrier, which the particle has to overcome, in order to migrate to the next minimum. Hence, at some point, the so called *critical tilt* is reached, i.e. the potential minimum has become a potential 'plateau'. At this tilt, any further tilting leads to a deterministic migration of the particle 'downhill'. Now, taking into account the thermal noise, a small thermal perturbation is enough to kick the object from the plateau. This small fluctuation is greatly enhanced by the subsequent dynamical evolution and the result is a huge dispersion, if an ensemble of particles is subjected to different realizations of the thermal noise [121]. If the dynamics was not overdamped, the dynamics at the plateau would be dominated by inertia, i.e. inertia forces would drive the particle over all plateaus once it started to move, and the diffusion enhancement would vanish.

In order to realize such a tilted periodic potential landscape with overdamped dynamics, microfluidics again is a very suitable system (cp. Sec. 2.2.1) and the same setup can be used as in Sec. 4.3. Briefly, an ac voltage U_{ac} is applied to a microfluidic chip, whose design is shown in Fig. 4.26. The positive dielectrophoretic trapping of DNA in response to U_{ac} is exploited in the microfluidic channel with a periodicity of the structure L , to generate a spatially periodic potential landscape. Additionally, a static voltage U_{dc} is applied to tilt the potential (see Fig. 4.26).

The diffusion can be determined with Eqs. 2.19 and 2.29. The latter,

$$D = \frac{L^2 \langle t^2(x_0 \rightarrow x_0 + L) \rangle - \langle t(x_0 \rightarrow x_0 + L) \rangle^2}{2 \langle t(x_0 \rightarrow x_0 + L) \rangle^3}, \quad (4.10)$$

has the advantage, that it converges faster [70], which is of importance because of the finite number of objects that can be observed. However, the equation applies only to a point particle and to a 1D Markov process [135], i.e. subsequent escape events have

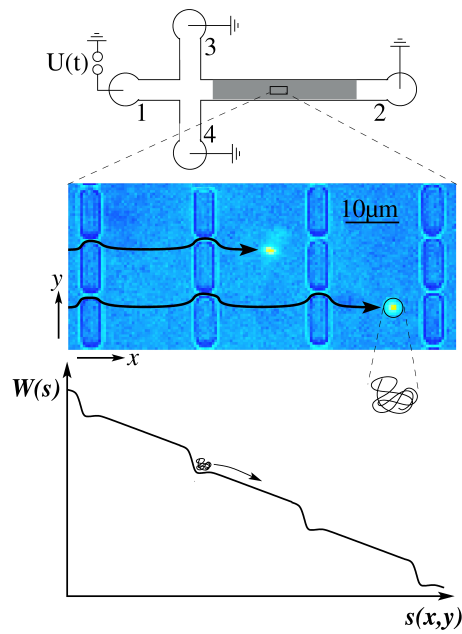


Figure 4.26: A schematic of the experimental setup is shown. It is the same as in Sec. 4.3 (see there for specifications). The microfluidic device consists of a cross injector and a microstructured channel. Voltages are applied as indicated for the observation of diffusion enhancement. The enlargement shows an optical micrograph of the microstructure with two DNA molecules. The arrows indicate two typical trajectories. Below, the 1D potential landscape along a typical trajectory ($s(x,y)$, see also main text) is depicted schematically, near the critical tilt.

to be uncorrelated, and the dynamics has to be reduced to 1D. As we have already omitted the z direction, because of the assumed isotropy (see Sec. 2.5), the system reduces to 2D. A further reduction is possible because of the experimentally observed dynamics. Every trapping event 'resets' the molecule to some kind of initial condition, i.e. the escape events are uncorrelated and a Markov process can be assumed in good approximation. And because the dynamics of the objects is dominated by the escape from a trap, and not by the motion from trap to trap, where different 2D paths are possible, the system might be reduced to 1D. This is supported by the fact that it is only rarely observed that a DNA molecule 'changes the lane' in y direction. Hence, in good approximation, the DNA migration can be described along a parameterized 1D path $s(x, y)$.

Furthermore, the DNA molecules have to be assumed as globular, without an internal dynamics. As already discussed in Sec. 4.3.3, the deformation energy, which a DNA molecule is subjected to in a trap, is smaller than $k_B T$. Moreover, the relaxation time from a deformation is only about 0.1 s for λ DNA and about 0.6 s for T2 DNA [169–171]. Thus, if the molecules were deformed, they could relax on their migration from trap to trap.

In order to experimentally demonstrate *Giant DNA Diffusion*, the DNA migration is observed for different tilts and the first passage time is determined, here given by the time a molecule needs from entering one trap to entering the next ahead.

The results for two different DNA species under the same electrical conditions ($\omega = 60$ Hz and $U_{ac} = 240$ V) are shown in Fig. 4.27. For both species a peak in diffusion is observed, i.e. the diffusion of the λ -DNA is enhanced by a factor 180 and the T2-DNA by even a factor of 700 compared to the free diffusion ($D(\lambda) = (0.68 \pm 0.09) \mu\text{m}^2/\text{s}$ and $D(T2) = (0.39 \pm 0.05) \mu\text{m}^2/\text{s}$, see also Tab. 4.7). For the shorter λ DNA, the critical tilt is found at a smaller U_{dc} compared to the T2 DNA. This is in accordance with the determined polarizabilities (see Sec. 4.3.4). The depth of the potential for a polarizable object is given by $W = -(1/2)\alpha\vec{E}^2$ (see Sec. 2.2.4). Thus, a smaller molecule is subjected to a less deep potential minimum and a smaller U_{dc} already results in a critical tilting.

There are several points to notice: the smallest U_{dc} value, for which the diffusion coefficient can be determined, is given by the fact that all injected DNA molecules have to pass by the detector, i.e. they have to escape during the observation time, in order not to distort the distribution of the ensemble. However, because of the finite observation time, the tail of the distribution for very long first passage times is cut off and the distribution is distorted. The impact is checked by removing very long trapping times

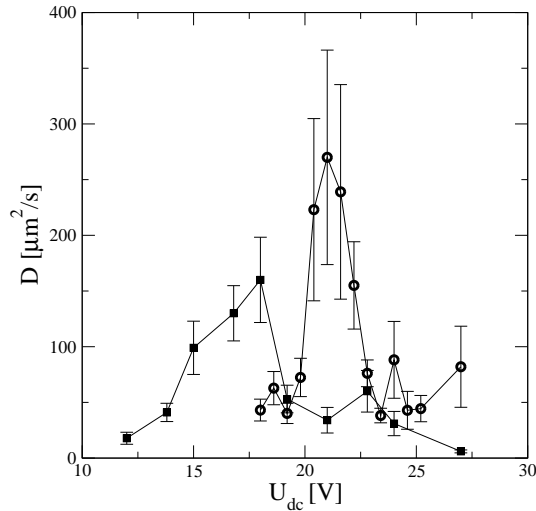


Figure 4.27: DNA diffusion enhancement for λ -DNA (squares) and T2-DNA (dots). The diffusion is enhanced by a factor of 180 and 700 respectively compared to the free diffusion coefficient ($D(\lambda) = (0.68 \pm 0.09) \mu\text{m}^2/\text{s}$, $D(T2) = (0.39 \pm 0.05) \mu\text{m}^2/\text{s}$). For both species an ac voltage of $U_{ac} = 240$ V and $\omega = 60$ Hz is applied. The diffusion coefficient is determined according to the first passage time (Eq. 4.10). The fluctuations are due to the limited number of recorded first passage times (about 30 per data point). The error bars are obtained from a boot strap, where only 75 % of the data points were considered.

from the distribution of the observed first passage times and only a marginal change in diffusion is found.

As can be seen in Fig. 4.27, even for strong tilts, the diffusion coefficient does not approach the value of the free diffusion. Closer analysis of the video data reveals that there is a potential saddle point at the center of each post, where the electric field lines split up and lead around the post. If a molecule hits the post at its center, it is hardly transported by the electric field because of its weakness at this point. Instead the molecule has to diffuse away from this saddle point. Thus, there is already some U_{ac} independent dispersion due to microstructure and the dimensionality. Moreover, the molecules could take different paths through the microstructure by diffusing in y -direction. This process would increase the dispersion, but it is observed very rarely.

Despite these processes, which already shift the diffusion towards higher values, the actual diffusion enhancement peak is only observed when the U_{dc} field is applied near the critical tilt.

This analysis also holds for the performed separation experiments (see Sec. 4.3.2). The microstructure itself induces an increased diffusion, which leads to peak broadening. This implies that the distance on which the separation is performed should be kept as short as possible, again improving the separation time. The phenomenon of the

diffusion enhancement is also possible during the separation experiment. Physically, it makes no difference if the potential is tilted until the critical tilt is reached by increasing U_{dc} , or if the potential minima are deepened by increasing U_{ac} . However, the diffusion enhancement is only observed right at the critical tilt. Hence, the probability of accidentally creating a critical tilt with the separation protocol is rather small, especially if the voltage ramp is 'coarse grained.'

Finally, the large fluctuations for strong tilting are due to the limited number of recorded frames per second (10 fps, see Sec. 3.6.2). For strong tilting, the DNA migrates from row to row within less than 5 frames. Thus, there is a deviation of 20 % in the first passage time, whether the fragment migrates within 4 or 5 frames from row to row.

In summary, the critical tilt is found at different U_{dc} -values, in accordance with the different polarizabilities of the DNA species. The diffusion enhancement for two different DNA species is demonstrated, with an enhancement up to a factor of 700 compared to the free diffusion. The only other study concerning diffusion enhancement, which is known to the author, was published by Lee and Grier [172]. They observed a diffusion enhancement by a factor of 100 for a single size of colloidal spheres in corrugated optical vortices with fluctuating potential barrier height.

The most interesting observation is that the diffusion can be controlled and can be 'switched on' for specific species. This could be exploited for mixing and purification, as stated at the beginning of this section. The experimental concept presented here, can be extended to all polarizable objects, such as proteins or carbon nanotubes.

5 Summary and Outlook

The leitmotif of this thesis is to exploit Brownian motion for bioanalysis in microfluidic systems operating far from thermal equilibrium.

For the first time, non-interacting micron sized particles moved opposite to a net acting force, an effect termed Absolute Negative Mobility (ANM) (see Sec. 4.1). The effect was realized in an array of microstructured geometric traps. ANM could then be exploited to separate differently sized but alike charged particles by simultaneously steering them into opposite directions (see Sec. 4.1.2). Interestingly, although the phenomenon of ANM is based on the existence of noise, its main limiting factor concerning the achievable velocities is the *weakness* of the thermal noise. Therefore, different possibilities to accelerate ANM were discussed and a microstructure, optimized in computer simulations was realized. An acceleration of ANM by one order of magnitude could be demonstrated in the direction opposite to the force as well as in the 'normal' direction (see Sec. 4.1.3).

The possibility to separate colloids by steering them into opposite directions was further explored in an electrodeless dielectrophoretic ratchet. The ratcheting of micron sized particles could be demonstrated (see Sec. 4.2). More importantly, first evidence was presented that with a single experimental parameter the separation criterion can be 'tuned.' The latter effect was demonstrated simultaneously for three different particle species. This result allows new perspectives and strategies for particle and cell separation.

Turning to biomolecules, in 1991 Ajdari and Prost proposed to separate DNA according to its polarizability and this idea was finally realized in an array of electrodeless dielectrophoretic traps. Those were created with non-conducting posts under the application of an ac voltage superimposed by a dc voltage. In order to find the right balance of the trapping force, the thermal noise, responsible for the escape from a trap, and the free migration velocity, the separation was performed while undergoing a special separation protocol, i.e. the trapping force was discretely increased during the migration of the DNA through the separation channel. Only this approach led to the successful separations of two long linear fragments and two supercoiled fragments. More importantly,

especially concerning possible applications for quality control of plasmid DNA, the separation of differently conformed DNA fragments was demonstrated, namely supercoiled DNA was separated from the equally long linear DNA fragment and the supercoiled dimer. Baseline resolution was achieved within less than 240 s (see Sec. 4.3.2).

The same device was then used to develop a new method to quantify the polarizability of DNA. The polarizability can be calculated by determining the DNA escape time from a dielectrophoretic trap for different trapping forces (see Sec. 4.3.3). The method was applied to four linear fragments (6 to 164 kbp) and four supercoiled fragments (7 to 21 kbp) (see Sec. 4.3.4). An increase of the polarizability with length was observed, except for the 21 kbp supercoiled fragment, which showed a different spatial configuration (see Secs. 4.3.4 and 4.3.4). The length dependence for the linear fragments, however, is quite weak. Evidence was presented that the polarizability of the linear fragments scales with the end-to-end distance of the DNA molecule (see Sec. 4.3.4). Nevertheless, the separation is efficient because differences in polarizability are amplified exponentially.

Results from the literature, concerning the salt dependence of the polarizability could be reproduced (see Sec. 4.3.6) confirming the validity of the new method. To my knowledge for the first time, the dependence on the fluorescent dye concentration was studied (see Sec. 4.3.7). It was shown that the polarizability depends in a non monotonic manner on the concentration and possible explanations were discussed. Furthermore, the frequency dependence was studied and it was shown that higher frequencies allow for the trapping of smaller molecules (see Sec. 4.3.5).

Last but not least, the diffusion of DNA in a tilted periodic potential was studied (see Sec. 4.4). The potential landscape was designed with nonconducting posts and electric ac and dc voltages. To my knowledge, only one example of diffusion enhancement with a single particle size was demonstrated experimentally so far with an increase of diffusion compared to the free diffusion by a factor 100. Here, the giant diffusion is demonstrated for two different linear DNA fragments with the diffusion enhanced by a factor 700 compared to the free diffusion. Furthermore, and much more relevant for possible practical applications, the giant diffusion can specifically be 'switched on and off' for a one species, while another species undergoes 'normal' diffusion. This allows for novel approaches to fast mixing as well as for sample purification.

For ANM, the separation of cells seems a valuable next step. The trapping mechanism needs no further modification, and even the surface chemistry is applicable to cell handling. Thus, long-term objectives as the separation of stem or cancer cells might be anticipated. More difficult is the application of ANM to biomolecules. Therefore,

substantial modifications of the basic physical trapping mechanism will be necessary.

Concerning the ratchet, firstly, it is necessary to further study the fundamental physics, with a combination of numerical simulations and experiments. The goals are optimized geometries and driving parameters that allow a maximum of flexibility concerning the adjustability of the separation criterion. Then, the concept should be applied to the separation of cells or biomolecules, as already energetic traps are used, allowing the manipulation of smaller objects.

The new concept of specific diffusion control should be used to experimentally demonstrate the enhanced mixing. For the purification, substantial modifications to the setup are necessary, as purification only makes sense, if the purified sample can be extracted from the chip.

The simplicity of the newly developed measurement method for the DNA polarizability may open the way to further systematic experimental studies including its dependence on the ac driving frequency, buffer conditions and used dyes. However, the method itself needs to be studied in more detail: the possible deformation of plectonemic molecules should be studied, and the influence of the DNA motion in the trap. The first obtained results concerning the YOYO-1 influence on the polarizability, can be checked by determining the radius of gyration for different YOYO-1 loads. Moreover, the possible deformation of plectonemically shaped plasmids in an electric field might be verified by AFM.

Both principles - dielectrophoretic separation and polarizability measurements - are not restricted to DNA, but may be applied to any polarizable migrant, e.g. proteins. In particular, a closer look at the polarizability of different topological conformations seems promising, although care should be taken to characterize the actual spatial configuration. Moreover, the separation of all three different conformations of DNA (ccc, oc linear) should be addressed. This might have direct impact on the quality control of plasmid samples for biotechnological applications like gene therapy and DNA vaccination.

Appendix

Theoretical derivation of the automated determination of average migration time

Here, it is demonstrated that the time $\langle t \rangle$ obtained in Sec. 3.7 is indeed the average migration time of the ensemble [173]. Therefore some distributions are defined.

- $\Psi_{esc}(t)$ Distribution of trapping times
- $\Psi_0(t)$ Distribution of migration times in between two traps
- $\Psi_+(t)$ Distribution before entering the trap array

The distribution after N traps thus follows as

$$H_N(t) = \int d\tilde{t} \Psi_+(\tilde{t}) \int \prod_{i=1}^N dt_i dt'_i \Psi_{esc}(t_i) \Psi_0(t'_i) \cdot \delta \left[t - \left(\tilde{t} + \sum_{k=1}^N t_k + t'_k \right) \right]. \quad (5.1)$$

Assuming the validity of a rate description for the escape process from a trap, i.e. $k_B T \ll \Delta W$, $\Psi_{esc}(t)$ can be written as

$$\Psi_{esc}(t) = \frac{1}{\tau} \exp \left(-\frac{t}{\tau} \right). \quad (5.2)$$

Assuming further that the DNA plug at the time of the injection has the shape of a δ -peak, which seems reasonable comparing the peak width at the injection and after several passed traps, and that the dispersion is only due to trapping, not the free migration, i.e. $\Psi_0(t) = \delta(t - t_0)$ and $\Psi_+(t) = \delta(t - t_+)$, with t_0 the migration time from one row of traps to next with $U_{ac} = 0$ and t_+ the time needed from the injector to the trap array, with $t_{free} = t_+ + Nt_0$, one gets

$$H_N(t) = \int \prod_{i=1}^N dt_i \Psi_{esc}(t_i) \cdot \delta \left(t - t_{free} - \sum_{k=1}^N t_k \right). \quad (5.3)$$

This equation can be solved with a Laplace Transformation and the final result is

$$H_N(t) = \frac{1}{\tau(N-1)!} \cdot \left(\frac{t-t_{free}}{\tau}\right)^{N-1} \cdot \exp\left(-\frac{t-t_{free}}{\tau}\right) \cdot \Theta(t-t_{free}), \quad (5.4)$$

with $\Theta(t-t_{free})$ being the Heaviside function. Thus, one can calculate the average migration time as

$$\langle t \rangle = \int dt \cdot t \cdot H_N(t) = \tau N + t_{free} \quad (5.5)$$

Tracking with camera noise

Equation 2.30 can be derived as follows [125]:

$P(\vec{r}, t)$ is the probability to find the particle at the position \vec{r} at the time t

$$P(\vec{r}, t) = \frac{1}{4\pi Dt} \exp\left(-\frac{r^2}{4Dt}\right) \quad (5.6)$$

The probability $P(\vec{r}, \vec{r}')$ to find the particle due to camera noise at the position \vec{r}' although it is at the position \vec{r} is given by

$$P(\vec{r}, \vec{r}') = \frac{1}{2\pi\sigma^2} \exp\left(-\frac{|\vec{r} - \vec{r}'|^2}{2\sigma^2}\right) \quad (5.7)$$

with σ the average deviation of the position. The probability to find the particle at \vec{r}' for time t can then be derived as

$$\begin{aligned} P'(\vec{r}', t) &= \int_0^\infty r dr \int_0^{2\pi} d\Theta P(\vec{r}, t) P(\vec{r}, \vec{r}') \\ &= \int_0^\infty r dr \int_0^{2\pi} d\Theta \frac{1}{4\pi Dt} \frac{1}{2\pi\sigma^2} \exp\left(-\frac{r^2}{4Dt} - \frac{|\vec{r} - \vec{r}'|^2}{2\sigma^2}\right) \end{aligned} \quad (5.8)$$

Expansion of the exponent with Θ , the angle between \vec{r} and \vec{r}' , leads to

$$-\frac{r'^2}{2\sigma^2} - \frac{(2\sigma^2 + 4Dt)r^2}{2\sigma^2 4Dt} + \frac{2rr' \cos \Theta}{2\sigma^2} \quad (5.9)$$

The integral over the angle results in [174]

$$\int_0^{2\pi} d\Theta \exp\left(\frac{rr'}{\sigma^2} \cos \Theta\right) = 2\pi J_0\left(i\frac{rr'}{\sigma^2}\right) \quad (5.10)$$

with J_0 the Bessel function. Integration over r gives without prefactors [174]

$$\int_0^\infty r dr \exp\left(-\frac{2\sigma^2 + 4Dt}{2\sigma^2 4Dt} r^2\right) J_0\left(i\frac{rr'}{\sigma^2}\right) = \frac{1}{2} \frac{2\sigma^2 4Dt}{2\sigma^2 + 4Dt} \exp\left(\frac{4Dt}{2\sigma^2(2\sigma^2 + 4Dt)} r'^2\right). \quad (5.11)$$

Thus

$$\begin{aligned} P'(\vec{r}', t) &= \frac{1}{4\pi Dt} \frac{1}{2\pi\sigma^2} 2\pi \frac{1}{2} \frac{2\sigma^2 4Dt}{2\sigma^2 + 4Dt} \exp\left(\left(\frac{4Dt}{2\sigma^2(2\sigma^2 + 4Dt)} - \frac{1}{2\sigma^2}\right) r'^2\right) \\ &= \frac{1}{\pi(2\sigma^2 + 4Dt)} \exp\left(-\frac{r'^2}{2\sigma^2 + 4Dt}\right) \end{aligned} \quad (5.12)$$

and finally the result is

$$\begin{aligned} \langle \vec{r}'^2 \rangle &= \int_0^\infty 2\pi r' dr' r'^2 \frac{1}{\pi(2\sigma^2 + 4Dt)} \exp\left(-\frac{r'^2}{2\sigma^2 + 4Dt}\right) \\ &= 2\sigma^2 + 4Dt \end{aligned} \quad (5.13)$$

Contact unit for exposure during lithography process

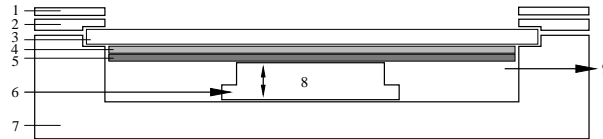


Figure 5.1: Scheme of the pneumatic pressure unit. An aluminum frame (1) presses a gasket (2) onto the chromium mask (3) and the outer frame of the unit (7). The wafer (4) lies on a aluminum plate (5), which can be lifted with a pneumatic die (8), which is actuated through nitrogen via (6), and hence presses the wafer against the mask. The remaining cavity inside the unit can be evacuated via a valve (9).

The resolution of a contact lithography process is limited by the quality of the contact. Ideally, there is no spacing between the photo resist and the chromium mask. In order to obtain tighter contact, a pneumatic contact unit was constructed. After spin coating, the wafer is placed in the unit. A pneumatically driven die, placed underneath the wafer, presses the wafer against the mask. Simultaneously, the evacuation of the chamber begins and the atmospheric pressure bears down the chromium mask. Thus the wafer is pressed upwards and the mask downwards, assuring a good contact when both forces cancel out each other.

List of Publications

1. A. Ros, R. Eichhorn, J. Regtmeier, T.T. Duong, P. Reimann, and D. Anselmetti. Brownian Motion: Absolute Negative Particle Mobility, *Nature*, 436:928, 2005.
2. W. Hellmich, J. Regtmeier, T.T. Duong, R. Ros, D. Anselmetti, A. Ros. Poly(ethyleneoxide) Based Surface Coatings for Poly(dimethylsiloxane) Microchannels, *Langmuir*, 21:7551-7557, 2005.
3. A. Ros, W. Hellmich, J. Regtmeier, T. T. Duong and D. Anselmetti. Bioanalysis in Structured Microfluidic Systems, *Electrophoresis*, 27:2651-2658, 2006.
4. R. Eichhorn, A. Ros, J. Regtmeier, T.T. Duong, P. Reimann, and D. Anselmetti. Paradoxical Brownian Motion in a Microfluidic Device: Absolute Negative Mobility, *European Physical Journal Special Topics*, 143:159-167, 2007.
5. J. Regtmeier, R. Eichhorn, T.T. Duong, P. Reimann, D. Anselmetti, and A. Ros. Pulsed-field Separation of Particles in a Microfluidic Device, *European Physical Journal E*, 22:335-340, 2007.
6. J. Regtmeier, S. Grauwin, R. Eichhorn, P. Reimann, D. Anselmetti, and A. Ros. Acceleration of Absolute Negative Mobility, *Journal of Separation Science*, 30:1461-1467, 2007.
7. J. Regtmeier, T.T. Duong, R. Eichhorn, D. Anselmetti, and A. Ros. Dielectrophoretic Manipulation of DNA: Separation and Polarizability, *Analytical Chemistry*, 79:3925-3932, 2007.
8. J. Regtmeier, R. Eichhorn, P. Reimann, A. Ros, D. Anselmetti. Giant DNA diffusion, in preparation

List of Conference Proceedings

1. J. Regtmeier, T. Duong, R. Eichhorn, D. Anselmetti, P. Reimann, and A. Ros. Novel Migration Phenomena in Structured Microfluidic Devices, Micro Total Analysis Systems Vol. 1, 340-342, 2005, Proceedings of the μ TAS 2005, Boston, (ISBN: 0-9743611-1-9)
2. J. Regtmeier, T.T. Duong, A. Ros, D. Anselmetti. Fast Separation of λ - and T2-DNA with Electrodeless Dielectrophoresis, Micro Total Analysis Systems Vol.

- 1, 383-385, 2006, Proceedings of the μ TAS 2006, Tokyo, (ISBN: 4-9903269-0-3-C3043)
3. J. Regtmeier, R. Eichhorn, P. Reimann, A. Ros, D. Anselmetti. Acceleration of Absolute Negative Mobility for Particle Sorting in a Microfluidic Device, *Micro Total Analysis Systems Vol. 1*, 648-650, 2006, Proceedings of the μ TAS 2006, Tokyo, (ISBN: 4-9903269-0-3-C3043)
4. J. Regtmeier, H. Höfemann, R. Eichhorn, D. Anselmetti, and A. Ros. Separation and Polarizability of DNA by Dielectrophoresis, Proceedings of the μ TAS 2007, Paris, in press, 2007

Contributions to Conferences

1. J. Regtmeier, R. Eichhorn, P. Reimann, D. Anselmetti, A. Ros. Experimental Proof of Absolute Negative Mobility of Single Brownian Particles, Spring Meeting of the German Physical Society, March 4 -9, 2005, Berlin, Germany. (Talk)
2. J. Regtmeier, R. Eichhorn, D. Anselmetti, P. Reimann, A. Ros. Absolute negative mobility in a microfluidic system, *Physics & Chemistry of Microfluidics*, August 21-26, 2005, Oxford, Great Britain. (Poster)
3. J. Regtmeier, T.T. Duong, D. Anselmetti, A. Ros. DNA separation via dielectrophoresis on a microfluidic chip, *Microscale Bioseparation 2006*, January 23-26, 2006, Amsterdam, The Netherlands. (Poster)
4. A. Ros, J. Regtmeier, T.T. Duong, D. Anselmetti. Sorting in Structured Microfluidic Devices, Spring Meeting of the German Physical Society, March 27 -31, 2006, Dresden, Germany.
5. J. Regtmeier, T.T. Duong, D. Anselmetti, A. Ros. Elucidating the dielectrophoretic separation of DNA, ICN+T, International Conference on Nanoscience and Technology, July 30-August 4, 2006, Basel, Switzerland. (Talk)
6. J. Regtmeier, T.T. Duong, D. Anselmetti, A. Ros. Fast separation of λ - and T2-DNA with electrodeless dielectrophoresis, μ TAS 2006, The 10th International Conference on Miniaturized Systems for Chemistry and Life Sciences, November 5-9, 2006, Tokyo, Japan. (Poster)

-
7. J. Regtmeier, R. Eichhorn, P. Reimann, A. Ros, D. Anselmetti. Acceleration of Absolute Negative Mobility For Particle Sorting in a Microfluidic Device, μ TAS 2006, The 10th International Conference on Miniaturized Systems for Chemistry and Life Sciences, November 5-9, 2006, Tokyo, Japan. (Poster)
 8. J. Regtmeier, T.T. Duong, R. Eichhorn, K. Tönsing, D. Anselmetti, A. Ros. Separation and molecular polarizability of DNA via electrodeless dielectrophoresis, The 42nd Winterseminar, Biophysical Chemistry, Molecular Biology and cybernetics of cell functions, January 13-27, 2007, Klosters, Switzerland. (Poster and Talk)
 9. J. Regtmeier, H. Höfemann, T.T. Duong, R. Eichhorn, D. Anselmetti, A. Ros. Separation and Polarizability of DNA by Dielectrophoresis, μ TAS, September 2007, Paris, France. (Poster)

Bibliography

- [1] E. Frey and K. Kroy. Brownian motion: a paradigm of soft matter and biological physics. *Ann. Phys.*, 14:20–30, 2005.
- [2] Y. Xia and G. Whitesides. Soft lithography. *Annu. Rev. Mater. Sci.*, 28:153–184, 1998.
- [3] P. Yager, T. Edwards, E. Fu, K. Helton, K. Nelson, M.R. Tam, and B.H. Weigl. Microfluidic diagnostic technologies for global public health care. *Nature*, 442:412–418, 2006.
- [4] D.J. Harrison, A. Manz, Z. Fan, H. Lüdi, and H.M. Widmer. Capillary electrophoresis and sample injection systems integrated on a planar glass chip. *Anal. Chem.*, 64:1926–1932, 1992.
- [5] D. Reyes, D. Iossifidis, P. Aurox, and A. Manz. Micro total analysis systems. 1. introduction, theory, and technology. *Anal. Chem.*, 74:2623–2636, 2002.
- [6] J. Khandurina, T. E. McKnight, S. C. Jacobson, L. C. Waters, R. S. Foote, and J. M. Ramsey. Integrated system for rapid PCR-based DNA analysis in microfluidic devices. *Anal Chem*, 72:2995–3000, 2000.
- [7] C.L. Hansen, E. Skordalakes, J.M. Berger, and S.R. Quake. A robust and scalable microfluidic metering method that allows protein crystal growth by free interface diffusion. *Proc. Natl. Acad. Sci. (USA)*, 99:16531–16536, 2002.
- [8] International Human Genome Sequencing Consortium. Finishing the euchromatic sequence of the human genome. *Science*, 431:931–945, 2005.
- [9] M. Schleef, editor. *DNA pharmaceuticals: formulation and delivery in gene therapy, DNA vaccination and immunotherapy*. Weinheim: WILEY-VCH, 2005.
- [10] N. C. Stellwagen, C. Gelfi, and P. G. Righetti. The free solution mobility of DNA. *Biopolymers*, 42:687–703, 1997.

-
- [11] L.R. Huang, J.O. Tegenfeldt, J.J. Kraeft, J.C. Sturm, R.H. Austin, and E.C. Cox. A DNA prism for high-speed continuous fractionation of large DNA molecules. *Nature Biotechnol.*, 20:1048–1051, 2002.
- [12] L. Huang, E. Cox, R. Austin, and J. Sturm. Continuous particle separation through deterministic lateral displacement. *Science*, 304:987–990, 2004.
- [13] O. Bakajin, T. A. Duke, J. Tegenfeldt, C. F. Chou, S. S. Chan, R. H. Austin, and E. C. Cox. Separation of 100-kilobase DNA molecules in 10 seconds. *Anal. Chem.*, 73:6053–6056, 2001.
- [14] N. Kaji, Y. Tezuka, Y. Takamura, M. Ueda, T. Nishimoto, H. Nakanishi, Y. Horiike, and Y. Baba. Separation of long DNA molecules by quartz nanopillar chips under a direct current electric field. *Anal. Chem.*, 76:15–22, 2004.
- [15] P.S. Doyle, J. Bibette, A. Bancaud, and J.-L. Viovy. Self-assembled magnetic matrices for DNA separation chips. *Science*, 295:2237, 2002.
- [16] M. Tabuchi, M. Ueda, N. Kaji, Y. Yamasaki, Y. Nagasaki, K. Yoshikawa, K. Kataoka, and Y. Baba. Nanospheres for DNA separation chips. *Nature Biotech.*, 22:337–340, 2004.
- [17] A. Ros, W. Hellmich, T.T. Duong, and D. Anselmetti. Towards single molecule analysis in PDMS microdevices: from the detection of ultra low dye concentrations to single DNA molecule studies. *J. Biotechnol.*, 112:65–72, 2004.
- [18] T.T. Duong, G. Kim, R. Ros, M. Streek, F. Schmid, J. Brugger, D. Anselmetti, and A. Ros. Size-dependent free solution DNA electrophoresis in structured microfluidic systems. *Microelectron. Eng.*, 67-68:905–912, 2003.
- [19] J. Han, S.W. Turner, and H.G. Craighead. Entropic trapping and escape of long DNA molecules at submicron size constriction. *Phys. Rev. Lett.*, 83:1688–1691, 1999.
- [20] J. Han and H. G. Craighead. Separation of long DNA molecules in a microfabricated entropic trap array. *Science*, 288:1026–1029, 2000.
- [21] J. Fu, J. Yoo, and J. Han. Molecular sieving in periodic free-energy landscapes created by patterned nanofilter arrays. *Phys. Rev. Lett.*, 97:018103, 2006.

- [22] B. Li, X. Fang, H. Luo, Y.-S. Seo, E. Petersen, Y. Ji, M. Rafailovich, J. Sokolov, D. Gersappe, and B. Chu. Separation of DNA with different configurations on flat and nanopatterned surfaces. *Anal. Chem.*, 78:4743–4751, 2006.
- [23] A.R. Wheeler, W.R. Throdsset, R.J. Whelan, A.M. Leach, R.N. Zare, Y.H. Liao, K. Farrell, I.D. Manger, and A. Daridon. Microfluidic device for single-cell analysis. *Anal. Chem.*, 75:3581–3586, 2003.
- [24] X. Wang, D. Vykoukal, F. Becker, and P. Gascoyne. Separation of polystyrene microbeads using dielectrophoretic/gravitational field-flow-fractionation. *Biophys. J.*, 74:2689–2701, 1998.
- [25] P. Gascoyne and D. Vykoukal. Particle separation by dielectrophoresis. *Electrophoresis*, 23:1973–1983, 2002.
- [26] N. Green and H. Morgan. Dielectrophoretic investigations of sub-micrometre latex spheres. *J. Phys. D*, 30:2626–2633, 1997.
- [27] H. Morgan, M. Hughes, and N. Green. Separation of submicron bioparticles by dielectrophoresis. *Biophys. J.*, 77:516–525, 1999.
- [28] N. Green, A. Ramos, and H. Morgan. AC electrokinetics: a survey of sub-micrometre particle dynamics. *J. Phys. D*, 33:632–641, 2000.
- [29] X.-B. Wang, Y. Huang, J.P.H. Burt, G.H. Markx, and R. Pethig. Selective dielectrophoretic confinement of bioparticles in potential energy wells. *J. Phys. D*, 26:1278–1285, 1993.
- [30] B.H. Lapizco-Encinas, B.A. Simmons, E.B. Cummings, and Y. Fintschenko. Dielectrophoretic concentration and separation of live and dead bacteria in an array of insulators. *Anal. Chem.*, 76:1571–1579, 2004.
- [31] Mehmet Toner and Daniel Irimia. Blood-on-a-chip. *Annu. Rev. Biomed. Eng.*, 7:77–103, 2005.
- [32] L. Gorre-Talini, J. P. Spatz, and P. Silberzan. Dielectrophoretic ratchets. *Chaos*, 8:650–656, 1998.
- [33] S. Matthias and F. Müller. Asymmetric pores in a silicon membrane acting as massively parallel Brownian ratchets. *Nature*, 424:53–57, 2003.

-
- [34] L. Huang, E. Cox, R. Austin, and J. Sturm. Tilted Brownian ratchet for DNA analysis. *Anal. Chem.*, 75:6963–6967, 2003.
- [35] C. Marquet, A. Buguin, L. Talini, and P. Silberzan. Rectified motion of colloids in asymmetrically structured channels. *Phys. Rev. Lett.*, 88:168301, 2002.
- [36] J. Bader, R. Hammond, S. Henck, M. Deem, G. McDermott, J. Bustillo, J. Simpson, G. Mulhern, and J. Rothberg. DNA transport by a micromachined Brownian ratchet device. *J. Proc. Natl. Acad. Sci. (USA)*, 96:13165–13169, 1999.
- [37] P. Auroux, D. Iossifidis, D. Reyes, and A. Manz. Micro total analysis systems. 2. Analytical standard operations and applications. *Anal. Chem.*, 74:2637–2652, 2002.
- [38] T. Vilckner, D. Janasek, and A. Manz. Micro total analysis systems. Recent developments. *Anal. Chem.*, 76:3373–3386, 2004.
- [39] P.S. Dittrich, K. Tachikawa, and A. Manz. Micro total analysis systems. Latest advancements and trends. *Anal. Chem.*, 78:3887–3908, 2006.
- [40] J.B. Berg, J.L. Tymoczko, and L. Stryer, editors. *Biochemie*. Spektrum, 2003.
- [41] D.L. Nelson and M.M. Cox, editors. *Lehninger Biochemie*. Springer, 2001.
- [42] W. Müller-Esterl. *Biochemie. Eine Einführung für Mediziner und Naturwissenschaftler*. Spektrum, 2004.
- [43] D. Voet and J.G. Voet. *Biochemie*. VCH Weinheim, 2004.
- [44] E. F. Fynan, R. G. Webster, D. H. Fuller, J. R. Haynes, J. C. Santoro, and H. L. Robinson. DNA vaccines: protective immunizations by parenteral, mucosal, and gene-gun inoculations. *Proc. Natl. Acad. Sci. (USA)*, 90:11478–11482, 1993.
- [45] J. Viovy. Electrophoresis of DNA and other polyelectrolytes: Physical mechanisms. *Rev. Mod. Phys.*, 72:813–872, 2000.
- [46] M. Doi and S.F. Edwards. *The theory of polymer dynamics*. Clarendon Press, Oxford, 1986.
- [47] J.F. Marko and E.D. Siggia. Statistical mechanics of supercoiled DNA. *Phys. Rev. E*, 52:2912–2938, 1995.

- [48] R.M. Robertson, S. Laib, and D.E. Smith. Diffusion of isolated DNA molecules: dependence on length and topology. *Proc. Natl. Acad. Sci. (USA)*, 103:7310–7314, 2006.
- [49] Y. Lu, B. Weers, and N. Stellwagen. DNA persistence length revisited. *Biopolymers*, 61:261–275, 2002.
- [50] S. R. Quake, H. Babcock, and S. Chu. The dynamics of partially extended single molecules of DNA. *Nature*, 388:151–154, 1997.
- [51] P. J. Hagerman. Flexibility of DNA. *Ann. Rev. Biophys. Biophys. Chem.*, 17:265–286, 1988.
- [52] B. Ladoux, J. P. Quivy, P. S. Doyle, G. Almouzni, and J. L. Viovy. Direct imaging of single-molecules: from dynamics of a single DNA chain to the study of complex DNA-protein interactions. *Sci. Prog.*, 84:267–290, 2001.
- [53] R. Winter and F. Noll. *Methoden der Biophysikalischen Chemie*. Teubner, 1998.
- [54] A. Larsson, C. Carlsson, M. Jonsson, and B. Albinsson. Characterization of the binding of the fluorescent dyes YO and YOYO to DNA by polarized light spectroscopy. *J. Am. Chem. Soc.*, 116:8459–8465, 1994.
- [55] A. Larsson, C. Carlsson, and M. Jonsson. Characterization of the binding of YO to [poly(dA-dT)]₂ and [poly(dG-dC)]₂, and of the fluorescent properties of YO and YOYO complexed with the polynucleotides and double-stranded DNA. *Biopolymers*, 36:153–167, 1995.
- [56] T.L. Netzel, N. Nafisi, M. Zhao, J.R. Lenhard, and I. Johnson. Base-content dependence of emission enhancements, quantum yields, and lifetimes for cyanine dyes bound to double-strand DNA: photophysical properties of monomeric and bichromophoric DNA stains. *J. Chem. Phys.*, 99:17936–17947, 1995.
- [57] C. Carlsson, A. Larsson, and M. Jonsson. Influence of optical probing with YOYO on the electrophoretic behavior of the DNA molecule. *Electrophoresis*, 17:642–651, 1996.
- [58] C. Carlsson, M. Jonsson, and B. Akerman. Double bands in DNA gel electrophoresis caused by bis-intercalating dyes. *Nucleic Acids Res.*, 23:2413–2420, 1995.

-
- [59] H. Ihmels and D. Otto. *Topics in current chemistry. BD.258. Intercalation of organic dye molecules into double-stranded DNA - General principles and recent developments*. Springer, 2005.
- [60] T.M. Squires and S.R. Quake. Microfluidics: Fluid physics at the nanoliter scale. *Rev. Mod. Phys.*, 77:977–1026, 2005.
- [61] M.T. Tyn and T.W. Gusek. Prediction of diffusion coefficients of proteins. *Biotechnol. Bioeng.*, 35:327–338, 1990.
- [62] R. Probstein. *Physicochemical Hydrodynamics*. Wiley-Interscience, 2. edition, 2003.
- [63] L. Fauchaux and A. Libchaber. Confined brownian motion. *Phys. Rev. E*, 49:5158–5163, 1994.
- [64] G. Randall and P. Doyle. Permeation-driven flow in poly(dimethylsiloxane) microfluidic devices. *J. Proc. Natl. Acad. Sci. (USA)*, 102:10813–10818, 2005.
- [65] H. Vogel, editor. *Gerthsen Physik*. Springer, 2004.
- [66] E. Purcell. Life at low Reynolds number. *Am. J. Phys.*, 45:3–11, 1977.
- [67] D. Sinton, L. Ren, and D. Li. Visualization and numerical modelling of microfluidic on-chip injection processes. *J. Colloid Interface Sci.*, 260:431–439, 2003.
- [68] D. Long, J.L. Viovy, and A. Ajdari. Simultaneous action of electric fields and nonelectric forces on a polyelectrolyte: Motion and deformation. *Phys. Rev. Lett.*, 76:3858–3861, 1996.
- [69] E.B. Cummings, S.K. Griffiths, R.H. Nilson, and P.H. Paul. Conditions for similitude between the fluid velocity and electric field in electroosmotic flow. *Anal. Chem.*, 72:2526–2532, 2000.
- [70] R. Eichhorn and P. Reimann. personal communication.
- [71] A. Ramos, H. Morgan, N. Green, and A. Castellanos. AC electrokinetics: a review of forces in microelectrode structures. *J. Phys. D*, 31:2338–2353, 1998.
- [72] H.A. Pohl. *Dielectrophoresis: The Behavior of Neutral Matter in Nonuniform Electric Fields*. Cambridge University Press, 1978.

- [73] J.G. Kralj, M.T. Lis, M.A. Schmidt, and K.F. Jensen. Continuous dielectrophoretic size-based particle sorting. *Anal. Chem.*, 78:5019–5025, 2006.
- [74] S. Fiedler, S. Shirley, T. Schnelle, and G. Fuhr. Dielectrophoretic sorting of particles and cells in a microsystem. *Anal. Chem.*, 70:1909–1915, 1998.
- [75] N. Green, H. Morgan, and J. Milner. Manipulation and trapping of sub-micron bioparticles using dielectrophoresis. *J. Biochem. Biophys. Meth.*, 35:89–102, 1997.
- [76] E. Cummings and A. Singh. Dielectrophoresis in microchips containing arrays of insulating posts: Theoretical and experimental results. *Anal. Chem.*, 75:4724–4731, 2003.
- [77] B. Lapizco-Encinas, B. Simmons, E. Cummings, and Y. Fintschenko. Insulator-based dielectrophoresis for the selective concentration and separation of live bacteria in water. *Electrophoresis*, 25:1695–1704, 2004.
- [78] M. Washizu, S. Suzuki, O. Kurosawa, T. Nishizaka, and T. Shinohara. Molecular dielectrophoresis of biopolymers. *IEEE Trans. Industry Applications*, 30:835–843, 1994.
- [79] R. Hölzel, N. Calander, Z. Chriagwandi, M. Willander, and F. Bier. Trapping single molecules by dielectrophoresis. *Phys. Rev. Lett.*, 95:128102, 2005.
- [80] R. Krupke, F. Hennrich, H. Löhneysen, and M. Kappes. Separation of metallic from semiconducting single-walled carbon nanotubes. *Science*, 301:344–347, 2003.
- [81] C.F. Chou, J.O. Tegenfeldt, O. Bakajin, S.S. Chan, E.C. Cox, N. Darnton, T. Duke, and R.H. Austin. Electrodeless dielectrophoresis of single- and double-stranded DNA. *Biophys. J.*, 83:2170–2179, 2002.
- [82] T.B. Jones. *Electromechanics of particles*. Cambridge University Press, 1995.
- [83] J.D. Jackson. *Klassische Elektrodynamik*. de Gruyter, 1983.
- [84] T.B. Jones. Basic theory of dielectrophoresis and electrorotation. *IEEE Engineering in Medicine and Biology*, (November/December):33, 2003.
- [85] D. Porschke. Macrodipoles Unusual electric properties of biological macromolecules. *J. Biophys. Chem.*, 66:241–257, 1997.

-
- [86] B. Saif, R. K. Mohr, C. J. Montrose, and T. A. Litovitz. On the mechanism of dielectric relaxation in aqueous DNA solutions. *Biopolymers*, 31:1171–1180, 1991.
- [87] D. Porschke. The mechanism of ion polarisation along DNA double helices. *Biophys. Chem.*, 22:237–247, 1985.
- [88] D. Porschke. Unique physical signature of DNA curvature and its implications for structure and dynamics. *J. Phys. Chem. B*, 111:12004–12011, 2007.
- [89] H. Washizu and K. Kikuchi. Electric polarizability of DNA in aqueous salt solution. *J. Phys. Chem. B*, 110:2855–2861, 2006.
- [90] C. Asbury, A. Diercks, and G. v. d. Engh. Trapping of DNA by dielectrophoresis. *Electrophoresis*, 23:2658–2666, 2002.
- [91] D. Bakewell, I. Ermolina, H. Morgan, J. Milner, and Y. Feldman. Dielectric relaxation measurements of 12 kbp plasmid DNA. *Biochim. Biophys. Acta*, 1493:151–158, 2000.
- [92] C. Asbury and G. v. d. Engh. Trapping of DNA in nonuniform oscillating electric fields. *Biophys. J.*, 74:1024–1030, 1998.
- [93] A. Castellanos, A. Ramos, A. Gonzalez, N. Green, and H. Morgan. Electrohydrodynamics and dielectrophoresis in microsystems: scaling laws. *J. Phys. D*, 36:2584–2597, 2003.
- [94] F. van der Touw and M. Mandel. Dielectric increment and dielectric dispersion of solutions containing simple charged linear macromolecules. I. Theory. *J. Biophys. Chem.*, 2:218–230, 1974.
- [95] U. Mohanty and Y. Zhao. Polarization of counterions in polyelectrolytes. *Biopolymers*, 38:377–388, 1996.
- [96] J. Gimsa. Particle characterization by ac-electrokinetic phenomena: 1. A short introduction to dielectrophoresis (dp) and electrorotation (er). *Colloid Surf. A*, 149:451–459, 1999.
- [97] D.J. Bakewell and H. Morgan. Dielectrophoresis of DNA: time- and frequency-dependent collections on microelectrodes. *IEEE Trans. Nanobioscience*, 5:139–146, 2006.

- [98] D. C. Rau and E. Charney. Electric dichroism of DNA. Influence of the ionic environment on the electric polarizability. *Biophys. Chem.*, 17:35–50, 1983.
- [99] D. Frenkel. Soft condensed matter. *Physica A*, 313:1–31, 2002.
- [100] A. Einstein. On the motion of small particles suspended in liquids at rest required by the molecular kinetic theory of heat. *Ann. Phys.*, 17:549–560, 1905.
- [101] J. Rousselet, L. Salome, A. Ajdari, and J. Prost. Directional motion of Brownian particles induced by a periodic asymmetric potential. *Nature*, 370:446–447, 1994.
- [102] L.P. Faucheux, G. Stolovitzky, and A. Libchaber. Periodic forcing of a Brownian particle. *Phys. Rev. E*, 51:5239–5250, 1995.
- [103] R. Eichhorn, P. Reimann, B. Cleuren, and C. Van den Broeck. Moving backward noisily. *Chaos*, 15:026113, 2005.
- [104] T.J. Banys, I.V. Parshelyunas, and Y.K. Pozhela. Absolute negative resistance of gallium-arsenide in a strong microwave field. *Sov. Phys. Semicond.*, 5:1727, 1972.
- [105] B.J. Keay, S.J. Allen, J. Galan, J.P. Kaminski, K.L. Campman, A.C. Gossard, U. Bhattacharya, and M.J.W. Rodwell. Photon-assisted electric field domains and multiphoton-assisted tunneling in semiconductor superlattices. *Phys. Rev. Lett.*, 75:4098–4101, 1995.
- [106] P. Reimann, C. Van den Broeck, and R. Kawai. Nonequilibrium noise in coupled phase oscillators. *Physical Review E*, 60(6):6402–6406, 2004.
- [107] R. Eichhorn, P. Reimann, and P. Hänggi. Brownian motion exhibiting absolute negative mobility. *Phys. Rev. Lett.*, 88:190601, 2002.
- [108] R. Eichhorn, P. Reimann, and P. Hänggi. Paradoxical motion of a single Brownian particle: Absolute negative mobility. *Phys. Rev. E*, 66:066132, 2002.
- [109] R. Eichhorn, P. Reimann, and P. Hänggi. Absolute negative mobility and current reversals of a meandering Brownian particle. *Physica A*, 325:101–109, 2003.
- [110] B. Cleuren and C. Van den Broeck. Random walks with absolute negative mobility. *Phys. Rev. E*, 65:030101, 2002.
- [111] P. Reimann. Brownian motors: noisy transport far from equilibrium. *Phys. Rep.*, 361:57–265, 2002.

-
- [112] H. Risken. *The Fokker-Planck Equation*. Springer, 1989.
- [113] H.A. Kramers. Brownian motion in a force field and the diffusion model of chemical reactions. *Physica*, 4:284–304, 1940.
- [114] A. Barone and G. Paterno. *Physics and Applications of the Josephson Effect*. Wiley-VCH, New York, 1982.
- [115] A. Ajdari and J. Prost. Free-flow electrophoresis with trapping by a transverse inhomogeneous field. *J. Proc. Natl. Acad. Sci. (USA)*, 88:4468–4471, 1991.
- [116] G.I. Nixon and G.W. Slater. Entropic trapping and electrophoretic drift of a polyelectrolyte down a channel with a periodically oscillating width. *Phys. Rev. E*, 53:4969–4980, 1996.
- [117] P.J. Park and W. Sung. Dynamics of a polymer surmounting a potential barrier: The Kramers problem for polymers. *J. Chem. Phys.*, 111:5259–5266, 1999.
- [118] P. Hänggi, P. Talkner, and M. Borkovec. Reaction-rate theory: fifty years after Kramers. *Rev. Mod. Phys.*, 62:251–341, 1990.
- [119] P. Reimann, G. J. Schmid, and P. Hänggi. Universal equivalence of mean first-passage time and Kramers rate. *Phys. Rev. E*, 60:R1–R4, 1999.
- [120] S. Lifson and J. Jackson. On the self-diffusion of ions in a polyelectrolyte solution. *J. Chem. Phys.*, 36:2410–2414, 1962.
- [121] P. Reimann, C. Van den Broeck, H. Linke, P. Hänggi, J. Rubi, and A. Perez-Madrid. Diffusion in tilted periodic potentials: enhancement, universality, and scaling. *Phys. Rev. E*, 65:031104, 2002.
- [122] M. Schreier, P. Reimann, P. Hänggi, and E. Pollak. Giant enhancement of diffusion and particle selection in rocked periodic potentials. *Europhys. Lett.*, 44:416–422, 1998.
- [123] W. E. Moerner and M. Orrit. Illuminating single molecules in condensed matter. *Science*, 283:1670–1676, 1999.
- [124] W.E. Moerner and D.P. Fromm. Methods of single-molecule fluorescence spectroscopy and microscopy. *Rev. Sci. Instr.*, 74:3597–3619, 2003.

- [125] D. Martin, M. Forstner, and J. Käs. Apparent subdiffusion inherent to single particle tracking. *Biophys. J.*, 83:2109–2117, 2002.
- [126] T. Savin and P.S. Doyle. Static and dynamic errors in particle tracking microrheology. *Biophys. J.*, 88:623–638, 2005.
- [127] A.E. Cohen. *Trapping and manipulating single molecules in solution*. PhD thesis, Stanford University, 2006.
- [128] D. Campbell, K. Beckman, C. Calderon, P. Doolan, R. Moore, A. Ellis, and G. Lisensky. Uses of polydimethylsiloxane (PDMS) elastomer. <http://mrsec.wisc.edu/edetc/PDMS/index.html>, 2005.
- [129] U. Aebi and T. Pollard. A glow discharge unit to render electron microscope grids and other surfaces hydrophilic. *J. Electron Microsc. Tech.*, 7:29–33, 1987.
- [130] DIN 38404-10.
- [131] N. Streitner and C. Voss. Quality control of the samples with capillary gel electrophoresis, AG Fermentationstechnik, Technische Fakultät, Universität Bielefeld, 2007.
- [132] T. Schmidt, K. Friehs, M. Schlee, C. Voss, and E. Flaschel. Quantitative analysis of plasmid forms by agarose and capillary gel electrophoresis. *Anal. Biochem.*, 274:235–240, 1999.
- [133] N. Stuurmann. ImageJ plugin MTrack 2. valelab.ucsf.edu/nico/IJplugins/MTrack2.html, 2004.
- [134] L. Bogunovic. Einflüsse der Ionenkonzentration und von Fluorophoren auf die Polarisierbarkeit von linearer DNA in Mikrofluidiksystemen, Bachelor Thesis, Bielefeld University, 2007.
- [135] P. Reimann, C. Van den Broeck, H. Linke, P. Hänggi, J. M. Rubi, and A. Perez-Madrid. Giant acceleration of free diffusion by use of tilted periodic potentials. *Phys. Rev. Lett.*, 87:010602, 2001.
- [136] P. Reimann, C. Van den Broeck, and R. Kawai. Nonequilibrium noise in coupled phase oscillators. *Phys. Rev. E.*, 60:6402–6406, 1999.
- [137] B. Cleuren and C. Van den Broeck. Brownian Motion with absolute negative mobility. *Phys. Rev. E*, 67:055101, 2003.

-
- [138] J. Regtmeier. Absolut Negative Mobilität, Diplomarbeit, Bielefeld University, 2005.
- [139] R. Eichhorn and P. Reimann. Analytical theory of absolute negative mobility in a microfluidic device. *Acta Phys. Pol. B*, 37:1491–1501, 2006.
- [140] L.R. Huang, P. Silberzan, J.O. Tegenfeldt, E.C. Cox, J.C. Sturm, R.H. Austin, and H. Craighead. Role of molecular size in ratchet fractionation. *Phys. Rev. Lett.*, 89:178301, 2002.
- [141] Feynman, Leighton, and Sands. *The Feynman Lectures on Physics*. Addison-Wesley Longman, 6th printing edition, 1977.
- [142] P. Reimann and P. Hänggi. Introduction to the physics of Brownian motors. *Appl. Phys. A*, 75:169–178, 2002.
- [143] C. Marquet, A. Buguin, L. Talini, and P. Silberzan. Rectified motion of colloids in asymmetrically structured channels. *Phys. Rev. Lett.*, 88:168301, 2002.
- [144] M.P. Hughes. Strategies for dielectrophoretic separation in laboratory-on-a-chip systems. *Electrophoresis*, 23:2569–2582, 2002.
- [145] A. Lao and I. Hsing. Flow-based and sieving matrix free DNA differentiation by a miniaturized field flow fractionation device. *Lab Chip*, 5:687–690, 2005.
- [146] N. C. Stellwagen. Electric birefringence of restriction enzyme fragments of DNA: optical factor and electric polarizability as a function of molecular weight. *Biopolymers*, 20:399–434, 1981.
- [147] J. Elias and D. Eden. Transient electric birefringence study of the persistence length and electrical polarizability of restriction fragments of DNA. *Macromolecules*, 14:410–419, 1981.
- [148] D. C. Rau and V. A. Bloomfield. Transient electric birefringence of T7 viral DNA. *Biopolymers*, 18:2783–2805, 1979.
- [149] M. Hanss and J. C. Bernengo. Dielectric relaxation and orientation of DNA molecules. *Biopolymers*, 12:2151–2159, 1973.
- [150] L.H. Pope, M.C. Davies, C.A. Laughton, C.J. Roberts, J.B. Tendler, and P.M. Williams. Atomic force microscopy studies of the intercalation-induced changes in plasmid DNA tertiary structure. *J. Microscopy*, 199:68–78, 2000.

- [151] J. Giddings. *Unified separation science*. John Wiley Sons: New York, 1991.
- [152] E. Petersen, B. Li, X. Fang, H. Luo, V. Samuilov, D. Gersappe, J. Sokolov, B. Chu, and M. Rafailovich. DNA migration and separation on surfaces with a microscale dielectrophoretic trap array. *Phys. Rev. Lett.*, 98:088102, 2007.
- [153] H. Oana, R.W. Hammond, J.J. Schwinefus, S. Wang, M. Doi, and M.D. Morris. High-speed separation of linear and supercoiled DNA by capillary electrophoresis. Buffer, entangling polymer, and electric field effects. *Anal. Chem.*, 70:574–579, 1998.
- [154] K. Seiler, Z.H. Fan, K. Fluri, and D.J. Harrison. Electroosmotic pumping and valveless control of fluid flow within a manifold of capillaries on a glass chip. *Anal. Chem.*, 66:3485–3491, 1994.
- [155] S. Tuukkanen, A. Kuzyk, J.J. Toppari, H. Häkkinen, V.P. Hytönen, E. Niskanen, M. Rinkiö, and P. Törma. Trapping of 27 bp–8 kbp DNA and immobilization of thiol-modified DNA using dielectrophoresis. *Nanotechnology*, 18:295204, 2007.
- [156] J. Bowers and R. Prud'homme. Low field theory of polymer transient electric birefringence. *J. Phys. Chem.*, 96:7135–7143, 1992.
- [157] M. Duval, P. Lutz, and C. Strazielle. Hydrodynamic dimensions of ring-shaped macromolecules in a good solvent. *Makromol. Chem. Rapid Commun.*, 6:71–76, 1985.
- [158] D.F. Hodgson and E.J. Amis. Dilute solution behavior of cyclic and linear polyelectrolytes. *J. Chem. Phys.*, 95:7653–7663, 1991.
- [159] S. Cocco, J. F. Marko, R. Monasson, A. Sarkar, and J. Yan. Force-extension behavior of folding polymers. *Eur. Phys. J. E*, 10:249–263, 2003.
- [160] M. Hogan, N. Dattagupta, and D.M. Crothers. Transient electric dichroism of rod-like DNA molecules. *Proc. Natl. Acad. Sci. (USA)*, 75:195–199, 1978.
- [161] T. C. Boles, J. H. White, and N. R. Cozzarelli. Structure of plectonemically supercoiled DNA. *J. Mol. Biol.*, 213:931–951, 1990.
- [162] S. Koneshan, J. Rasaiah, R.M. Lynden-Bell, and S.H. Lee. Solvent structure, dynamics and ion mobility in aqueous solution at 25°C. *J. Phys. Chem. B*, 102:4193–4204, 1998.

-
- [163] the calculated time is only an estimate because peak-to-peak values of the sinusoidal voltage are used.
- [164] D. C. Rau and E. Charney. Polarization of the ion atmosphere of a charged cylinder. *Biophys. Chem.*, 14:1–9, 1981.
- [165] Y. Murayama, Y. Sakamaki, and M. Sano. Elastic response of single DNA molecules exhibits a reentrant collapsing transition. *Phys. Rev. Lett.*, 90:018102, 2003.
- [166] A.Y. Grosberg, T.T. Nguyen, and B.I. Shklovskii. Colloquium: The physics of charge inversion in chemical and biological systems. *Rev. Mod. Phys.*, 74:329–345, 2002.
- [167] P.Y. Hsiao and E. Luijten. Salt-induced collapse and reexpansion of highly charged flexible polyelectrolytes. *Phys. Rev. Lett.*, 97:148301, 2006.
- [168] M. Shimizu, S. Sasaki, and M. Tsuruoka. DNA length evaluation using cyanine dye and fluorescence correlation spectroscopy. *Biomacromolecules*, 6:2703–2707, 2005.
- [169] P.K. Wong, Y.-K. Lee, and C.-M. Ho. Deformation of DNA molecules by hydrodynamic focusing. *J. Fluid Mech.*, 497:55–65, 2003.
- [170] G.C. Randall and P.S. Doyle. DNA deformation in electric fields: DNA driven past a cylindrical obstruction. *Macromolecules*, 38:2410–2418, 2005.
- [171] Y. Liu, Y. Jun, and V. Steinberg. Longest relaxation times of double-stranded and single-stranded DNA. *Macromolecules*, 40:2172–2176, 2007.
- [172] S.H. Lee and D.G. Grier. Giant colloidal diffusivity on corrugated optical vortices. *Phys. Rev. Lett.*, 96:190601, 2006.
- [173] R. Eichhorn. personal communication.
- [174] M. Abramowitz and I. Stegun. *Handbook of Mathematical Functions*. Dover Publications, New York, 1965.

Acknowledgement

An dieser Stelle möchte ich mich bei allen bedanken, die an der Entstehung dieser Arbeit beteiligt gewesen sind. Es sind in diesem besonderen Falle zwei Arbeitsgruppen, die gemeinsam zum Erfolg der verschiedenen Projekte im Rahmen des SFB 613 beigetragen haben. Gerade dieses Wechselspiel zwischen Theorie und Experiment ist die Grundlage dieser Arbeit.

Zu erst möchte ich Herrn Prof. Dario Anselmetti für die Möglichkeit zur Durchführung der experimentellen Arbeiten und das entgegengebrachte Vertrauen danken. Ebenso danke ich Herrn Prof. Peter Reimann aus der Gruppe Kondensierte Materie für die Möglichkeit diese Arbeit auf ein solides theoretisches Fundament aufbauen zu können. Nur durch die sehr enge Zusammenarbeit beider Gruppen war es möglich viele gute Ergebnisse in so kurzer Zeit zu erzielen.

Auf experimenteller Seite gilt mein besonderer Dank Frau PD Dr. Alexandra Ros für die wissenschaftliche Betreuung. Die Diskussionen und sehr guten Anregungen, sowohl zur Physik als auch im Besonderen zu Fragen der Chemie, haben ganz wesentlich zum Erfolg dieser Arbeit beigetragen.

Auf theoretischer Seite gilt mein tiefer Dank Herrn Dr. Ralf Eichhorn. Ohne seine Betreuung, Unterstützung und die zur Verfügungstellung und Weiterentwicklung seiner Simulationssoftware, wäre diese Arbeit in der erzielten Form nicht möglich gewesen. Ich danke ihm für sehr viele kritische, wertvolle und sehr angenehme Diskussionsrunden, und das kritische Korrekturlesen dieser Arbeit.

Mein spezieller Dank gilt weiterhin Herrn Henning Höfemann. Er hat wertvolle Beiträge zur Dielektrophorese von DNA geliefert und mich bei der Lithographie unterstützt. Herrn Lukas Bogunovic bin ich ebenfalls zu sehr großem Dank verpflichtet. Er hat sehr gute, fortschrittbringende Beiträge zur DNA Dielektrophorese geliefert. Beiden danke ich für die sehr gute Zusammenarbeit, die Bürogemeinschaft und die entstandenen Freundschaften.

Mein ganz besonderer Dank gilt Frau Dr. Wibke Hellmich und Herrn Dr. Thanh Tu Duong. Sie haben mir vom ersten Tag an immer mit Rat und Tat zur Seite gestanden. Die erfolgreiche Zusammenarbeit, die Diskussionen und die entstandene Freundschaft

sind für mich von großem Wert.

Des weiteren Danke ich Carsten Oberpenning und Sebastian Grauwin für ihre Beiträge zur ANM, und Lisa Czaja und Tobias Rosenstock für die Erstellung von AFM Bildern der Plasmide. Rafael Szczepanowski danke ich für die zur Verfügungstellung des PJP2 Plasmids und einige Agarosegele. Für die weitere Qualitätskontrolle danke ich Nadine Streitner, Carsten Voß und Hanna Bednarz. Der PlasmidFactory mit Dr. Martin Schleef und Dr. Marco Schmeer danke ich für die kostenlosen Plasmidproben. Martina Everwand und Stefan Gerkens danke ich für ihre weiteren Arbeiten im Feld der Mikrofluidik. Dank gilt auch der M- und E- Werkstatt für die immer sehr prompte und gute Erledigung aller Aufträge.

Des weitem danke ich der gesamten Arbeitsgruppe Biophysik für das sehr unkomplizierte Umfeld. Jederzeit findet man ein offenes Ohr, seien es Fragen zur Chemie, die Frau Dr. Katja Tönsing oder Rainer Eckel zu beantworten wussten, Fragen zum AFM, die Dr. Robert Ros oder Volker Walhorn erschöpfend beantworteten, Fragen zu Technik und Optik, die Herr Christoph Pelargus umgehend klären konnte, oder bürokratische Hindernisse, die Frau Gabi Krome aus zu räumen wusste.

Last but not least, danke ich meiner Familie, meinen Eltern, die mich stets auf meinem Weg bestärkt haben und mir alles an wichtigem Rüstzeug mitgegeben haben, meinem Bruder und seiner Frau, auf die immer Verlass ist, meinen Schwiegereltern incl. Oma für die sehr herzliche Unterstützung, und meiner eigenen kleinen Familie mit meiner Frau und unserem Sohn, die auch in anstrengenden Zeiten immer an meiner Seite waren und mir mit sehr viel Geduld all dies ermöglicht haben.

Curriculum Vitae

Jan Regtmeier

born in Bielefeld, Germany, Nov. 25th 1979, married

1986 - 1990	Domschule Minden
1990 - 1996	Ratsgymnasium Minden
Sept. 1996 - May 1997	Decatur County Highschool, Kansas, USA
May 1997 - 1999	Ratsgymnasium Minden, Abitur (1,4)
2000 - 2002	Studies in Physics, RWTH Aachen, Vordiplom (gut)
2002 - 2004	Studies in Physics, Bielefeld Univeristy
Juli 2004 - Feb. 2005	Diploma Thesis: <i>Absolute negative Mobility</i> (mit Auszeichnung) at the groups Experimental Biophysics & Applied Nanoscience and Condensed Matter Theory, Bielefeld University
Feb. 2005 - Dec. 2007	PhD study at the group Experimental Biophysics & Ap- plied Nanoscience, Bielefeld University

Bielefeld, Nov. 27th 2007